HYDROELASTIC ANALYSIS COUPLED WITH NONLINEAR MOORING-RISERS FOR A MOORED DEFORMABLE FLOATING BODY AND DEVELOPMENT OF DYNAMIC POSITIONING SYSTEM FOR HIGH ACCURACY

A Dissertation

by

HEONYONG KANG

Submitted to the Office of Graduate and Professional Studies of
Texas A&M University
in partial fulfillment of the requirements for the degree of

DOCTOR OF PHILOSOPHY

Chair of Committee, Moo-Hyun Kim
Committee Members, Richard S. Mercier
Jeffrey M. Falzarano
Sivakumar Rathinam
Head of Department, Robin Autenrieth

December 2014

Major Subject: Ocean Engineering

ABSTRACT

Two main topics of offshore technologies, hydroelasticity and dynamic positioning system, are investigated in the present research.

For the larger dimension of offshore structures in harsher operating environments, comprehensive hydroelastic analysis is developed. The interactions of a moored deformable floating body and waves are solved by the modal expansion method, and the dynamics of the deformable floating body is fully coupled with the nonlinear mooring-riser dynamics. Not only the hydroelastic dynamic motion responses but also the corresponding dynamic stress resultants are achieved for regular waves and random seas. A new methodology is developed for the direct time domain hydroelastic structural analysis for the random seas without infeasible computational fluid dynamics. As case studies, both of a slender structure and a large volume 3D structure are considered. The slender body case adopts the well-known beam theory to represent the deformations and the 3D structure case employs the finite element method for modal analysis. Moreover, the twisting effects of the 3D structure and corresponding 3D hydroelastic effects are investigated. The developed numerical tools are robustly verified by cross-correlation between frequency and time domains. Each case study includes the resonance phenomenon of the floating body deformation, and its influences on the dynamic motions and stress resultants are studied. The enhanced resonances due to the nonlinear wave loads are investigated by adding the 2^{nd} order wave loads to the time domain hydroelastic dynamic analyses. Taking advantages of time-domain hydroelastic analysis, a numerical hammer test is conceived and the real wet natural frequencies are identified.

For the purpose of float-over-based offshore installment, a high accuracy dynamic positioning system is developed. The optimum control system is designed using a combination of Kalman filter and PD control with the separation theorem. Subsequently, the generalized allocation scheme is employed for faster and more accurate reactions. As an example, an appreciably small watch circle is achieved and the corresponding resultants are clarified in terms of individual thrusts and azimuth angles. Moreover, the developed DP control is embedded into the mooring-riser-hull coupled dynamics, and the benefits and characteristics of the mooring-combined DP system are discussed.

DEDICATION

To my mother, YeongDoo Jeong,

who raised me with indescribable love and sacrifice,

I love you and thank you wholeheartedly.

To my wife, KyungJae Lee,

who is the eternal partner inspiring and amazing,

I love you beyond expression.

ACKNOWLEDGEMENTS

From the bottom of my heart, I thank all those who have stood by me and helped throughout my graduate school periods. I gratefully appreciate my supervisor, Professor Joseph M.H. Kim for ceaselessly giving me thoughtful guidance and cheerful support during the whole period of graduate studies.

Heartfelt thanks also go to my committee members, Professors Richard S. Mercier, Jeffrey M. Falzarano, and Sivakumar Rathinam for teaching me and nourishing my researches to complete. I also want to extend my gratitude to the senior engineers from Professor Kim's research group, Drs. S.S. Ryu and D.H. Lee for their invaluable mentoring.

Finally, thanks to my father, MyeongKi Kang, my mother, YeongDoo Jeong, and my sisters, JiHye and JiSook, and brothers-in-law, HyeongWon Jeon and SuHo Ji, and nephews and nieces, deeply.

.

NOMENCLATURE

VLFS	Very Large Floating Structure
DP	Dynamic Positioning
FLNG	Floating Liquefied Natural Gas
DOF	Degree of Freedom
BVP	Boundary Value Problem
PD	Proportional & Derivative
BEM	Boundary Element Model
FEM	Finite Element Model
TLP	Tension Leg Platform
FPSO	Floating Production Storage and Offloading

TABLE OF CONTENTS

Page

LIST OF FIGURES

Page

LIST OF TABLES

Page

1. INTRODUCTION

With growing energy demand and global economy, the size of offshore platforms or marine vessels gets enlarged and the operating environment is extended, which requires broader functionality. Among the various subjects of great importance in the corresponding offshore technology development, two main topics, hydroelasticity and dynamic positioning system, are investigated in this research.

Hydroelasticity generally represents bi-directional interaction of fluids and elastic solid structures. In the research field of ocean engineering, the fluid is ocean water waves, and the solid structures can be any objects in the ocean environment such as large deformable floating bodies or flexible risers. The hydroelasticity is normally regarded as the coupled interactions of the deformable floating bodies and ocean waves. In the conventional ocean engineering field, the bi-directional hydroelastic analysis has been depreciated. The floating body is assumed as a rigid body. Even though a number of researchers studied for very large floating structures (VLFS) in freely floating condition up to the linear order, it mainly focuses on frequency domain for regular waves and the mooring-riser interactions and random sea tests have been rarely studied.

In this study, the deformation of the floating body and its interaction with waves or other environmental loads are investigated by the modal expansion method beyond the conventional rigid body assumption. Moreover, the moored deformable floating body is analyzed by solving the fully coupled interactions of the deformable body, water waves, and nonlinear mooring-riser dynamics. As the first fully coupled hydroelastic analysis for a moored deformable body, the influences of the interacting nonlinear

mooring-riser dynamics will be examined thoroughly on the deformable floating body and flexible mooring riser system in the random seas. The local interactions of the flexible riser or mooring line with fluids are not included. The local phenomena are usually investigated with the floating body interactions ignored.

Contrary to the previous hydroelastic studies with limited results either in single domain or from partial analysis, the comprehensive hydroelastic analysis is implemented in both the frequency and time domains. In both domains respective hydroelastic motion and structural dynamics are achieved for regular and irregular waves. Resonance phenomena of the deformation are also investigated in terms of the motion responses and stress resultants. Especially in the time domain, a new methodology is developed to achieve dynamic stress resultants in the random seas without costly CFD and DNS. As the first direct hydroelastic structural analysis feasible for random seas, the corresponding benefits are discussed including the completeness over the deflection-based conventional method and the overwhelming efficiency than DNS. As further advancement, a simplified method is introduced to include the second order wave loading to address the enhanced resonance in the high or low frequency region.

The next main topic, dynamic positioning system, is normally utilized for the purpose of station keeping of offshore structures such as drilling vessels, service vessels, or transport vessels. The dynamic positioning (DP) control system manages the global position of the vessels undergoing irregular environmental loads such as waves, winds, and currents or ice impacts. In general, the DP controlled drilling vessels or service vessels are more popular than offshore installation purpose, and they accept watch circle

range about 3~8 % of the operating water depth during long period of time. On the contrary, the offshore installation using the float-over method requires higher accuracy for a short period.

In this study, the high accuracy dynamic positioning control is developed to achieve an appreciably small watch circle in operating condition needed for the float-over installation. Based on the individual state-of-art DP technologies, an optimum integrated DP system is built. The high accuracy DP control consists of separation theorem to combine Kalman filtering and optimal feedback as well as the generalized allocation scheme. An automatic estimation method for Kalman filter parameters is introduced by taking advantage of numerical simulation. The generalized allocation is designed by pseudo inverse matrix to achieve instant reactions without delay by the conventional Lagrangian method. Moreover, the DP control is equipped into the moored structure. Effectiveness of the high accuracy DP control is comprehensively investigated and benefits of the mooring-combined DP control system are discussed.

In that the DP system is in general designed by static analysis for the maximum environmental loads, the present method can provide more realistic DP design that includes interacting dynamics of DP system with environmental loads and a mooring system.

2. HYDROELASTICITY IN FREQUENCY DOMAIN

Over the last decades, many researchers investigated in the hydroelasticity, focusing on the frequency domain up to the first order. General theories about the ship hydroelasticity are addressed by Bishop and Price [2]. Newman established frameworks for the water wave interactions with deformable floating bodies and solved various types of floating body problems including the deformable body [28]. He adopted the modal expansion method to account for the bi-directional interaction of the floating body's deformation with water waves. Contrary to the direct coupling method, the modal expansion method is beneficial in terms of computing cost, whereas it has higher complexity to build the numerical tool [17]. Moreover, the modal expansion method has strong potential for further applications, taking advantages of computing efficiency and structural compatibility. The compatibility of the numerical structure means that the finite number of elastic modes for the deformable structure can be effectively combined and coupled with other objects such as multiple deformable bodies, wind turbine units, nonlinear mooring lines or risers, or any other dynamic units. Regarding the modal analysis, Rao covered general theories and various methods to represent vibrations of multiple degrees of freedom [33].

Along with the modal expansion method on the linear frequency domain, Newman [30] and Kashiwagi [16] introduced the nonlinear interpolation schemes for the large scale analysis to improve accuracy in the high frequency region with efficiency assured. The significant deformation and its interaction of a membrane type structure are studied by Cho and Kim [4] and represented satisfactory correspondence between

experiments and numerical analyses. Kim et al. solved hydroelastic problems for two-body VLFS by using plate theory [20]. For reviews, the state of art hydroelastic analyses are summarized by Hamamoto et al. [12], Kashiwagi [18] and Watanabe et al. [37].

In the present study of the frequency-domain hydroelasticity, two types of analyses are performed: hydroelastic dynamic analysis and hydroelastic structural analysis. Ocean waves are assumed to be the potential flow and the boundary element method (BEM) is used. The modal expansion method is adopted with the 4th order B-spline with Galerkin method. To take proper elastic modes of a deformable structure, the finite element method (FEM)-based modal analysis is addressed as well as the analytic solution-based modal analysis.

The modal expansion method is based on the assumption that water contact effects and interacting wave effects can be regarded as loads acting on the deformable body instead of the boundary conditions that affect the mode shapes and natural frequencies [2]. Therefore the dry-condition driven mode shapes and natural frequencies are directly included in the system of motion equations after the 6 DOFs, and the extended BVP provides with the hydrodynamic pressures and hydrostatic pressures as loads acting on the floating deformable body, which are induced by the water and wave effects to the total 6+*e* DOFs. The hydrodynamic pressures can be categorized into the diffraction potential part as wave excitations and radiation potential part as radiation damping and added inertia coefficients.

Therefore the modal expansion method does not require to update the wet-condition driven mode shapes and frequencies. Although such an assumption may be

considered to depreciate wet condition or wave effects to the deformation mode shapes and natural frequencies, it is still arguable to determine which water and wave effects will affect the modal analysis and the validity of the modal expansion method has been robustly proved over the decades in comparison of experiments and DNS as well demonstrated by Kashiwagi [17]. It is seen that the modal expansion method is well coincided with experiments and almost identical to the costly DNS. Moreover, the computational feasibility of the DNS, which can solve the directly coupled fluid-structure domain, is significantly low especially for the random seas. Therefore, the modal expansion method is utilized in the present study.

Hydroelastic Dynamic Analysis

The hydroelastic dynamic analysis achieves the motion responses of a deformable floating body, which include the coupled interactions among 6 DOF rigid motions, the finite number of elastic modes, and waves.

Governing Equation

Assuming the ocean waves are ideal flows, the interactions with a floating body can be addressed by solving the boundary value problems (BVP) of the Laplace equation, where the boundary is defined by interfaces of the floating body's surface and waters.

$$\nabla^2 \Phi = 0 \qquad (1)$$

The velocity potential Φ consists of the diffraction potential, which includes incident and scattered potentials, and radiation potential. The radiation velocity potential is induced by all types of motions of the floating body. Therefore, the hydroelastic analysis requires extension of the BVP to include the deformation responses of elastic modes as well as 6 degrees of freedom (DOF) rigid modes. The solutions to the extended BVP represent the fluid domain interacting with the deformable floating body over the rigid body's 6 DOF motions.

$$\begin{aligned} &\Phi = \Phi_D + \Phi_R, \\ &\textit{where } \Phi_D = \Phi_I + \Phi_S, \textit{ and } \Phi_R = \sum_{j=1}^{K} x_j \Phi_j,\ K = 1,...,(6+e) \end{aligned} \tag{2}$$

The subscripts are initials of the type of velocity potentials. The total number of radiation potentials is 6+*e*, which correspond to the total number of DOFs including the *e* elastic modes to represent the floating body's deformation. For the multiple-body analysis, *K* will be the total summation of each body's full DOFs.

$$\begin{aligned} &\frac{\partial \Phi_D}{\partial \vec{n}} = 0 \ \ on\ S_w, \\ &\frac{\partial \Phi_K}{\partial \vec{n}} = i\omega \vec{n}_K, \text{ where } K = 1,...,(6+e), \text{ or } \frac{\partial \Phi_R}{\partial \vec{n}} = i\omega \vec{n}\left(\zeta + \alpha \times r + \upsilon_j \Xi_j\right), \\ &\frac{\partial \Phi}{\partial z} - \kappa \Phi = 0 \ on\ z = 0, \quad \frac{\partial \Phi}{\partial z} = 0 \ on\ z = -h, \text{ where } \kappa = \omega^2 / g, \\ &\Phi \to 0 \text{ when } r \to \infty. \end{aligned} \tag{3}$$

The velocity potentials are solutions to respective boundary conditions. Based on the linear order assumption, the diffraction potential presents the reflected waves from the fixed floating body surface, and radiation potentials imply the generated waves by each of the DOFs, which consist of translational motions ζ, rotational motions α and

elastic modal responses υ. Both types of boundary conditions are called as Neumann boundary conditions. The last two boundary conditions represent free-surface and bottom boundary conditions, respectively. After solving the respective BVPs, the total velocity potentials are superposition of all the potentials.

The BVP of the hydroelasticity is regarded as the extended boundary value problem in that there exist *e* more boundary conditions to satisfy for the interacting deformation of the floating body, especially for the radiation potentials. To solve the extended BVP, the conventional BEM is adopted by using WAMIT [6, 23, 24, 27, 29]. A subroutine is further developed to be compatible to the general FEM modal analysis and either source panel method or the known green function method is used for the case studies.

Once the velocity potentials obtained, the system of motion equations is formulated from the known hydrodynamic and hydrostatic pressure fields by the linear Bernoulli Equation.

$$p = -\rho \frac{\partial \Phi}{\partial t} - \rho g z \qquad (4)$$

The pressures induce forces *F*, moments *M*, and modal forces *N*. Ξ is the mode shape of each elastic mode.

$$\begin{aligned} F_j &= \iint_{S_w} \vec{n}_j p \, ds, \text{ where } j = 1,2,3, \\ M_j &= \iint_{S_w} \left(\vec{x} \times \vec{n}_j\right) p \, ds, \text{ where } j = 1,2,3 \\ N_j &= \iint_{S_w} \Xi(\vec{x}) \vec{n}_j p \, ds, \text{ where } j = 1,...,e. \end{aligned} \qquad (5)$$

The hydrodynamic pressures of the diffraction potential generate excitations of each mode F^{1st}, the hydrodynamic pressures of the radiation potential induce added inertia ΔM and radiation damping D^R, and the hydrostatic pressures and gravity effects generate the hydrostatic gravitational stiffness K^H. Along with the momentum equilibrium of the deformable floating body with respect to the body coordinate system, the system of motion equations is given as

$$(M^E + \Delta M)\ddot{X} + (D^R{}_\omega)\dot{X} + (K^E + K^H)X = F^{1st}. \quad (6)$$

The system of equations for the hydroelasticity is (6+*e*) by (6+*e*) matrix equation. The inertial matrix M^E and stiffness matrix K^E have additional *e* diagonal modal inertia and stiffness elements after the conventional 6 DOF inertia and stiffness matrices. Moreover, the deformation of the floating body affects the hydrostatic stiffness in terms of coupling terms among 6 rigid modes and *e* elastic modes [28].

$$K_{ij}^H = \rho g \left[\iint_{S_\delta} z\vec{n}_i dS - \iint_{S_o} z\vec{n}_i dS \right] \quad (7)$$

The larger scale of the deformable body implies the more enhanced effects from the floating body's deformation in terms of added inertia and hydrostatic stiffness, which may significantly influence the natural frequencies of the system.

Modal Analysis

The modal analysis of a structure could be regarded as finding a series of deformation shapes and natural frequencies. And one can assume the total deformation of a structure can be approximated by the superposition of respective deformation shapes.

The modal analysis can be implemented by either FEM or analytic solutions. Representing a structure by the finite number of elements with free vibration condition, the structural momentum equations are formed as

$$[M]\left[\ddot{\xi}\right]+[K][\xi]=[0]. \tag{8}$$

The eigenvalues of the matrix equation are natural frequencies of the structure and Eigen functions are mode shapes, which is the deformation shape at respective eigenvalues. Once the mode shapes obtained, the diagonal modal inertia and stiffness are calculated and become diagonal elements after 6 DOFs of Eq. (6).

$$[\Xi]^T[M][\Xi]=\begin{bmatrix}\ddots & & \\ & m & \\ & & \ddots\end{bmatrix},\quad [\Xi]^T[K][\Xi]=\begin{bmatrix}\ddots & & \\ & k & \\ & & \ddots\end{bmatrix} \tag{9}$$

While the general FEM is beneficial to use for a structure with arbitrary shape, the limited number of analytic method can provide with remarkable efficiency of computation. For a slender body similar to beam or rod or a simple pontoon type body, analytic solutions are available from Beam or Plate theory. As an example, the Euler-Bernoulli Beam equation is adopted.

$$\frac{\partial}{\partial x^2}\left(EI\frac{\partial^2 w}{\partial x^2}\right)+m\frac{\partial^2 w}{\partial t^2}=q(x)r(t) \tag{10}$$

The *m* is mass distribution, and the bending stiffness *EI* can vary along the *x* axis. The deflection of the floating body *w* is induced by the distributed loads *q(x)r(t)*. It is BVP, where the end conditions are the boundaries. For free-free end conditions, which are zero shear force and bending moment at the ends,

$$w(x,t)=\sum_{j=1}^{\infty}a_j(t)\Xi_j(x),$$
$$\frac{\partial^2 w}{\partial x^2}=0 \ and \ \frac{\partial}{\partial x}\left(EI\frac{\partial^2 w}{\partial x^2}\right)=0, \qquad (11)$$

and the mode shapes are expressed as

$$\Xi_{om}=\frac{1}{2}\left(\frac{\sin k_{om}\cdot x}{\sin k_{om}}+\frac{\sinh k_{om}\cdot x}{\sinh k_{om}}\right), \ where \ om=1,3,5,7$$
$$\Xi_{em}=\frac{1}{2}\left(\frac{\cos k_{em}\cdot x}{\cos k_{em}}+\frac{\cosh k_{em}\cdot x}{\cosh k_{em}}\right), \ where \ em=2,4,6,8 \qquad (12)$$
$$where \ \ k_{om,em} \text{ are roots of } (-1)^{om,em}\tan k_{om,em}+\tanh k_{om,em}=0.$$

Multiplying the homogeneous governing equation of Eq. (10) by the mode shapes and integrating along with *x* axis, the modal inertia, stiffness, and excitation of respective elastic modes are obtained.

$$\int_x m\Xi_k{}^2(x)dx\cdot\ddot{a}_k(t)+\int_x EI\Xi_k{}''''(x)\Xi_k(x)dx\cdot a_k(t)=\int_x q(x)\Xi_k(x)dx\cdot r(t), \qquad (13)$$
$$\text{where } k=1,...,e.$$

It is seen that the mode shapes are dependent on the boundary conditions. Contrary to the beam theory, the three dimensional plate has fewer analytic solutions available. Leissa explained various types of available analytic solutions with experimental comparisons [26]. In case of an arbitrary shape structure, the general FEM is applicable.

The modal resultants such as modal inertia, modal stiffness, mode shapes, and natural frequencies are prerequisite of the hydroelastic analysis. Once they are clarified, the extended BVP is solved and the hydroelastic dynamic motion responses are achieved from the extended system of motion equations.

Hydroelastic Structural Analysis

Subsequently to the hydroelastic dynamic analysis, the fully coupled dynamic stress resultants are achieved by the hydroelastic structural analysis. The motion responses from the hydroelastic dynamic analysis entail that the inertia and restoring loads distributed over the deformable floating body are procurable. With the known fluid pressure fields, all the clarified loads provides with the dynamic stress resultants such as shear forces, bending moments, and torsional moments by the equilibrium between loads and stress resultants.

A deformable floating structure with a shallow draft in general has dominant vertical loads on the horizontal plane, and the stress resultants with respect to the horizontal axes are significant. Considering the x and y axes as the principle axes, the global structural analysis for the hydroelasticity is explained with respect to the x and y axes. On each axis, vertical shear forces, bending moments, and torsional moments are investigated.

First, the loads acting on the body can be categorized into two types: external loading and internal loading. The total hydrodynamic pressures induced by the total velocity potential is regarded as external loading, and the inertia and restoring loads induced by the dynamic motions are considered as the counteracting internal loads. The internal and external loads are balanced one another.

With all clarified loads, the shear forces V and bending moments M are achieved by the single integral and double integral of the loads p along the respective principle axes. The torsional moments T are the integration of the sectional torques along the

principle axes. Taking advantages of the frequency domain analysis, the total hydrodynamic pressures are utilized instead of decomposition of the respective types of velocity potentials. It provides less terms to deal with in further calculations. On the contrary, the time domain entails the complexity to deal with the hydrodynamic pressures due to impulse theory, and the new methodology is developed in this study to enable the time-domain hydroelastic structural analysis beyond the conventional limited method. The details of the time domain hydroelastic structural analysis are addressed in the next chapter of the time domain.

$p_E = p(x, y, z, \omega)_t$, where p_t is total hydrodynamic pressures.

$$p_I(x, y) = -m\left\{\ddot{X}_3 - x \cdot \ddot{X}_5 + y \cdot \ddot{X}_4 + \sum_{k=1}^{e} \ddot{w}_k(x, y, t)\right\},$$
$$p_R(x, y) = -\rho g\left\{X_3 - x \cdot X_5 + y \cdot X_4 + \sum_{k=1}^{e} w_k(x, y, t)\right\}. \quad (14)$$

Based on the body coordinate system of the 6-DOF floating body, the shear forces are given by the single integral of the vertical loads along with the surge direction for the *x* axis and the sway direction for the *y* axis. The boundaries of the structure are assumed to be free shear forces.

$$V(x, y) = \int_{x,y}\int_{y,x} p_{E+I+R}(\tau, \zeta)\, d\tau d\zeta \quad (15)$$

The bending moments are obtained with respect to the pitch direction for the *x* axis and the roll direction for the *y* axis. It is a summation of the double integral of the vertical loads and the existing all bending moments on the floating body. In other words, the pitch moments for the *x* axis or roll moments for the *y* axis induced by the other loads than the vertical loads need to be included.

$$
\begin{aligned}
&M(x,y) = M_0 + M_{R+I}(x,y) + \int_{x,y} V(\zeta)\, d\zeta, \\
&\text{where } M_0 = M_{-L_{x,y}/2}\delta_{x,y}(\zeta + L/2) + M_{L_{x,y}/2}\delta_{x,y}(\zeta - L/2), \\
&M_I(x,y) = c\int_{x,y} CG_z m(\zeta)\ddot{X}_{1,2}\, d\zeta, \text{ where } c = -1 \text{ for } x \text{ and } c = 1 \text{ for } y, \\
&M_R(x,y) = -\int_{x,y} \left(\rho g \forall(\zeta) CB_z - m(\zeta) g CG_z\right)\ddot{X}_{5,4}\, d\zeta.
\end{aligned}
\tag{16}
$$

In addition to the bending moments induced by the vertical loads, which is the single integral of the shear forces, there exist additional components. Horizontal pressures acting on the side walls of the floating structures generate the bending moments M_0. Gravitational effects also generate the inertia-induced bending moments M_I and the restoring-induced bending moment M_R.

The torsional moments have reverse directions. The roll moments are the torsional moments for the x axis stress resultants, and the pitch moments are the torsional moments for the y axis. With the free torque condition at the boundaries,

$$
\begin{aligned}
&T(x,y) = \int_{x,y}\left[\int_{y,x} p_{E+I+R}(x,y)\cdot\tau\, d\tau + T^{x,y}_{0+I+R}(\zeta)\right] d\zeta, \text{ where} \\
&T^{x,y}_0 = M_{-L_{y,x}/2}(x,y)\cdot\delta_{y,x}(\zeta + L_{y,x}/2) + M_{L_{y,x}/2}(x,y)\cdot\delta_{y,x}(\zeta - L_{y,x}/2), \\
&T^{x,y}_I = c\int_{y,x} CG_z m_{x,y}(\zeta)\ddot{X}_{2,1}\, d\zeta, \text{ where } c = 1 \text{ for } x \text{ and } c = -1 \text{ for } y, \\
&T^{x,y}_R = -\int_{y,x}\left(\rho g \forall_{x,y}(\zeta) CB_z - m_{x,y}(\zeta) g CG_z\right)\ddot{X}_{4,5}\, d\zeta.
\end{aligned}
\tag{17}
$$

The vertical loads induce the torsional moments, and horizontal hydrodynamic pressures generate T^0. The gravitational effects cause the inertia and restoring induced torsional moments, T^I and T^R.

The three types of stress resultants for the x and y axes are achieved by the series of surface integrals above and the frequency domain hydroelastic structural analysis subsequently provides the respective components as well as the total stress resultants as

functions of space and frequency. They include all the dynamic effects without any artificial restrictions or unrealistic simplification and all loads acting on the deformable floating body are correctly included without missing any components. Especially comparing with the classic plate theory method, the horizontal wall and gravitational effects are fully considered, which are normally ignored in the plate theory method.

The components of the stress resultants are clarified by the governing equations of motion, based on the equilibrium of loads and stress resultants and the following verifying methods are developed.

As the first phase of verifications, the componential comparison is utilized between the stress resultants at the ends and the body forces and moments. For instance, the shear force at both ends should be coincided with the heave forces, and the torsional moments at the ends are identical to the roll moments for the x axis and the pitch moments for the y axis. One caution is needed for the bending moments. The bending moments are, simply speaking, counteracting moments of the total moments acting on the body with respect to the measuring points. In other words, the bending moments along the x or y axes are measured at the instant reference position rather than the fixed center of body coordinate system. Therefore, it is incorrect to compare the bending moments at the ends directly against the pitch moments for the x axis and the roll moments for the y axis.

To complete the robust verification, the second validation method is contrived. The stress resultants are compared between the frequency domain and time domain by the Fourier Transform in terms of the total and componential stress resultants.

3. HYDROELASTICITY IN TIME DOMAIN

In company with the frequency domain-based hydroelasticity, this study completes the time-domain hydroelastic analysis for both dynamic motion responses and stress resultants of a deformable floating body in the random sea. The time domain allows including the nonlinearities of waves or any other irregular impacts. Moreover, it can be coupled with the nonlinear dynamics of the mooring lines and risers or any other dynamic units such as wind turbines and wave energy converters.

Contrary to the frequency domain hydroelasticity, a few researchers investigated about the time domain hydroelastic analysis. Kashiwagi [19] and Lee and Choi [25] solved transient hydroelastic motion responses in the time domain and the fully coupled hydroelastic structural analysis is rarely solved in the time domain. In this study, the conventional time-domain hydroelastic dynamic analysis is first explained and the new methodology is developed for the direct time-domain hydroelastic structural analysis without the DNS and CFD.

Hydroelastic Dynamic Analysis

The floating body in random seas can be explained by the impulse response theory. The irregular excitations of the random seas can be regarded as the impact at the instantaneous time step. To solve the impact-induced responses, the impulse response function including the convolution integral is adopted [5].

$$\Phi_j = \dot{X}_j \psi_j + \int_{-\infty}^{t} \varphi_j(t-\tau)\dot{X}_j(\tau)d\tau \qquad (18)$$

The total velocity potential Φ_j is induced by j^{th} mode, and it consists of the unit potential for impulsive flow ψ_j and the velocity potential for the wave elevation φ_j. The assumptions of linear and small motions satisfy the Neumann boundary condition at the wet surface S_w. While the rigid body assumption implies only the 6 rigid modes are applied to the boundary condition, the hydroelasticity entails the additional elastic modes as well as the 6 rigid modes. In the time domain analysis, all the modes are the responses induced by the impact even though the response shapes such as the mode shapes or definitions of 6 DOFs are identical to those in the frequency domain.

$$\frac{\partial \Phi_j}{\partial n} = \frac{\partial \psi_j}{\partial n} = i\omega n \cdot \begin{cases} \zeta_j & \text{for } j \le 3 \\ \alpha_j \times r & \text{for } 4 \le j \le 6 \\ \Xi_j(r)\upsilon_j & \text{for } j \ge 7 \end{cases} \text{, since } \frac{\partial \varphi_j}{\partial n} = 0 \ \ on\ S_w \qquad (19)$$

The free surface boundary conditions are also satisfied. Taking the linear pressure terms from the Bernoulli equation, the governing equation is given by the system of motion equations for 6+e variables.

$$\left(M_{ij} + \Delta M_{ij}^{\infty}\right)\ddot{X}_j + K_{ij}^{H} X_j = F_i^{(1)}(t) + F_i^{C}(t), \text{ where } i, j = 1, \ldots, 6+e. \qquad (20)$$

Contrary to the governing equation in the frequency domain, the added inertia matrix at the infinite frequency ΔM^{∞} is induced by ψ, and the impulse-generated wave potential φ generates the $F^{(1)}$ and F^{c} , which is the first order wave induced excitations and the convolution integral. The convolution term presents the decaying responses. K^H is the stiffness matrix same as the frequency domain one.

To avoid the costly DNS and take advantages of the frequency-domain results, the Fourier transform based on Kramers-Kronig relations is utilized to provides the time domain added inertia term and memory effect term, ΔM^{∞} and F^{c} [31].

$$
\begin{aligned}
R_{ij}(t) &= \frac{2}{\pi}\int_0^{\infty} B_{ij}(\omega)\cos(\omega t)d\omega \cong \frac{2}{\pi}\int_0^{\omega_{\max}} B_{ij}(\omega)\cos(\omega t)d\omega, \\
\Delta M_{ij}^{\infty} &= \Delta M_{ij}(\omega_{\max}) + \int_0^{\infty} R_{ij}(t)\frac{\sin(\omega_{\max} t)}{\omega_{\max}}dt \\
&\cong \Delta M_{ij}(\omega_{\max}) + \int_0^{t_{\max}} R_{ij}(t)\frac{\sin(\omega_{\max} t)}{\omega_{\max}}dt, \\
F_i^{C}(t) &= -\int_{-\infty}^{t} R_{ij}(t-\tau)\dot{X}_j(\tau)d\tau = -\int_{-t}^{\infty} R_{ij}(\tau)\dot{X}_j(t-\tau)d\tau \\
&= -\int_0^{\infty} R_{ij}(\tau)\dot{X}_j(t-\tau)d\tau \cong -\int_0^{t_{\max}} R_{ij}(\tau)\dot{X}_j(t-\tau)d\tau.
\end{aligned}
\qquad (21)
$$

In order to achieve the accurate time domain analysis by Eqs (20) and (21), the infinite integrals are approximated by the equivalent finite integrals. The retardation function *R* would be integrated until the negligible damping coefficients along with the frequency in that the higher frequency generates the less radiation damping. Infinite-frequency added inertia ΔM^{∞} is integrated until the values converge. The given retardation function provides the convolution term and the second term in the added inertia formula by integral until the negligible integrand.

In dimension wise, retardation functions need to be formed for $(6+e)^2$ modes to include full interactions among rigid and elastic modes. The corresponding added inertia and convolution terms also have the identical dimension. As prerequisite to assure the accuracy, it is recommended to conduct the convergence tests for the terms above.

The impulse excitations of the random sea are the superposition of a series of wave excitations of different frequencies and phases at instant time. Furthermore,

considering the importance of high or low frequency regions, the second order wave excitations of sum and different frequencies can be involved by the two-term Volterra series once the complete or approximate the second order excitations available [21, 22].

Solving the Eq. (20) with all known coefficients, the random sea-induced hydroelastic dynamic motion responses are achieved. The derivation of the governing equation implies that the hydroelastic dynamic analysis has cross-correlation between the time domain and frequency domain. Such a correspondence enables to verify the developed hydroelastic dynamic analysis on both domains such that the spectral RAOs calculated from the time domain responses should be well coincided with counterparts in the frequency domain.

Hydroelastic Structural Analysis

Conventional methods to achieve the dynamic stress resultants induced by the random seas are limited. Although the most straightforward one is the DNS or CFD including the coupled fluid and structure dynamics, it is infeasible to be employed for the random sea problems. For the time-domain hydroelasticity of random seas, it is general to implement static analysis or use un-coupled hydrodynamic loads or deflection relation for the dynamic cases. Such limited methods or further simplifications generally cause the accuracy loss and provide insufficient knowledge for the deformable floating body in the structural safety and fatigue life.

In this study, the direct time-domain hydroelastic structural analysis is developed as the new methodology to achieve the fully coupled dynamic stress resultants for the random seas. It is overwhelmingly efficient and feasible in computing and compatible to

further integration with other dynamic units such as mooring lines, risers, wind turbines and wave energy converters. The new methodology is derived after introducing the limitation of the deflection-based conventional method.

A common method to calculate the stress resultants in time domain is adopting the stress-deflection relationship. Starting from the Hooke's law, the normal stress σ is proportional to strain ε by Young's modulus E, and the bending moment M is a surface integral of the bending stress over the cross section A.

$$\begin{aligned} &\sigma = -Ez\kappa \ \because \varepsilon = -z\kappa, \text{ where } \kappa \text{ is the curvature of deflection,} \\ &M = \int_A z\sigma dA = EI\kappa. \end{aligned} \tag{22}$$

The curvature gets approximated by the negligible deflection slope as

$$\kappa = \frac{\dfrac{d^2w}{dx^2}}{\left[1+\left(\dfrac{dw}{dx}\right)^2\right]^{3/2}} \cong \frac{d^2w}{dx^2}, \tag{23}$$

and it gives relationship between deflection and bending moment. Subsequently, the shear force is also expressed by the deflection, based on equilibrium relationships among loads, shear force, and bending moment as

$$M = EI\frac{d^2w}{dx^2} \text{ and } V = \frac{dM}{dx} = EI\frac{d^3w}{dx^3}. \tag{24}$$

Although this method is convenient to use, there exist multiple drawbacks. First, it is affected by the assumption of the small deflection slope. For the high order of the elastic modes with remarkable fluctuation or the low order of elastic modes under the resonance, the assumption may not be satisfactory and it entails erroneous stress

resultants. Moreover, the method would not be sufficient unless all the loading effects to the deflection are considered without any missing components. In the general hydroelastic analysis, beam theories [36] or plate theories [20] for the modal analysis are commonly used and it tends to exclude the horizontal pressures and gravitational effects, which could be significantly large and dominant factors of the stress resultants [13]. Therefore, the incomplete deflection would induce the corresponding accuracy loss of stress resultants.

In order to secure accuracy over the deflection-based classic method, the direct time-domain hydroelastic structural analysis for the random sea is newly developed.

As described in the frequency-domain hydroelastic structural analysis, the equilibrium between the loads and stress resultants is applicable, but the complexity of terms in the time-domain hydroelastic analysis requires further derivations in order to utilize the equilibrium. The complexity is mainly due to the impulse-induced added inertia term and decaying energy term in Eq. (21), which are not straightforward to convert to the distributed loads from the body loads. The body loads mean the forces and moments given as lumped loading with respect to the body coordinate system.

To extract the distributed loads from the impulse-related terms, the Fubini's theorem is adopted. Fubini, the Italian mathematician, proved that if the integrand is measurable regardless of the continuity, the order of integrals is exchangeable [9, 35].

$$f(x,y)=g(x)h(y),\ \text{where}\ f(x,y)\ \text{is a}\ A\times B\ \text{measurable function,}$$
$$\int_A g(x)dx\int_B h(y)dy=\int_A\left(\int_B g(x)h(y)dy\right)dx=\int_B\left(\int_A g(x)h(y)dx\right)dy \qquad (25)$$
$$=\int_{A\times B} f(x,y)d(x,y).$$

The Fubini's theorem enables to reformulate the two impulse-related terms so that the corresponding distributed added inertia and convolution term are given as functions of space and time.

In detail of the added inertia at the infinite frequency, it has multiple integrals of the hydrodynamic pressures *P*, which are induced by the radiation potential.

$$\Delta M_{ij}^{\infty}=\Delta M_{ij}^{\infty}(\omega_{\max})$$
$$+\int_0^{\infty}\left\{\frac{2}{\pi}\int_0^{\infty}\left(\iint_{S_W}\left[P_j^{\mathrm{Im}}(\omega,r)\cdot n_i\right]ds\right)\cos(\omega t)d\omega\right\}\frac{\sin(\omega_{\max}t)}{\omega_{\max}}dt \qquad (26)$$

The series of order manipulations of the integrals to put the surface integral at the last give the distributed added inertia f^A over the wetted surface.

$$f^A(r)=\ddot{X}_j(r,t)\left(\begin{array}{l}P_j^{\mathrm{Re}}(\omega_{\max},r)+\\ \int_0^{\infty}\left(\frac{2}{\pi}\int_0^{\infty}\left[P_j^{\mathrm{Im}}(\omega,r)\cos(\omega t)\right]d\omega\right)\frac{\sin(\omega_{\max}t)}{\omega_{\max}}dt\end{array}\right) \qquad (27)$$

The distributed convolution term f^C is also obtained by the integral order manipulations.

$$f^C(r,t)=-\int_0^{\infty}\left(\frac{2}{\pi}\int_0^{\infty}\left[P_j^{\mathrm{Im}}(\omega,r)\cos(\omega\tau)\right]d\omega\times\dot{X}_j(t-\tau)\right)d\tau \qquad (28)$$

The hydroelastic structural analysis for the random sea has the *j* up to 6+*e* modes. The distributed loads are acting on the boundary elements in respective normal directions.

The two complicated terms are decomposed into the distributed loads, and it allows the direct structural analysis by equilibrium of loads and stress resultants as given in Eqs. (15), (16), and (17), since all the loads acting on the deformable floating body in the random seas can be clarified.

Other loading components are identified from the governing equation of the time domain hydroelastic dynamic analysis and reformulated into the distributed loads. The remaining terms are inertial, restoring, and wave excitation loads, and it is straightforward to convert it to the distributed forms.

From the hydrodynamic pressures P^D induced by the diffraction potential, the wave excitations can be formulated in the distributed manner by superposing the hydrodynamic pressures P^D at each boundary element cross a range of wave frequencies.

$$f^1(r,t) = \mathrm{Re}\left[\sum_{j=1}^{N} Amp_j P_j^D(r,t) e^{-i(\omega_j t+\alpha_j)}\right] \qquad (29)$$

The N frequencies are superposed with the disturbed phase α_j to generate the random sea-induced excitations. The phase disturbance is purposed to prevent from repetitive pattern over certain time duration.

Following decomposition of the external loads, the inertia and restoring loads are reformulated into the distributed forms. It is overall similar to those in the frequency domain except for the response type. In the time domain, the motion responses substituted in the loading formulas are time series induced by the random seas.

The hydroelastic dynamic motion responses generate the inertia loading f^I and restoring loading f^R and the loads are expressed by the kinematics of the deformable floating body

$$
\begin{aligned}
f^I(x,y) &= -m\left\{\ddot{X}_3 - x\cdot\ddot{X}_5 + y\cdot\ddot{X}_4 + \sum_{k=1}^{e}\ddot{w}_k(x,y,t)\right\},\\
f^R(x,y) &= -\rho g\left\{X_3 - x\cdot X_5 + y\cdot X_4 + \sum_{k=1}^{e} w_k(x,y,t)\right\}.
\end{aligned}
\qquad (30)
$$

Similarly to the frequency domain, the time domain inertia and restoring loads have the additional terms induced by the gravitational effects. With the center of gravity *CG*, the center of buoyance *CB*, and the position vector *r*,

$$
\begin{aligned}
&g_k^I(r,t) = dm(r)\left[CG\times\ddot{X}(t)\right]_k, \text{ where } k = 4,5,6,\\
&g_k^R(r,t) = d\forall(r)\cdot\rho g\left[\left(CB_Z - CG_Z\right)X_k(t) + \left(CB_l - CG_l\right)X_6(t)\right],\\
&\text{where } k = 4,5 \text{ and } l = \begin{cases} x \text{ for } k = 4,\\ \text{y for } k = 5.\end{cases}
\end{aligned}
\qquad (31)
$$

With all the componential loads clarified, the direct hydroelastic structural analysis for the random sea is achieved. Combining the distributed internal and external loads,

$$
F^A(r,t) = f^1(r,t) + f^C(r,t) - f^I(r,t) - f^A(r,t) - f^R(r,t). \qquad (32)
$$

Substituting the distributed loads into the formulas of the stress resultants at each time step, instantaneous stress resultants are achieved.

$$
V(x,y,t) = \int_{x,y}\int_{y,x} F^A(\tau,\zeta,t)\, d\tau d\zeta \qquad (33)
$$

The bending moments have additional terms from the horizontal pressures acting on the side walls and gravitational effects of $g^{I,R}$. For the small draft,

$$
\begin{aligned}
&M(x,y,t) = M_0 + M_{R+I}(x,y,t) + \int_{x,y}\int_{y,x} V(\tau,\zeta,t)\,d\tau\,d\zeta,\\
&\text{where } M_0 = M_{-L_{x,y}/2}\delta_{x,y}(\zeta + L/2) + M_{L_{x,y}/2}\delta_{x,y}(\zeta - L/2),\\
&M_I(x,y,t) = c\int_{x,y} CG_z m(\zeta)\ddot{X}_{1,2}(t)\,d\zeta, \text{ where } c=-1 \text{ for } x \text{ and } c=1 \text{ for } y,\\
&M_R(x,y,t) = -\int_{x,y}\left(\rho g\forall(\zeta)CB_z - m(\zeta)gCG_z\right)\ddot{X}_{5,4}(t)\,d\zeta.
\end{aligned}
\qquad (34)
$$

Subsequently, the torsional moments are given by

$$
\begin{aligned}
&T(x,y,t) = \int_{x,y}\left[\int_{y,x} F^A(x,y,t)\cdot\tau\,d\tau + T^{x,y}_{0+I+R}(\zeta,t)\right]d\zeta,\\
&\text{where}\\
&T^{x,y}_0 = M_{-L_{y,x}/2}(x,y,t)\cdot\delta_{y,x}(\zeta + L_{y,x}/2) + M_{L_{y,x}/2}(x,y,t)\cdot\delta_{y,x}(\zeta - L_{y,x}/2),\\
&T^{x,y}_I = c\int_{y,x} CG_z m_{x,y}(\zeta)\ddot{X}_{2,1}(t)\,d\zeta, \text{ where } c=1 \text{ for } x \text{ and } c=-1 \text{ for } y,\\
&T^{x,y}_R = -\int_{y,x}\left(\rho g\forall_{x,y}(\zeta)CB_z - m_{x,y}(\zeta)gCG_z\right)\ddot{X}_{4,5}(t)\,d\zeta.
\end{aligned}
\qquad (35)
$$

The shear forces, bending moments, and torsional moments for both the *x* and *y* axes are dynamic stress resultants induced by random seas. They are given as functions of time and space.

The new methodology can be robustly verified by multiple levels of validation. After checking the correctness of the decomposition process, each stress resultants at the ends or boundaries are compared against the body loading terms similarly to the frequency domain. Subsequently, the stress resultants at certain spatial point should be coincided in both time and frequency domains in RAO. Similarly to the dynamic responses, the governing equations of the structural analysis in both domains represent correspondence, and thus the spectral RAO of stress resultants from the time domain should match with those in the frequency domain.

This methodology has notable advantages such that the computing cost is remarkably efficient in comparison with DNS or CFD, it includes all irregular loads acting on the deformable floating body in the random seas, and thus the accuracy is assured with efficiency. Moreover, it is compatible to further applications in order to couple with other dynamic units.

Considering that this method does not require the deflection, it is also applicable to the rigid-assumed floating body undergoing the random seas. For instance, this method can provide the fully coupled dynamic stress resultants for the moored FLNG in the random sea on the assumption of the rigid body.

Hydroelastic Analysis with Simplified Second-Order Loads

Although the main environmental loads from waves are induced by the linear order waves, the second order wave loads for sum and difference frequencies are indispensable in that the resonance in the low or high frequency regions may occur. The complete second order diffraction wave theory and floating body interactions are achieved by Kim and Yue [21, 22]. The floating body is assumed as a rigid body. The second order hydroelasticity is rarely investigated and the complete second order hydroelastic analysis does not exist yet. In this study, as a simplified method, the rigid-body induced complete second order wave loads are applied into the hydroelastic dynamic analysis.

The sum and difference-frequency wave loads are calculated by solving the second order BVP derived from the perturbation theory and added into the wave excitation terms by the two-term Volterra series [22].

$$F = F_i^{(1)}(t) + F_i^{C}(t) + F_i^{(2)}(t), \text{ where } i = 1, \ldots, 6 + e.$$

$$F_i^{(2)}(t) = \begin{cases} \mathrm{Re}\sum_a^N \sum_b^N \left[A_a A_b^* \overline{F}_{ab}^{l-} e^{i(\omega_a - \omega_b)t} + A_a A_b^* \overline{F}_{ab}^{l+} e^{i(\omega_a + \omega_b)t} \right], \; if \; i < 7 \\ 0, \; if \; i > 6 \end{cases} . \quad (36)$$

Even though the second order wave loads are applied only for the rigid modes with zeros for the elastic modes, the simplified method can capture the elastic excitations in the high-frequency due to the sum-frequency waves and low frequency due to the difference-frequency. Subsequently, the 2nd order wave loading induced resonance phenomena in the 6 rigid and *e* elastic modes can be investigated in consideration of the approximation error.

4. HYDROELASTICITY COUPLED WITH NONLINEAR MOORING-RISER DYNAMICS

With the enlarged scale of offshore structures, the mooring lines and risers may interact with the deformation of the floating body significantly. To address the moored deformable body correctly, the new extended hydroelastic analysis is developed in this study. In the time domain, the hydroelastic analysis of the deformable floating body is fully coupled with the nonlinear mooring-riser dynamics. The nonlinear dynamics of the mooring lines and risers are modeled by the FEM based on the rod dynamics, and thus the overall system can be regarded as combination of BEM and FEM.

Beyond the conventional hydroelastic analysis for the freely floating or constant forward speed condition, the new methodology achieves the hydroelastic dynamic motion responses and stress resultants interacting with the nonlinear mooring-risers and the deformable floating body.

The simplified 2nd order wave loads can be applied by the two-term Volterra series to investigate the nonlinear-wave induced interactions among the deformable floating body dynamics and nonlinear mooring-riser dynamics.

Hydroelastic Dynamic Analysis Coupled with Mooring Lines and Risers

The hydroelasticity of the floating body is solved by the BEM as described in the preceding chapters, and the mooring-riser dynamics is solved by the finite rod element method including the hydrodynamic loads on the rod. The interaction of the mooring-riser with surrounding local fluids is ignored.

Rod Dynamics

The nonlinear mooring-riser dynamics can be solved by the finite rod element method, which represent the slender bar under axial and bending deformations [10, 32]. The momentum equation along with the rod is

$$\begin{aligned} &-\left(Br''\right)'' + \left(\lambda r'\right)' + q = \rho \ddot{r}, \\ &\text{where } \lambda = T - B\kappa^2 \text{ and } \kappa \text{ is the curvature.} \end{aligned} \tag{37}$$

B is bending stiffness and T is effective tension including the hydrostatic effect on the rod with the small extensible condition. In case of largely extensible rod, the momentum equation needs an additional term to include the complete extensibility effect [1]. The rod dynamics satisfies a constraint equation for the small extensibility.

$$\frac{1}{2}\left(r'r' - 1\right) = \frac{T}{AE} \cong \frac{\lambda}{AE} \tag{38}$$

To solve the rod dynamics, the Galerkin finite element is adopted, which takes identical weight functions to the interpolation or shape functions. Assuming the r and λ can be expressed by the known cubic interpolation A and quadratic interpolation P,

$$\begin{aligned} &r_j(s,t) = A_i(s)U_{ji}(t), \\ &\lambda(s,t) = P_m(s)\lambda_m(t). \end{aligned} \tag{39}$$

The weighted residual should be zero for the small finite element length L.

$$\begin{aligned} &\int_0^L \left[-\left(Br_j''\right)'' + \left(\lambda r_j'\right)' + q_j - \rho \ddot{r}_j \right] \delta r_j ds = 0, \\ &\int_0^L \left[\frac{1}{2}\left(r_k'r_k' - 1\right) - \frac{\lambda}{AE} \right] \delta\lambda ds = 0 \end{aligned} \tag{40}$$

The unknown parameters U and λ are automatically defined by the types of interpolation functions as

$$
\begin{aligned}
&U_{j1}(t) = r_j(0,t),\ U_{j2}(t) = r_j'(0,t),\\
&U_{j3}(t) = r_j(L,t),\ U_{j4}(t) = r_j'(L,t),\\
&\lambda_1(t) = \lambda(0,t),\ \lambda_2(t) = \lambda\left(L/2, t\right),\ \lambda_3(t) = \lambda(L,t).
\end{aligned}
\tag{41}
$$

Substituting all the coefficients, known formulas, and unknown variables, the rod dynamics is solved in terms of the 15 variables of the U and λ for every element.

Coupling Rod Dynamics with Deformable Floating Body Dynamics

The coupling of the rod dynamics and floating body dynamics can be made by spring or damper connection at the interface as shown in Figure 1.

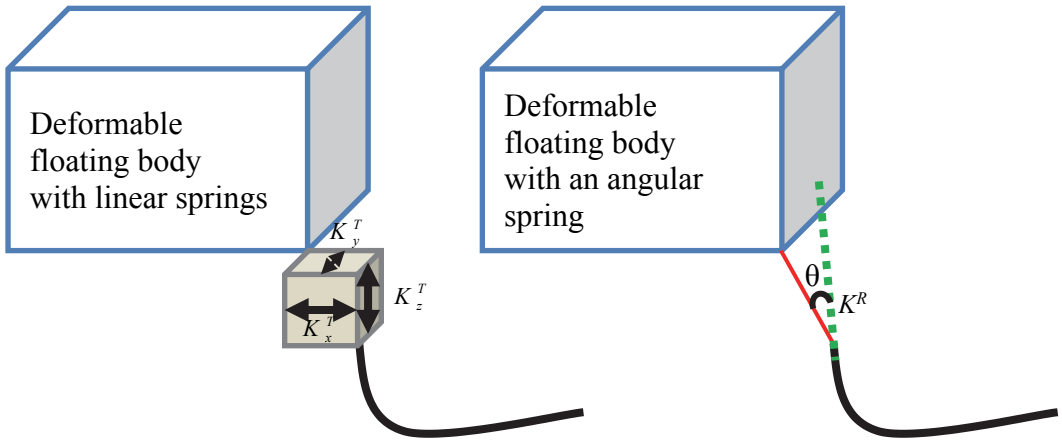

Figure 1. Schematic view of coupling between floating body and mooring-riser system

Assuming the 3 translational springs and 1 rotational spring at the connection, the reaction loads from the connection are induced in terms of 3 translational forces N and 3 rotational moments L.

$$N = K^T\left(\zeta + p + \alpha \times p + \upsilon_j \Xi_j(p) - r\right),$$
$$L = K^R\left(\bar{e} + \alpha \times \bar{e} - \frac{r'}{|r'|}\right) \quad (42)$$

The p is the position vector of the fairlead point with respect to the body coordinate system, $\bar{e}$ is the direction of the spring from the fairlead point, and r is the global coordinates of the connecting boundary of the rod element. The connection-induced reaction loads are given with respect to the coordinate system of the rod.

The reaction loads are regarded as external loads to the deformable floating body, and thus further coordinate transformation is needed. The translational forces to the floating body F have opposite direction as counteracting forces of the springs.

$$F = -N = -K^T\left(\zeta + p + \alpha \times p + \upsilon_j \Xi_j(p) - r\right) \quad (43)$$

The moments with respect to the body M are induced by the moment arms of the position vector.

$$M = p \times F + \bar{e} \times L \quad (44)$$

In addition, the forces generate modal excitations E for the respective elastic deformations.

$$E_j = \Xi_j(p)F \quad (45)$$

Numerical Solution

In time domain simulation, the solution at the next step can be estimated by the Taylor series of the previous step solution. Applying the first order Taylor expansion to the reaction loads at the rod, the next step is expressed by the Jacobian matrix.

$$N_i^{n+1} = N_i^n + \frac{\partial N_i}{\partial r_j}\Delta r_j + \frac{\partial N_i}{\partial \zeta_j}\Delta\zeta_j + \frac{\partial N_i}{\partial \alpha_j}\Delta\alpha_j + \frac{\partial N_i}{\partial \upsilon_j}\Delta\upsilon_j,$$
$$L_i^{n+1} = L_i^n + \frac{\partial L_i}{\partial r'_j}\Delta r'_j + \frac{\partial L_i}{\partial \alpha_j}\Delta\alpha_j, \qquad (46)$$
where $i = 1, 2, 3.$

Substituting the N into respective gradient terms,

$$K_{ij}^{rr} = -\frac{\partial N_i}{\partial r_j} = K_i^T\delta_{ij}\ ,\ K_{ij}^{r\zeta} = -\frac{\partial N_i}{\partial \zeta_j} = -K_i^T\delta_{ij}\ ,$$
$$K_{ij}^{r\alpha} = -\frac{\partial N_i}{\partial \alpha_j} = K_i^T C_{ij}, K_{ij}^{r\upsilon} = -\frac{\partial N_i}{\partial \upsilon_j} = -K_i^T\Xi_j(p_i), \qquad (47)$$
where $C_{ij} = \begin{bmatrix} 0 & -p_3 & p_2 \\ p_3 & 0 & -p_1 \\ -p_2 & p_1 & 0 \end{bmatrix}.$

The L gradients are

$$K_{ij}^{r'r'} = -\frac{\partial L_i}{\partial r_j} = K^R\left[\frac{\delta_{ij}}{\left(r'_m r'_m\right)^{1/2}} - \frac{r'_i r'_j}{\left(r'_n r'_n\right)^{3/2}}\right], K_{ij}^{r\alpha} = -\frac{\partial L_i}{\partial \alpha_j} = K_i^R D_{ij}, \qquad (48)$$
where $D_{ij} = \begin{bmatrix} 0 & -\overline{e}_3 & \overline{e}_2 \\ \overline{e}_3 & 0 & -\overline{e}_1 \\ -\overline{e}_2 & \overline{e}_1 & 0 \end{bmatrix}.$

The reaction loads acting on the deformable floating body have the Jacobian matrix for the excitation loads of the total 6 + e modes.

$$F_i^{n+1} = F_i^n + \frac{\partial F_i}{\partial \zeta_j}\Delta\zeta_j + \frac{\partial F_i}{\partial \alpha_j}\Delta\alpha_j + \frac{\partial F_i}{\partial \upsilon_j}\Delta\upsilon_j + \frac{\partial F_i}{\partial r_j}\Delta r_j$$
$$M_i^{n+1} = M_i^n + \frac{\partial M_i}{\partial \zeta_j}\Delta\zeta_j + \frac{\partial M_i}{\partial \alpha_j}\Delta\alpha_j + \frac{\partial M_i}{\partial \upsilon_j}\Delta\upsilon_j + \frac{\partial M_i}{\partial r_j}\Delta r_j + \frac{\partial M_i}{\partial r'_j}\Delta r'_j \qquad (49)$$
$$E_i^{n+1} = E_i^n + \frac{\partial E_i}{\partial \zeta_j}\Delta\zeta_j + \frac{\partial E_i}{\partial \alpha_j}\Delta\alpha_j + \frac{\partial E_i}{\partial \upsilon_j}\Delta\upsilon_j + \frac{\partial E_i}{\partial r_j}\Delta r_j$$

Substituting the F, M, and E into the gradients,

$$
\begin{aligned}
K_{ij}^{\zeta\zeta} &= -\frac{\partial F_i}{\partial \zeta_j} = K_i^T \delta_{ij}, & K_{ij}^{\zeta\alpha} &= -\frac{\partial F_i}{\partial \alpha_j} = K_i^T C_{ji}, \\
K_{ij}^{\zeta\upsilon} &= -\frac{\partial F_i}{\partial \upsilon_j} = K_i^T \Xi_j(p_i), & K_{ij}^{\zeta r} &= -\frac{\partial F_i}{\partial r_j} = -K_i^T \delta_{ij}, \\
K_{ij}^{\alpha\zeta} &= -\frac{\partial M_i}{\partial \zeta_j} = K_j^T C_{ij}\ , & K_{ij}^{\alpha\alpha} &= -\frac{\partial M_i}{\partial \alpha_j} = K_k^T C_{kj} C_{ki} + K^R D_{ki} D_{kj}, \\
K_{ij}^{\alpha\upsilon} &= -\frac{\partial M_i}{\partial \upsilon_j} = K_k^T \Xi_j(p_k) C_{ik}, & K_{ij}^{\alpha r} &= -\frac{\partial M_i}{\partial r_j} = -K_j^T C_{ij}, \\
K_{ij}^{\alpha r'} &= -\frac{\partial M_i}{\partial r_j} = K^R D_{ji}, & & \\
K_{ij}^{\upsilon\zeta} &= -\frac{\partial E_i}{\partial \zeta_j} = K_j^T \Xi_i(p_j)\ , & K_{ij}^{\upsilon\alpha} &= -\frac{\partial E_i}{\partial \alpha_j} = K_k^T C_{jk} \Xi_i(p_j)\ , \\
K_{ij}^{\upsilon\upsilon} &= -\frac{\partial E_i}{\partial \upsilon_j} = K_k^T \Xi_j(p_k) \Xi_i(p_k), & K_{ij}^{\upsilon r} &= -\frac{\partial E_i}{\partial r_j} = -K_j^T \Xi_i(p_j).
\end{aligned}
\tag{50}
$$

Solving the governing equation of the time-domain hydroelastic dynamic analysis coupled with mooring-riser, the combined matrix equation is formed by assembling all the equations of motions for the rod and deformable floating body. The reaction loads, N, L, F, M, and E, are applied into the right hand side as external excitations acting on the rod and floating body, respectively. Since the reaction loads are unknown in the every time step to solve, the approximate values derived by the first order Taylor series are substituted into the right hand side. Subsequently, the unknown Jacobian matrix or gradients of the approximation are placed on the left hand side and considered as additional stiffness coefficients for respective mode combinations.

As an example of the total stiffness matrix for the moored deformable floating body in Figure 2, a series of sub-matrices is formed to the number of finite rod elements,

K_{Rn}, the Jacobian matrices are substituted into the coupled off-diagonal terms, K_C, and the deformable body's stiffness matrix is given as K_B. Contrary to the rigid-assumed coupled analysis, the floating matrix is extended to 6+e DOFs where the hydrostatic coefficient revisions due to the deformation are given in the off-diagonal terms K_{6xe} and K_{ex6}. The diagonal sub-matrices of the K_B also include the hydrostatic stiffness coefficients as well as external stiffness in K_{6x6} and modal stiffness in K_{exe}.

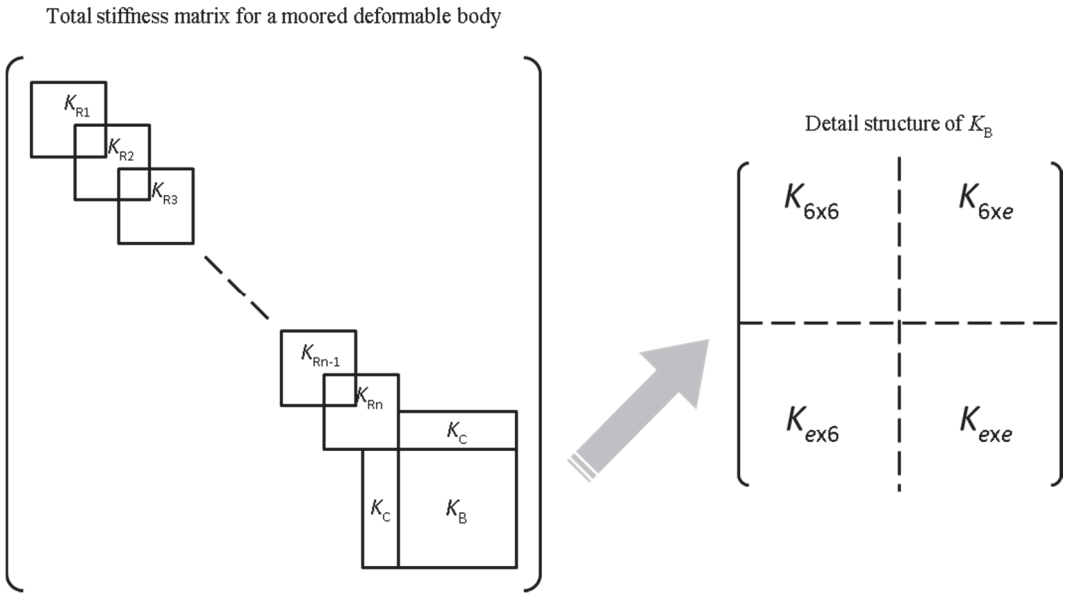

Figure 2. Example of total stiffness matrix of a moored deformable floating body

With all the diagonal and off-diagonal stiffness terms in the left hand side and previous step reaction loads on the right hand side of the full equations of motions, the hydroelastic dynamic analysis coupled with the mooring-riser system is completed.

Following the derivation, verification can be made such that at every time step the inertia and restoring momentum should be balanced by the external environmental loads and mooring-riser induced loads.

Based on the developed scheme, the riser can also be included by applying soft spring or pneumatic tensioner spring and damper at the connection. In case of damping connection, the hydroelastic coupling can be derived in the similar manner to the spring connection coupling. Considering the relative importance to the hydroelasticity and its interactions, the damper effect is not considered in this study.

Hydroelastic Structural Analysis Coupled with Mooring Lines and Risers

The fully coupled hydroelastic structural analysis for the moored deformable body can be achieved by including the loads induced by the coupled mooring and riser system. The rod dynamics with spring connections generates shear forces, bending moments and torsional moments at the fairlead points. The local concentrated stress resultants are integrated along the surface integral with other componential stress resultants which are given by Eqs. (33), (34), and (35).

Since the hydroelastic dynamic analysis for the moored deformable body already includes all the interactions among the floating body, mooring-riser, and environmental loads, and the coupling effects are represented by the inertia and restoring loads of the floating body, the time-domain hydroelastic structural analysis is still valid to use except for the absence of the mooring-riser effects.

Combining the formulas with the concentrated stress resultants induced by the mooring-riser completes the hydroelastic structural analysis for the moored deformable body.

The shear forces are combination of Eq. (32) and the local heave loads induced by the mooring-riser.

$$V(x,y,t) = \int_{x,y}\int_{y,x} F^{A}(\tau,\zeta,t) + \sum_{j} F_{3}^{j}(\tau,\zeta,t)\,\delta\left(\tau - x_{j}, \zeta - y_{j}\right) d\tau d\zeta \qquad (51)$$

The bending moments have additional local pitch moments for the x axis and roll moments for the y axis from the mooring-riser dynamics $M_{5,4}$ as well as surface integral of shear forces above.

$$\begin{aligned} M(x,y,t) = &\sum_{j} M_{5,4}^{j}\,\delta\left(x - x_{j}, y - y_{j}\right) \\ &+ M_{0} + M_{R+I}(x,y,t) + \int_{x,y}\int_{y,x} V(\tau,\zeta,t)\,d\tau\,d\zeta \end{aligned} \qquad (52)$$

The torsional moments also have the additional local roll moments for the y axis and pitch moments for the x axis.

$$\begin{aligned} T(x,y,t) = &\sum_{j} M_{4,5}^{j}\,\delta\left(x - x_{j}, y - y_{j}\right) \\ &+ \int_{x,y}\left[\int_{y,x} F^{A}(x,y,t)\cdot\tau\,d\tau + T_{0+I+R}^{x,y}(\zeta,t)\right] d\zeta \end{aligned} \qquad (53)$$

The time-domain hydroelastic structural analysis for the moored deformable body provides the fully coupled dynamic stress resultants induced by the random sea and it can be further utilized for various design purposes including more accurate fatigue analyses or local structural analyses.

5. HIGH ACCURACY DYNAMIC POSITIONING SYSTEM

Offshore structures undergo dynamic environmental loads such as waves, currents, and winds, and the station keeping is one of main performances to achieve. Either the mooring system or the dynamic positioning (DP) system can be a solution based on a given situation. The mooring system is broadly used for semi-permanent station keeping of offshore platforms such as TLP, SPAR, SEMI-SUBMERSIBLE, and FPSO/FLNG. The DP system is preferable for drilling, installation, or where needs mobility of the station keeping system.

The DP control in general consists of observer, feedback control, and allocation. From random dynamic responses of an offshore structure, observer (estimator) extracts low frequency responses to control and feedback controller assesses optimal counteracting forces from the filtered responses. The allocation unit distributes counteracting forces into individual thrusters to generate the thrusts. In this study, the dynamic positioning system satisfying the high accuracy of 1~3 m watch circle is achieved by the accurate observer design, the more efficient control system structure, and the fast and generalized allocation scheme. The present study of DP is carried out on the numerical simulation.

Governing Equation

The governing equation of the high accuracy DP system for an offshore structure can be regarded as combination of general 6 DOF dynamic motion equations and 3 DOF maneuvering equations.

The 6 DOF dynamics are solved by the Cummins equation as given in Eq. (20). In the DP analysis, the hydroelasticity is not considered and thus the variables to solve are 6 DOFs. Simultaneously with the 6 DOF Cummins equation at every time step, the 3 DOF linear maneuvering equations are solved to perform the DP control.

$$\begin{aligned}
&\dot{\zeta}_1 = u, M_{11}\dot{u} = \tau_x + w_x, \\
&\dot{\zeta}_2 = v, M_{22}\dot{v} + M_{26}\dot{\omega} = \tau_y + w_y, \\
&\dot{\alpha}_3 = \omega, M_{62}\dot{v} + M_{66}\dot{\omega} = \tau_\psi + w_\psi, \\
&\text{where } M_{11} = M + \Delta M_{11}(0), M_{22} = M + \Delta M_{22}(0), \\
&M_{26} = M + \Delta M_{26}(0), M_{66} = M + \Delta M_{66}(0).
\end{aligned} \qquad (54)$$

In that the station keeping is mainly performed on the horizontal plane, the surge (ζ_1), sway (ζ_2), and yaw (α_3) are considered. The inertia M terms are balanced with thrust forces τ and environmental disturbance loads w. This is generally regarded as the low frequency model, and the DP system is built on it.

In numerical analysis, the 6 DOF dynamics represent the simulated offshore structure motions in real time and the DP system at every time step generates the optimal counteracting forces into the offshore structure to reduce large and slow-varying motions. Subsequently, the offshore structure has the controlled dynamic responses including the counteracting forces to the designated environmental loads.

Kalman Filter

In general, it is infeasible and superfluous to control all types of motions of an offshore structure during the operation. The station keeping for an offshore structure requires controlling slow-varying large amplitude motions, especially on the horizontal

plane. To extract the target responses for the surge, sway, and yaw, an observer is utilized.

Multiple methods can be used as the observer. In the early era of the DP development, the notch filter was used to filter out a specific range of wave frequencies, but it induces phase leg between the filtered responses and original responses [11]. To overcome the drawbacks of the notch filter, Kalman filter has been broadly adopted for the DP control. In 1960s, the Kalman proved that there exists a linear optimal estimator under the Gaussian white noises of the process and measurement, called Kalman filter. Although it has a name of filter, it estimates the target values at the next step from the previous step, while the notch filter extracts certain range of values from all known values at every step.

The real time estimator, Kalman filter is optimum in the linear order, and it has process noises from high frequency excitations *w* and measurement noises from measuring motion responses *υ*.

$$\begin{bmatrix} \tilde{\zeta}_1 \\ \tilde{\zeta}_2 \\ \tilde{\alpha}_3 \end{bmatrix} = \begin{bmatrix} 0 & 1 & 0 & 0 & 0 & 0 \\ 0 & 0 & 0 & 1 & 0 & 0 \\ 0 & 0 & 0 & 0 & 0 & 1 \end{bmatrix} \begin{bmatrix} u \\ \zeta_1 \\ v \\ \zeta_2 \\ \omega \\ \alpha_3 \end{bmatrix} + \begin{bmatrix} \upsilon_{\zeta_1} \\ \upsilon_{\zeta_2} \\ \upsilon_{\alpha_3} \end{bmatrix}, \tag{55}$$

To derive the Kalman filter, the maneuvering equations are reformulated in a matrix equation.

$$
\begin{aligned}
&\mathrm{M}\dot{x} = \tilde{\mathrm{A}}x + \tilde{\mathrm{B}}\tau + \tilde{\mathrm{E}}w, \text{ where} \\
&x = \begin{bmatrix} u & \zeta_1 & v & \zeta_2 & \omega & \alpha_3 \end{bmatrix}^T, \\
&\tau = \begin{bmatrix} \tau_{\zeta_1} & \tau_{\zeta_2} & \tau_{\alpha_3} \end{bmatrix}^T, w = \begin{bmatrix} w_{\zeta_1} & w_{\zeta_2} & w_{\alpha_3} \end{bmatrix}^T, \\
&\mathrm{M} = \begin{bmatrix} M_{11} & 0 & 0 & 0 & 0 & 0 \\ 0 & 1 & 0 & 0 & 0 & 0 \\ 0 & 0 & M_{22} & 0 & M_{26} & 0 \\ 0 & 0 & 0 & 1 & 0 & 0 \\ 0 & 0 & M_{62} & 0 & M_{66} & 0 \\ 0 & 0 & 0 & 0 & 0 & 1 \end{bmatrix}, \ \tilde{\mathrm{A}} = \begin{bmatrix} 0 & 0 & 0 & 0 & 0 & 0 \\ 1 & 0 & 0 & 0 & 0 & 0 \\ 0 & 0 & 0 & 0 & 0 & 0 \\ 0 & 0 & 1 & 0 & 0 & 0 \\ 0 & 0 & 0 & 0 & 0 & 0 \\ 0 & 0 & 0 & 0 & 1 & 0 \end{bmatrix}, \tilde{\mathrm{B}} = \tilde{\mathrm{E}} = \begin{bmatrix} 1 & 0 & 0 \\ 0 & 0 & 0 \\ 0 & 1 & 0 \\ 0 & 0 & 0 \\ 0 & 0 & 1 \\ 0 & 0 & 0 \end{bmatrix}.
\end{aligned}
\tag{56}
$$

Rewriting in state space representation,

$$
\begin{aligned}
&x = Ax + B\tau + Ew \\
&y = Cx + \upsilon \\
&\text{where, } y = \begin{bmatrix} \tilde{\zeta}_1 & \tilde{\zeta}_2 & \tilde{\alpha}_3 \end{bmatrix}, \\
&A = \mathrm{M}^{-1}\tilde{\mathrm{A}}, \ B = \mathrm{M}^{-1}\tilde{\mathrm{B}}, \ \ E = \mathrm{M}^{-1}\tilde{\mathrm{E}}.
\end{aligned}
\tag{57}
$$

The state space model satisfies both of the observability which presents the estimated response is unique and the controllability that represents definite feedback inputs τ can make states the target values.

The Kalman filter is derived to impose the least error on the given Gaussian and white process noises w and measurement noises υ. The filtered responses are calculated by the Kalman gains L.

$$
\begin{aligned}
&\hat{x} = [\hat{u}, \hat{\zeta}_1, \hat{v}, \hat{\zeta}_2, \hat{\omega}, \hat{\alpha}_3]^T \\
&Q = E[w \cdot w^T], \quad R = E[\upsilon \cdot \upsilon^T] \\
&\dot{\hat{x}}(t) = A\hat{x}(t) + B\tau(t) + L\left[y(t) - C\hat{x}(t) \right] \\
&\hat{x}(t + \Delta t) = \hat{x}(t) + \dot{\hat{x}}(t)
\end{aligned}
\tag{58}
$$

The L is given by P which is the solution to the algebraic Riccati equation. In this DP control, the coefficients of the state space model are constants and thus the steady-state Kalman filter is adopted.

$$\begin{aligned} &L = PC^T R^{-1}, \\ &\text{where } 0 = \dot{P} = AP + PA^T - PC^T R^{-1} CP + EQE^T. \end{aligned} \tag{59}$$

The accuracy of Kalman filtering is purely dependent on the noise covariance matrices Q and R. Those matrices determine which range of responses will be removed by the filtering, and the more correct noise covariance values will result in the more preferable responses to control.

In the present DP system, the Q corresponds to the linear wave loads except for the low frequency range, and the R represents the high-frequency motions responses.

$$Q = \begin{bmatrix} W_{\zeta_1} & 0 & 0 \\ 0 & W_{\zeta_2} & 0 \\ 0 & 0 & W_{\alpha_3} \end{bmatrix}, \quad R = \begin{bmatrix} V_{\zeta_1} & 0 & 0 \\ 0 & V_{\zeta_2} & 0 \\ 0 & 0 & V_{\alpha_3} \end{bmatrix}. \tag{60}$$

The W and V are the power spectral density of each dataset. To satisfy the assumption of Kalman filter, the arbitrary-shape spectral distribution needs to be approximated by the white noise spectral distribution.

With a correlation function $\rho(\tau)$

$$\begin{aligned} &S(\omega) = \int_{-\infty}^{\infty} \rho(\tau) e^{-i\omega\tau} d\omega, \\ &\bar{E}\left\{x^2(t)\right\} \cdot 2\pi = \int_{-\infty}^{\infty} S(\omega) d\omega \cong \int_{\omega_{\min}}^{\omega_{\max}} S(\omega) d\omega, \\ &\bar{X} = \frac{\tilde{E}\left\{x^2(t)\right\} \cdot 2\pi}{\omega_{\max} - \omega_{\min}}. \end{aligned} \tag{61}$$

The $\bar{E}$ represents the mean, and the power spectral densities for Q and R are calculated by substituting the linear wave loads and high frequency motions into the x, respectively. The power spectral densities are functions of the offshore structure shape and wave headings. In case of any other disturbances included with high frequencies, they should also be accounted.

For a given offshore structure, it could be needed to tune the noise parameters further, since the covariance matrices are simplified to the white noise from the arbitrary shape spectra and it is not straightforward to identify the disturbances for removing. It is helpful to check the filtered responses after the initial running and tune the sensitivity of the Kalman filter by manipulating the noise parameters in order to get the optimal filtering. Based on the characteristics of Kalman filter theory [3], decrease of process noises or increase of measurement make the Kalman filter less sensitive so that the more high frequency responses removed. The reverse change of the noises implies the opposite resultants.

To achieve the high accuracy from the least required energy, the tuning of the Kalman filter is essential. On the filtered responses that are the most preferable to control, the optimal feedback control is designed.

Optimal Feedback Control

The filtered responses are controlled by the feedback scheme. Although some researchers investigated on the feed-forward DP control, it is not considered in this study in that the target of this DP system is high accuracy in a short operating time and it is hard to find a well-proved feed-forward scheme.

Taking advantages of the short operating time, only displacements and velocities are under control by the PD feedback scheme. The P and D stand for "proportional" and "derivatives", separately. The optimal control is formulated on a performance integral function *J*, which means the feedback inputs to the system are the optimum with respect to the performance function.

$$J = E\left\{\int (x'Ox + \tau' N\tau)dt\right\} \tag{62}$$

The larger coefficients in matrix *O* or *N* enhance performance or efficiency, relatively. Even in each matrix, the larger coefficients imply the more sensitive modes to control. The relative scales of the coefficients represent the importance.

The state space model for the PD feedback control is generally given as

$$\dot{x} = Ax + B\tau + Ew, \tag{63}$$

and the optimal PD gain matrix *G* is driven by the least square method similarly to the optimal estimator problem.

$$\begin{aligned} &G = N^{-1}B^T M, \\ &\text{where } 0 = -\dot{M} = MA + A^T M - MBN^{-1}B^T M + O. \end{aligned} \tag{64}$$

The optimal feedback forces are

$$\tau(t) = -G\hat{x}(t). \tag{65}$$

Although the optimal estimator is herein explained first, the optimal controller had been developed earlier than the observer in the history of DP system. Furthermore, the duality between the optimal controller and observer enables to combine both as a single unit.

Separation Theorem

For the DP control of an offshore structure, the optimal estimator and optimal controller are used simultaneously, and the combined controller should keep the optimum design.

The filtered responses are input to the feedback control, and it allows combining the estimator and controller and thus solving them as a single unit process.

Defining errors as

$$e = x - \hat{x}, \tag{66}$$

the observer and controller are coupled by x and e.

$$\begin{bmatrix} \dot{x} \\ \dot{e} \end{bmatrix} = \begin{bmatrix} A-BG & BG \\ 0 & A-LC \end{bmatrix} \begin{bmatrix} x \\ e \end{bmatrix} + \begin{bmatrix} E & 0 \\ E & -L \end{bmatrix} \begin{bmatrix} w \\ \upsilon \end{bmatrix} \tag{67}$$

The separation theorem proves that the coupled control system is the optimum by taking the Kalman gain L from Eq. (59) and the optimal gain G from Eq. (64). Both gain matrices are solutions to the Riccati equations with different coefficient matrices. Therefore, along with the Kalman filter the optimum controller is adopted in the high accuracy DP system with the performance function enhancing the positioning accuracy. The detail derivations of the optimum controller can be found in [8].

Generalized Allocation

Once the optimum controller calculates the most effective counteracting forces at every time step, the input forces are distributed into the individual thrusters and they generate actual counteracting forces. During the process, the less time leg from calculation to generation of the counteracting forces implies the higher accuracy of the

positioning and efficiency of energy consumption. In this study, the generalized allocation scheme is adopted to reduce the reaction time. Although there exists popular allocation scheme based on the Lagrange method to overcome the limited dimension of three rows [7], it requires lengthy calculation and thus may generates continuous time legs and subsequent accuracy loss.

The generalized allocation scheme is derived from the pseudo inverse matrix. Assuming the n number of thrusters at respective horizontal coordinates (x_j, y_j), the total thrust loads for surge, sway, and yaw are given by the vector decomposition and superposition of respective thrusts T in the local body coordinate system.

$$\begin{bmatrix} 1 & 0 & \cdots & \cos(\alpha) & \cdots & 1 & 0 \\ 0 & 1 & \cdots & \sin(\alpha) & \cdots & 0 & 1 \\ -y_1 & x_1 & \cdots & -y_j\cos(\alpha)+x_j\sin(\alpha) & \cdots & -y_n & x_n \end{bmatrix} \begin{bmatrix} \mathbf{T}_1^x \\ \mathbf{T}_1^y \\ \vdots \\ \mathbf{T}_j \\ \vdots \\ \mathbf{T}_n^x \\ \mathbf{T}_n^y \end{bmatrix} = \begin{bmatrix} \tilde{\tau}_{\zeta_1} \\ \tilde{\tau}_{\zeta_2} \\ \tilde{\tau}_{\alpha_3} \end{bmatrix} \quad (68)$$

The first and last thrusters are assumed to be azimuth type and the azimuth angle is calculated by arctangent of the x and y thrust components of each thruster. In case of a thruster with angle fixed α in yaw direction, only single thrust force T_j is considered. The generalized allocation scheme is derived by Pseudo inverse matrix, which represents the least error [34]. Considering the DP control is given with respect to the global coordinate system,

$$\begin{bmatrix} \mathbf{T}_1^x \\ \mathbf{T}_1^y \\ \vdots \\ \mathbf{T}_j \\ \vdots \\ \mathbf{T}_n^x \\ \mathbf{T}_n^y \end{bmatrix} = P \begin{bmatrix} \cos\alpha_3 & \sin\alpha_3 & 0 \\ -\sin\alpha_3 & \cos\alpha_3 & 0 \\ 0 & 0 & 1 \end{bmatrix} \begin{bmatrix} \tau_{\zeta_1} \\ \tau_{\zeta_2} \\ \tau_{\alpha_3} \end{bmatrix}, \tag{69}$$

where the P is the pseudo inverse matrix of the coefficient matrix D that

$$D = \begin{bmatrix} 1 & 0 & \cdots & \cos(\alpha) & \cdots & 1 & 0 \\ 0 & 1 & \cdots & \sin(\alpha) & \cdots & 0 & 1 \\ -y_1 & x_1 & \cdots & -y_j\cos(\alpha) + x_j\sin(\alpha) & \cdots & -y_n & x_n \end{bmatrix}. \tag{70}$$

The pseudo inverse matrix is also called as the generalized inverse matrix since it provides the optimal inverse even beyond the invertible matrix. Even with the remarkable efficiency the present generalized allocation scheme has singularity problem at certain range of instances due to the pseudo inverse matrix, it can be resolved by adding artificial disturbances at the azimuth angle in small amount or defining threshold to activate thrusters.

Assembling the combination of optimal observer and optimal feedback control with the fast single-step generalized allocation scheme, the high accuracy DP system is achieved. Along with the optimum DP control, the accuracy or efficiency can be improved by applying proper feed-forward mechanisms or customized system by more elaborated performance functions.

6. NUMERICAL HYDROELASTIC ANALYSIS OF A SLENDER STRUCTURE

As a case study, the numerical analysis of hydroelasticity is performed for a slender pontoon structure shown in Figure 3. A pontoon with 80 m length, 10 m width, and 5 m draft is adopted. To assure the accuracy of hydrodynamic coefficients even in the short waves, a series of convergence tests is made and total 2900 elements are adopted with the 4^{th} order B-spline method. Mass is 4E+6 kg and moment of inertia is 6.67E+07 kgm^2 for roll, and 2.13E+09 kgm^2 for pitch and yaw. The mass and bending stiffness are assumed to be distributed uniformly along the *x* axis. The center of gravity in the *z* axis is –2 m.

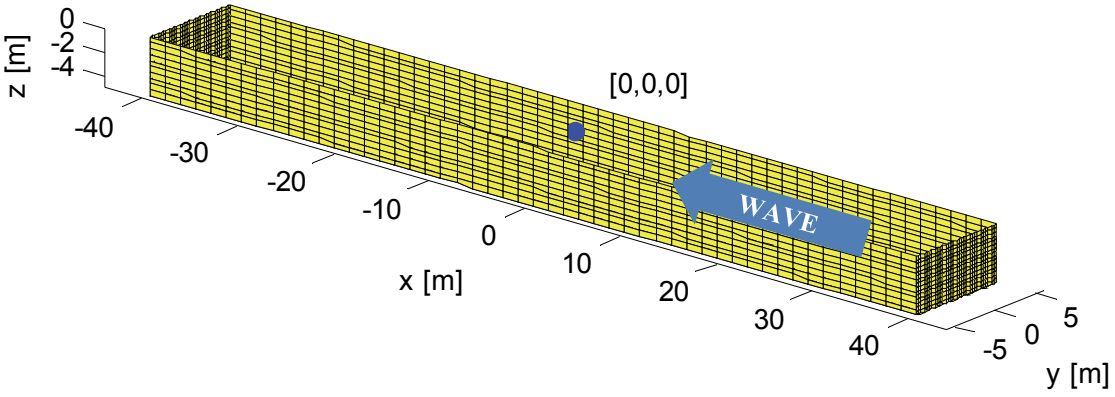

Figure 3. Schematic view of slender pontoon

The comprehensive hydroelasticity based on the developed methodologies is investigated. The hydroelastic dynamic motion responses and stress resultants are achieved for the freely floating condition on both frequency and time domains, and they are cross-checked. Considering the characteristics of the slender type, only shear forces

and bending moments for head sea condition are investigated without the torsional moment in this chapter. Moreover, the extended hydroelastic analysis is performed for the moored pontoon.

For the purpose of in-depth study for the hydroelasticity, a parametric study is carried out in terms of the bending elasticity. Such a slender body has the largest interaction in vertical deflection for the head waves, and thus four different bending stiffness values are applied as summarized in Table 1. The rigid body does not have deflection, and the Quarter *EI* case is the most flexible pontoon.

Table 1. Parametric study for the bending elasticity

Case	Bending Stiffness (*EI*)
1: Rigid body	∞
2: Full *EI* body	2.5601E+10 Nm^2
3: Half *EI* body	1.2801E+10 Nm^2
4: Quarter *EI* body	6.4003E+09 Nm^2

To account for the deflection, the Euler-Bernoulli beam theory is adopted. The mode shape functions are given as Eq. (12). The results from the modal analysis are given in Table 2. The modal resultants present that the lowest elastic modes of the Half and Quarter *EI* cases may undergo resonance due to the wave energy in the high frequency region.

Table 2. Modal resultants of the slender pontoon

Mode	$k_{om,em}$	Modal stiffness [N] / Dry Natural Frequency [rad/sec]		
		Full *EI*	Half *EI*	Quarter *EI*
1	2.365	6.2571E+6 / 2.5014	3.1285E+6 / 1.7688	1.5643E+6 / 1.2507
2	3.927	4.7544E+7 / 6.8952	2.3772E+7 / 4.8757	1.1886E+7 / 3.4476
3	5.498	1.8272E+8 / 13.517	9.1360E+7 / 9.5582	4.5680E+7 / 6.7587
4	7.069	4.9930E+8 / 22.345	2.4965E+8 / 15.800	1.2482E+8 / 11.172
5	8.640	1.1142E+9 / 33.380	5.5710E+8 / 23.603	2.7855E+8 / 16.690
6	10.210	2.1735E+9 / 46.621	1.0868E+9 / 32.967	5.4338E+8 / 23.311
7	11.781	3.8526E+9 / 62.069	1.9263E+9 / 43.890	9.6315E+8 / 31.035
8	13.352	6.3560E+9 / 79.725	3.1780E+9 / 56.374	1.5890E+9 / 39.862

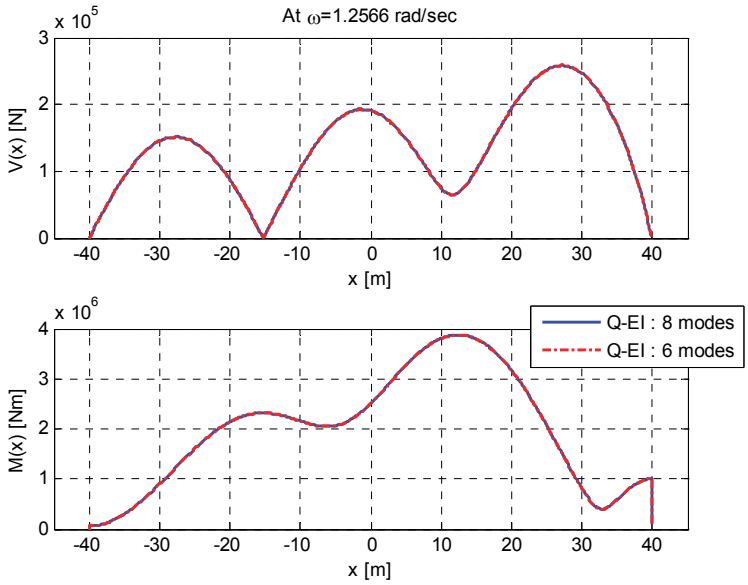

Figure 4. Convergence test of the number of elastic modes (reprinted with permission, Kang and Kim [13])

The number of elastic modes to represent the deflection is determined by convergence test in terms of the elastic mode number. The overall results of the case with 8 elastic modes are compared with those of the case with 6 elastic modes, and they show excellent agreements.

As an example, the total distributions of the shear forces and bending moments are compared at wave frequency 1.2566 rad/sec, as given in Figure 4. For the purpose of the robust analysis with high accuracy, the 8 elastic modes are adopted.

Hydroelastic Dynamic Analysis

To represent the deformation of the slender pontoon, the lowest 8 elastic modes of the Euler-Bernoulli beam theory are used as shown in Figure 5. The pontoon is assumed to be freely floating. The higher number of elastic modes has the higher natural frequency. The hydroelastic dynamic motion responses investigated in both frequency and time domains.

As prerequisite, the verification is made by comparison between two domains. The first two elastic modes are demonstrated in Figure 6. The spectral RAOs from the time domain analysis are well coincided with those frequency domain RAOs. In both domains, the resonance phenomena are well captured at the first elastic modes of the Quarter and Half *EI* cases.

Frequency Domain

The 16 modes for the deformable slender pontoon including the 8 elastic modes are compared with the different *EI* cases in Figure 7 for rigid modes and in Figure 8 for

elastic modes. The four cases including the rigid are compared in the 6 rigid modes and three elastic cases are compared in the 8 elastic modes along with the incident wave frequency. Considering the main wave energy from 0.3 to 1.6 rad/sec, 20 frequencies are applied from 0.01 rad/sec to 2.1 rad/sec.

Since the head sea is applied, the surge, heave and pitch motions are dominant in this case. The 6 rigid modes are almost same among the four different bending elastic cases, which represent that the elastic modes do not affect the rigid modes significantly.

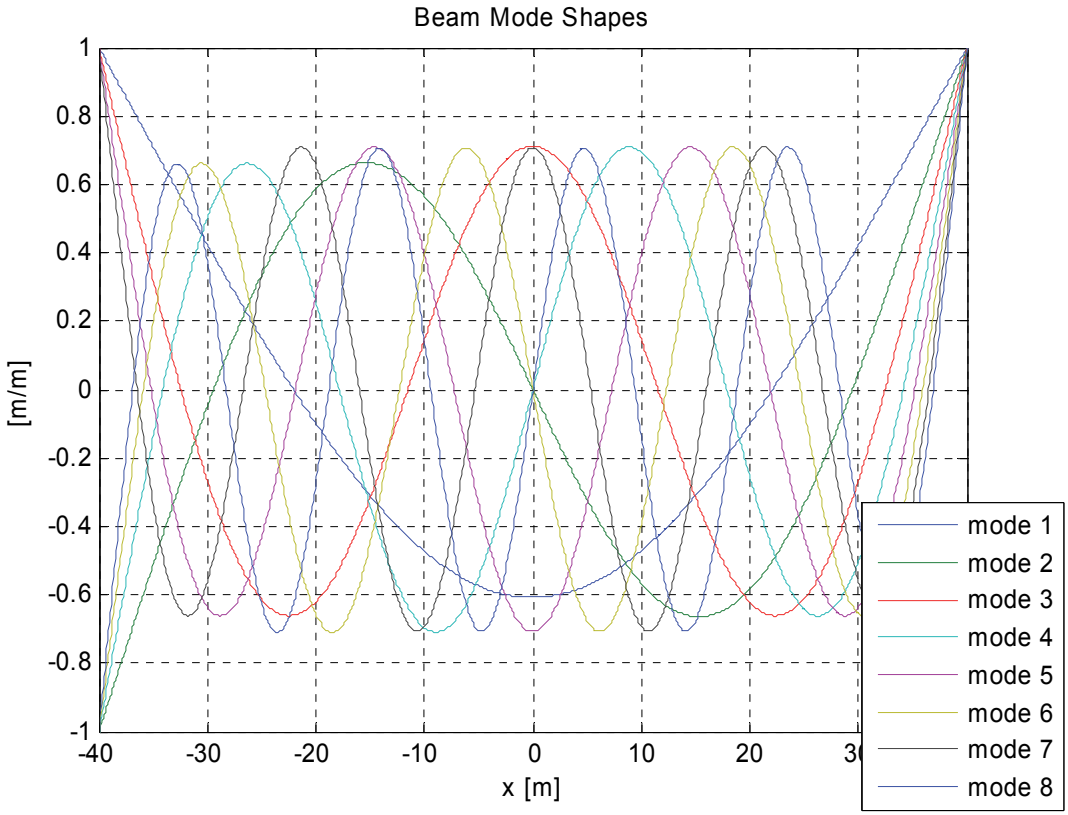

Figure 5. Mode shapes from Euler-Bernoulli beam theory

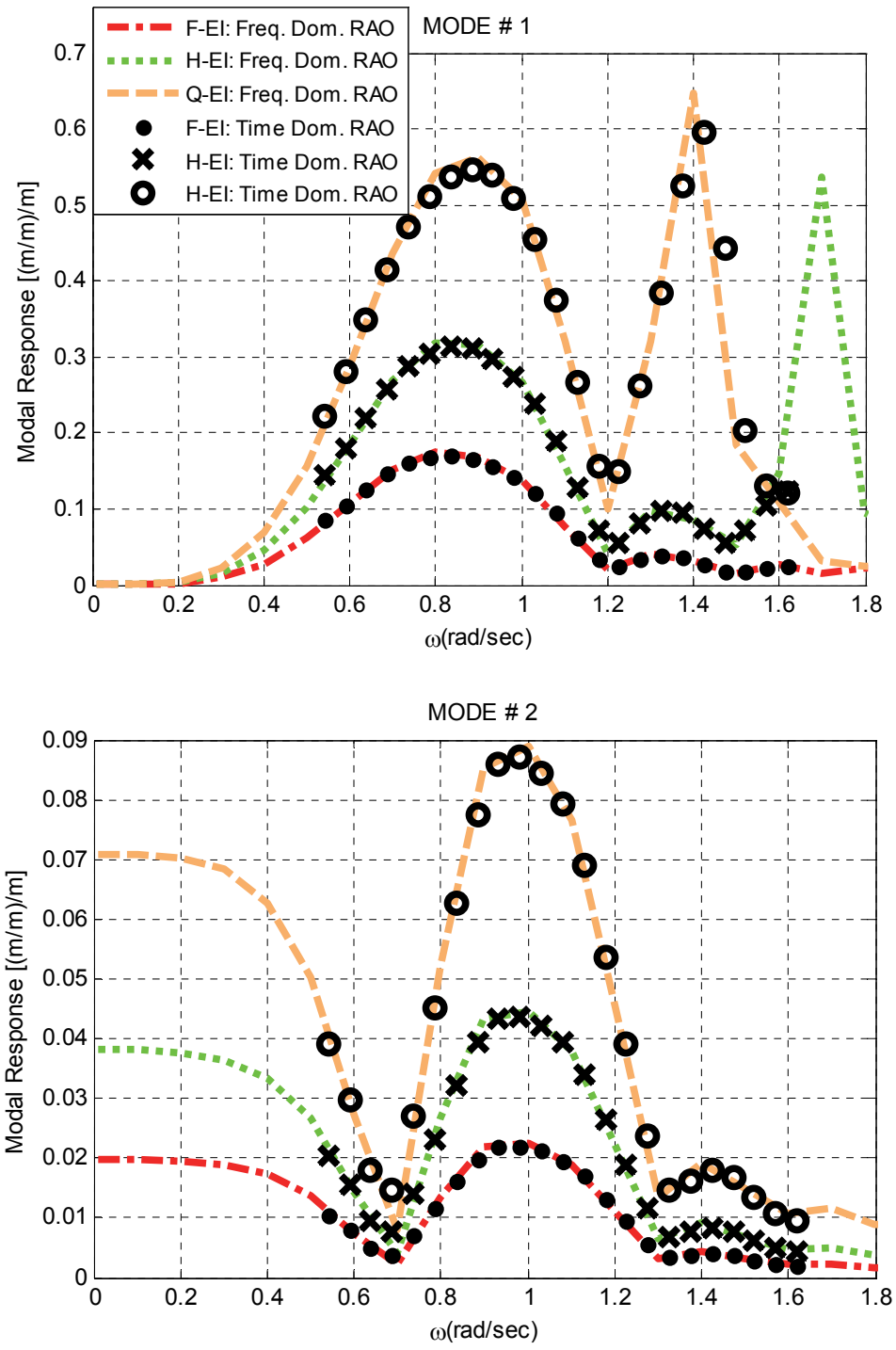

Figure 6. Verification of hydroelastic dynamic analysis for slender pontoon

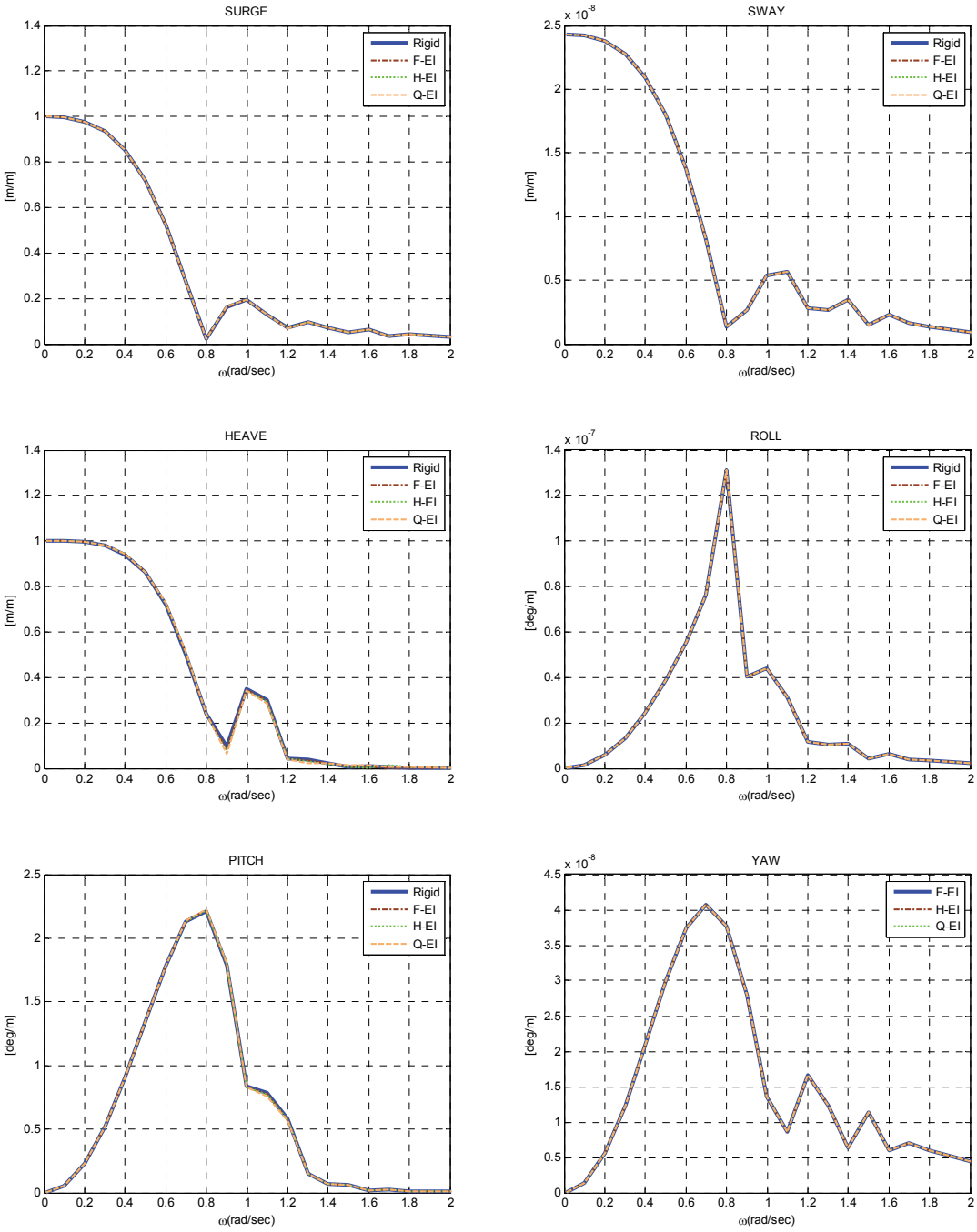

Figure 7. Hydroelastic dynamic motion for rigid mode responses on frequency domain for slender body

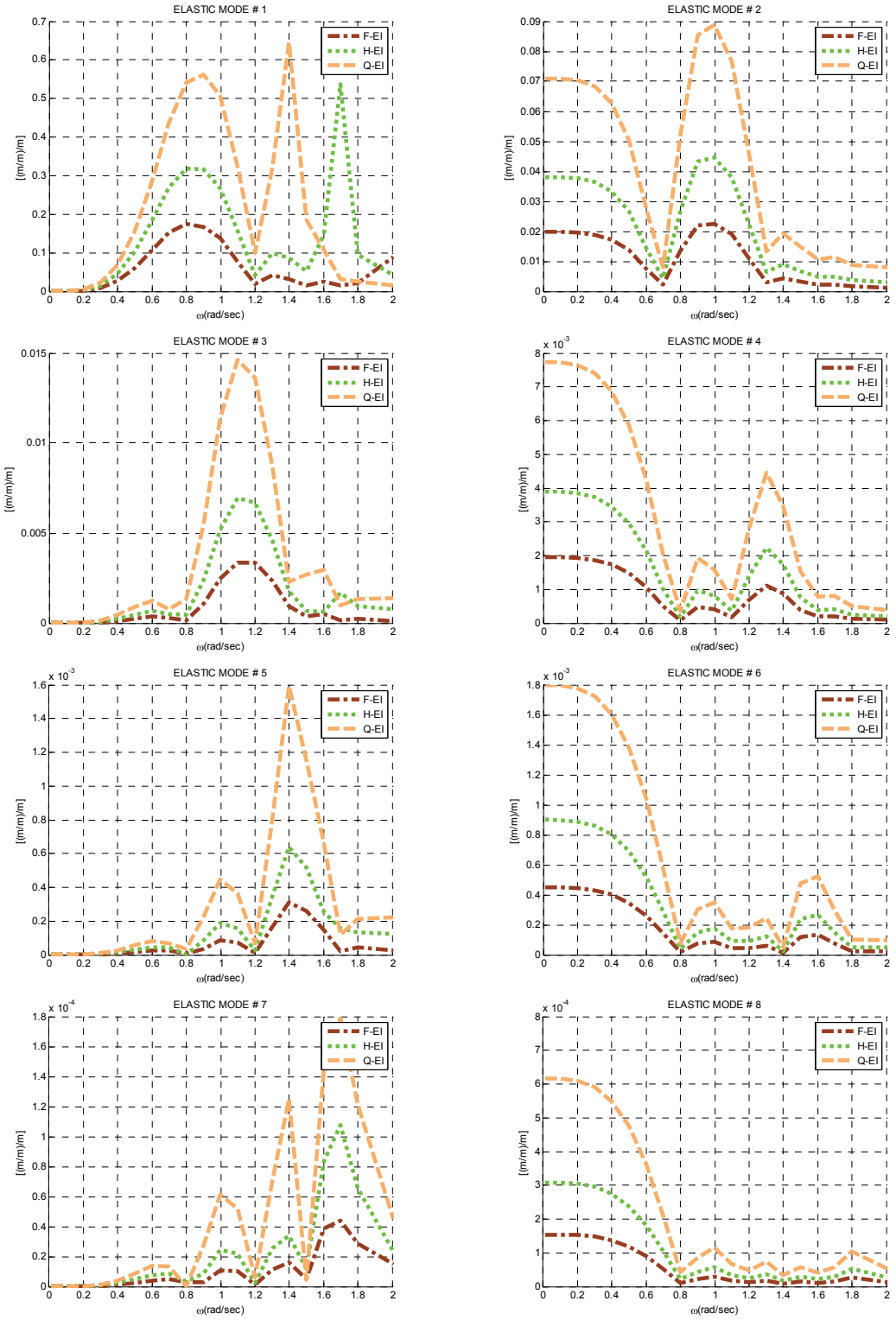

Figure 8. Hydroelastic dynamic motion for elastic mode responses on frequency domain for slender body

However, it does not mean the dynamic motion responses are identical. In the three elastic pontoon cases have additional elastic motion responses and thus the local responses will be different from the rigid case.

Moreover, the three flexible cases have deformations dependent on the natural frequencies of the elastic modes. The lowest elastic modes of the Quarter and Half *EI* cases have resonance peaks at 1.4 and 1.7 rad/sec, respectively. The high frequency energy of waves from the 2nd order sum-frequencies as well as the linear order frequency will excite those elastic modes and induce the resonances.

Overall, the odd number elastic modes have similar tendency of RAO, while the even number modes have their similarity of RAO. Therefore, the first or second elastic modes may excite the rest of odd number or even number elastic modes, respectively.

Numerical Hammer Test

With the diagonal modal inertia and stiffness values, the added inertia and hydrostatic stiffness terms are induced by the wet condition of the floating deformable body. The terms influence the virtual inertia and stiffness at respective elastic modes and create coupling effects among the rigid and elastic modes. Therefore, the wet natural frequency as the real resonance frequency needs to be identified over the dry natural frequency.

Based on the time-domain hydroelastic dynamic analysis, the numerical hammer test is conceived. The wave or any other environmental loads are assumed to be zero and an initial impact at a certain position is applied to the slender pontoon. Once the impact removed, the decaying vibrations are generated under the influences of the radiation

potential-induced hydrodynamic pressures and hydrostatic pressures. The hydrodynamic pressures consist of the infinite-frequency added inertia loads proportional to the accelerations of the deformable body and radiation damping convolution loads as functions of the velocities. Those pressures are placed in the left hand side of the whole system of motion equations as inertia, stiffness, and damping terms, and no further excitations are applied on the right hand side after the initial impact. Therefore, the series of frequencies calculated from the decaying vibrations can be interpreted as the realistic wet natural frequencies under the modal expansion method assumption.

In this study, the impact 1.5E+8 N is applied at the right top corner (40 m, 5 m, 5 m) of the slender pontoon and the free vibrations are measured at the left down corner (-40 m, -5 m, 5 m) as shown in Figure 9.

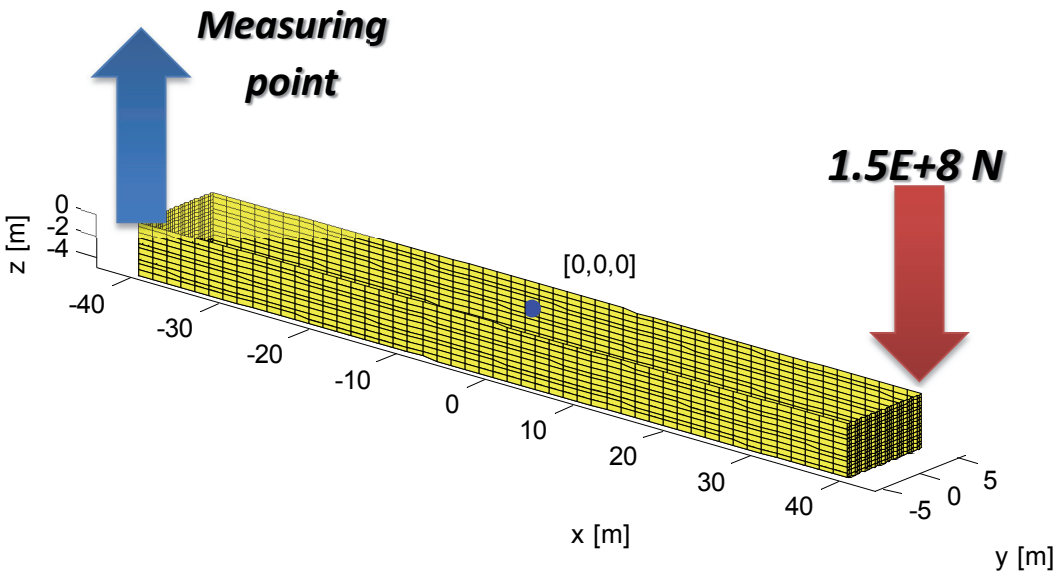

Figure 9. Numerical hammer test of the slender pontoon

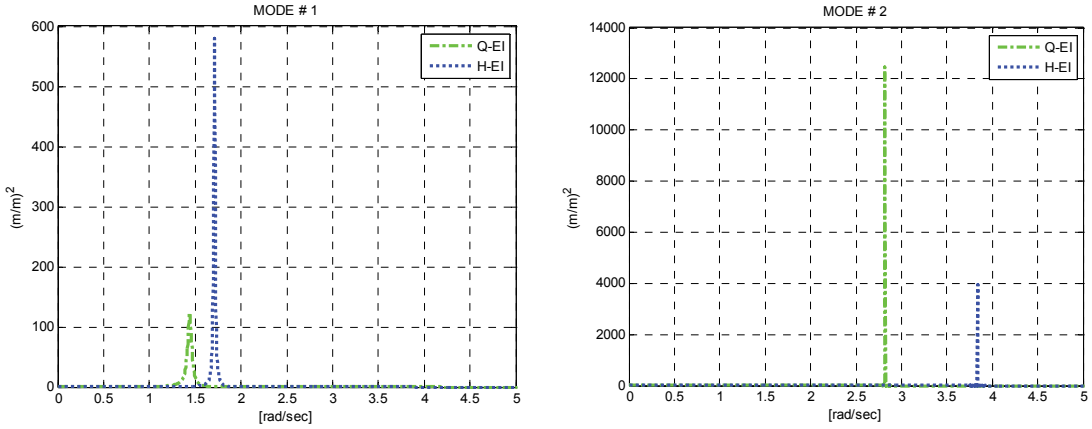

Figure 10. Response spectra after the hammer test

To clarify the resonance occurrence, the free vibrations of the first 2 elastic modes are investigated for the Quarter and Half *EI* cases as Figure 10. The real wet natural frequencies including the water contact condition and coupling effects among the modes are summarized in Table 3.

Table 3. Numerical hammer test of the slender pontoon

Elastic mode	Quarter *EI*	Half *EI*
1	1.44 rad/sec	1.71 rad/sec
2	2.82 rad/sec	3.84 rad/sec

The first elastic mode of the Quarter *EI* case is increased mainly due to the increased buoyancy-related stiffness for the first elastic mode as 1.961E+6 N, which is about 1.3 times larger than the dry modal stiffness. In the meantime, other three natural frequencies are decreased due to relatively dominant modal stiffness. It represents that

the wet natural frequency is dependent on not only the added modal inertia but also hydrostatic modal stiffness so that either decrease or increase of the natural frequency can happen.

Time Domain

The time domain hydroelastic dynamic analysis is carried out for a set of random sea waves given in Figure 11.

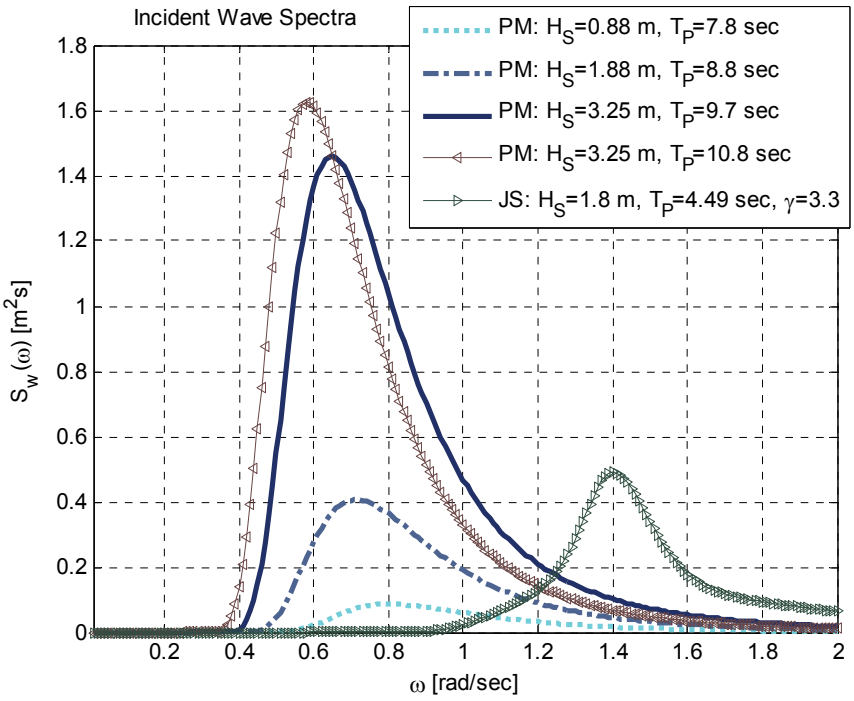

Figure 11. A set of random seas

To investigate the dynamic responses along with the severity of the sea states, sea state 3, 4, and 5 are applied by the significant wave height (H_S) 0.88, 1.88, and 3.25

m with the peak period (T_P) 7.8, 8.8, and 9.7 sec of the Pierson-Moskowitz spectrum, respectively. To study the resonance effects, the Korean south offshore condition is applied by H_S=1.88 m, T_P=4.49 sec, and γ=3.3 of the JONSWAP spectrum. Moreover, sea state 5* is implemented for the purpose of the hydroelastic structural analysis, which will be discussed in the next section.

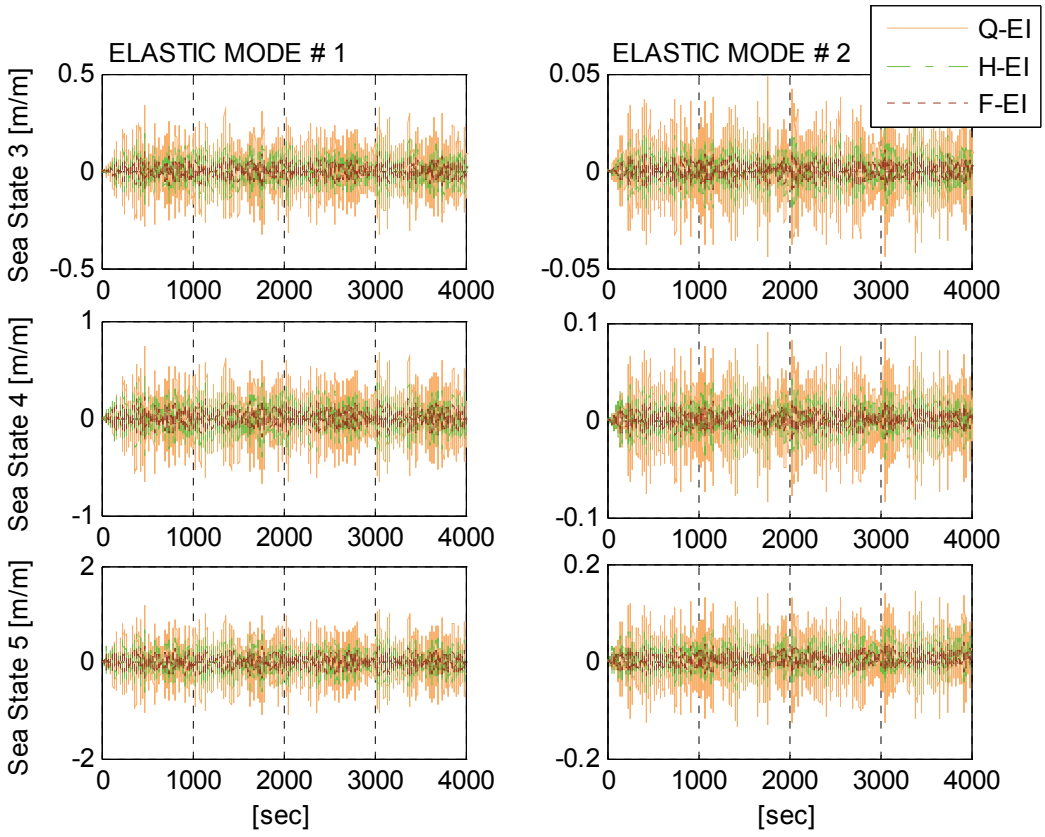

Figure 12. Amplified responses by the severer sea state

Considering negligible differences of the 6 rigid modes among the four cases, the first two elastic modes are first investigated for the three sea states in Figure 12. The

responses are proportional to the severity of the sea states and there exists no significant amplification due to the resonance. It is mainly because of the low wave energy around the natural frequencies of the elastic modes. The second elastic modes in general have 10 % scale of the first elastic modes. With respect to the bending elasticity, the more flexible body has straightforward increment in responses.

To clarify the resonance phenomena, the first elastic modes for the three flexible cases are compared in terms of response spectra in Figure 13. It is shown that the dominant responses are placed at 0.5 to 1.2 rad/sec by the main wave energy and the resonances induce minor peaks at 1.4 and 1.7 rad/sec, respectively.

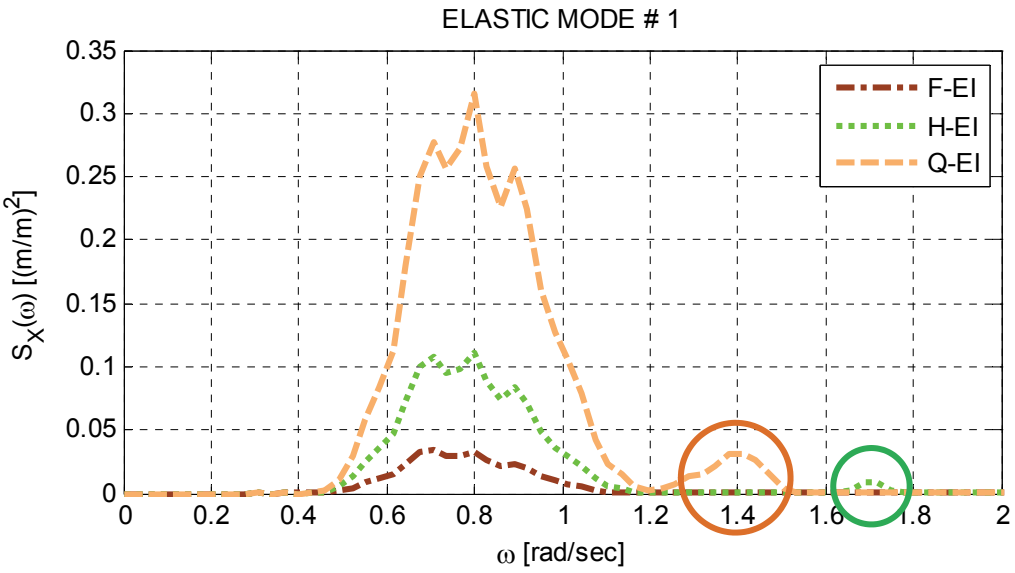

Figure 13. Response spectra of the first elastic modes

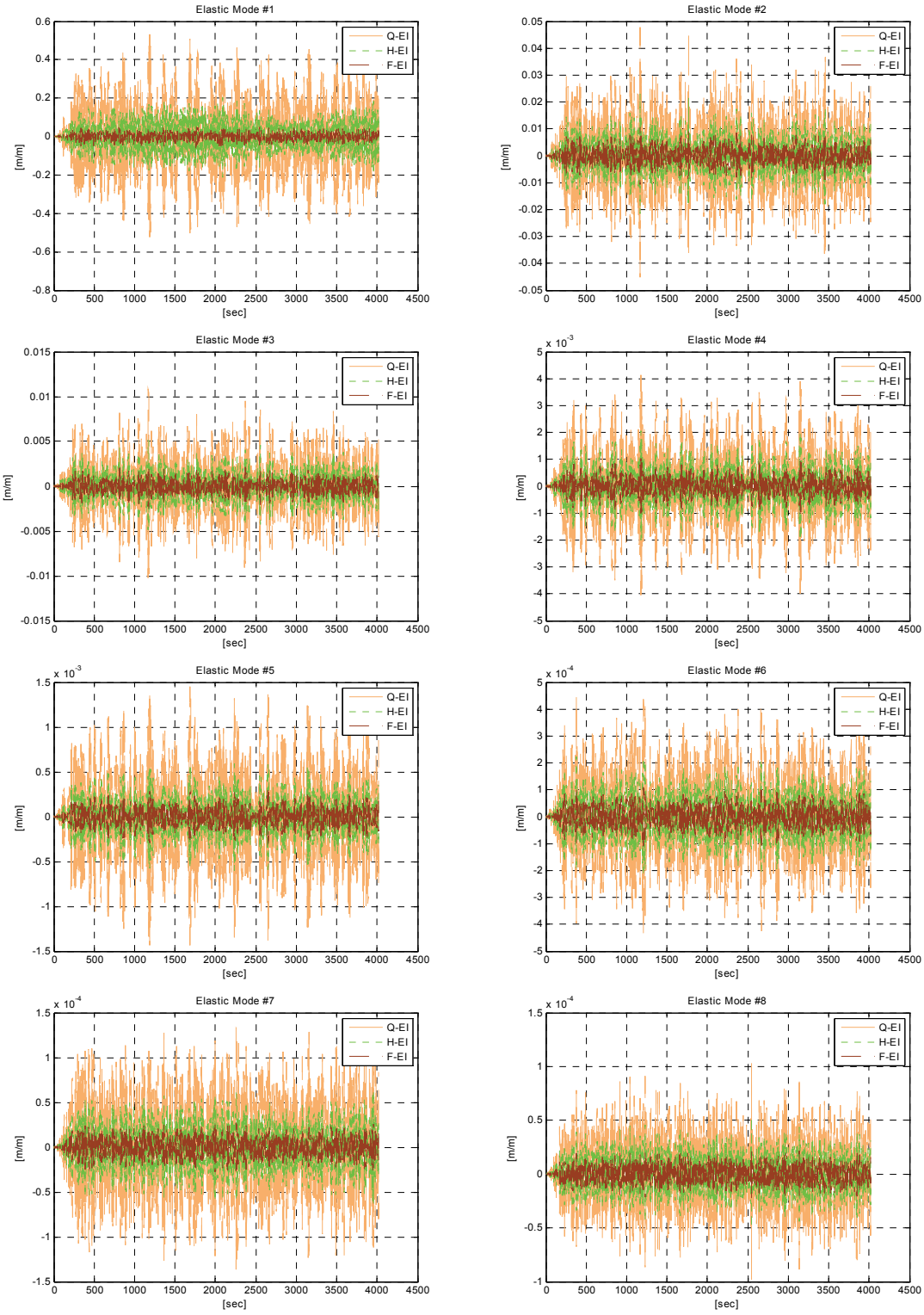

Figure 14. Resonated deformation of slender pontoon

To study a case with resonance enhanced, the JONSWAP spectrum for the Korean south offshore are applied. The low peak period of the JONSWAP mainly resonates with the first elastic modes of the Quarter and Half *EI* cases. The 6 rigid mode responses are absent due to the negligible differences among the four cases. Therefore, only three flexible cases are compared for the elastic modes in Figure 14.

In the relative scale of amplitudes, the first elastic modes show clear amplification by the resonance as compared in Figure 15. The Quarter and Half *EI* case have notably large amplitude than the Full *EI* case especially at the lowest elastic modes. The resonances are given as peaks in the response spectra of the first elastic mode.

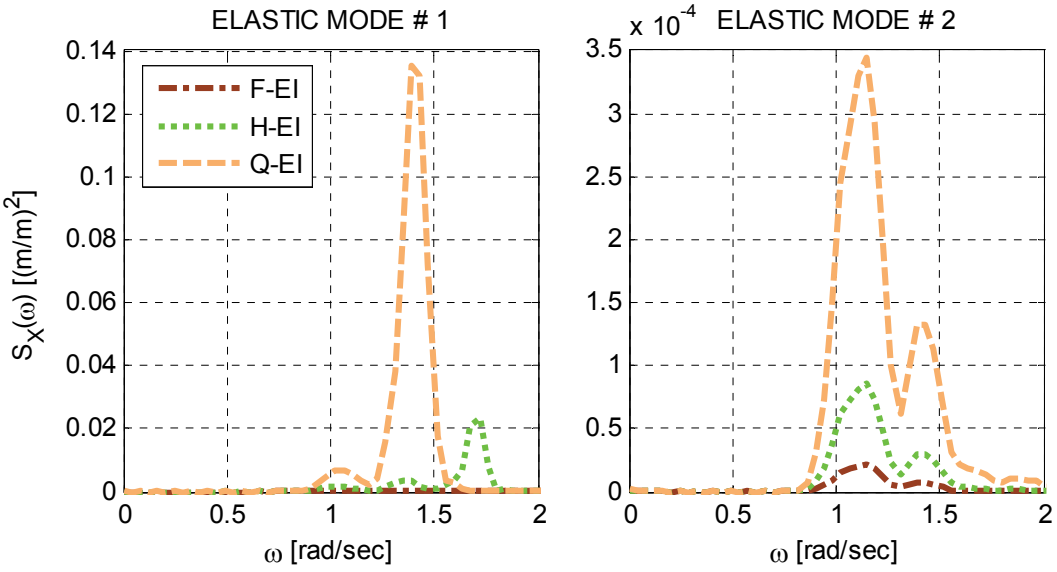

Figure 15. Resonated response spectra by JONSWAP spectrum

The hydroelastic dynamic analysis represents that the elastic modes may undergo resonance phenomena due to the wave energy in the high frequency region and have

strong coupling among the modes, while the 6 rigid modes could be invariant with the deformation. The dynamic elastic modes would important for the local vibration and overall deformation of the floating body.

Simplified 2nd Order Time Domain Analysis

Furthermore, the complete second order wave loads for the rigid modes are included in the time domain hydroelastic dynamic analysis for the slender pontoon by the two-term Volterra series. As an example, the JONSWAP spectrum with Hs=5 m, Tp=10.6 sec, and Gamma=1.6 is used

In comparison of the first elastic modes for the Half and Quarter *EI* cases, the simplified second order analysis clearly shows the enhanced resonance of two elastic modes mainly due to the rigid-assumed second order wave loads as shown in Figure 16.

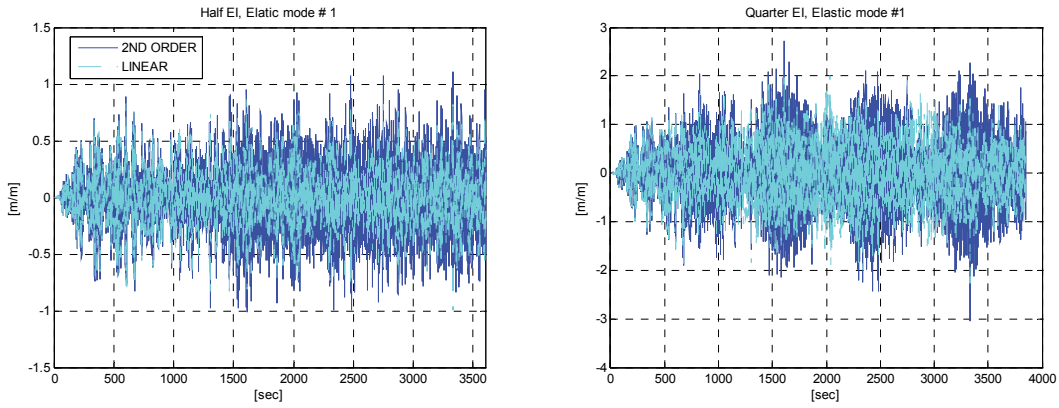

Figure 16. Time series of resonated elastic modes due to 2nd order wave loads for slender pontoon (reprinted with permission, Kang and Kim [14])

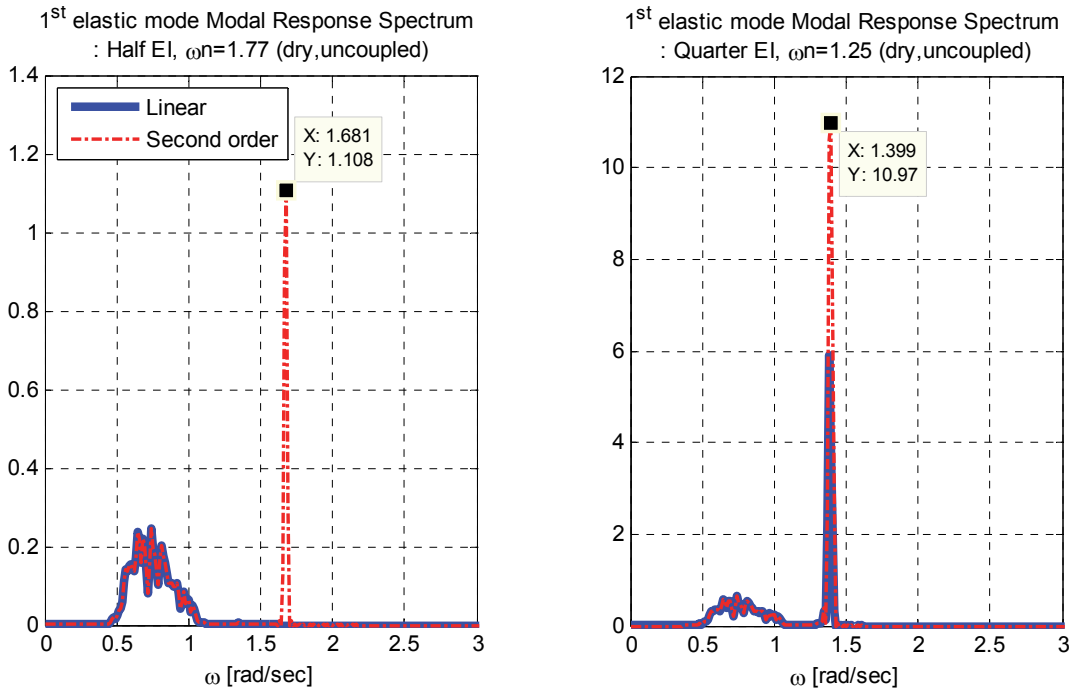

Figure 17. Response spectra of resonated elastic modes due to 2nd order wave loads for slender pontoon (reprinted with permission, Kang and Kim [14])

The response spectra represent that the first elastic mode of the Half *EI* case resonates with the sum- frequency loads at 1.681 rad/sec in Figure 17, and the Quarter *EI* case has the first elastic mode signified by the sum-frequency loads.

It turns out that the simplified method is good to capture the resonance in the high frequency region, but the complete 2nd order hydroelastic analysis needs to be developed for more accurate estimation in scale.

Hydroelastic Structural Analysis

Once the dynamic motion responses known, all the loads acting on the deformable floating body are available and the stress resultants are achievable. The slender pontoon is investigated in terms of shear forces and bending moments with the

torsional moments ignored. The shape of the floating body and head sea condition impose insignificant stress resultants. The frequency domain analysis provides full distributions of the stress resultants at each incident wave frequency with respect to the x axis and the time domain analysis achieve the irregular stress resultants induced by the random sea as functions of time and space.

As the prerequisite verification, the stress resultants between two domains are compared in terms of the stress resultants RAO. The irregular shear forces and bending moments induced by the random sea are measured at the quarter section and mid-section, respectively, and converted as spectral stress resultant RAO by the Fourier Transform. The severest sea state, sea state 5, is adopted for robust verification. The comparisons show successful agreements between the frequency and time domains and the resonance phenomena are well captured in both domains as demonstrated in Figure 18.

Beyond the total stress resultants, the componential stress resultants are also compared to identify the phase differences among the components and they also show excellent correspondence in Figure 19. For the purpose of demonstration, the bending moments are compared in terms of respective components.

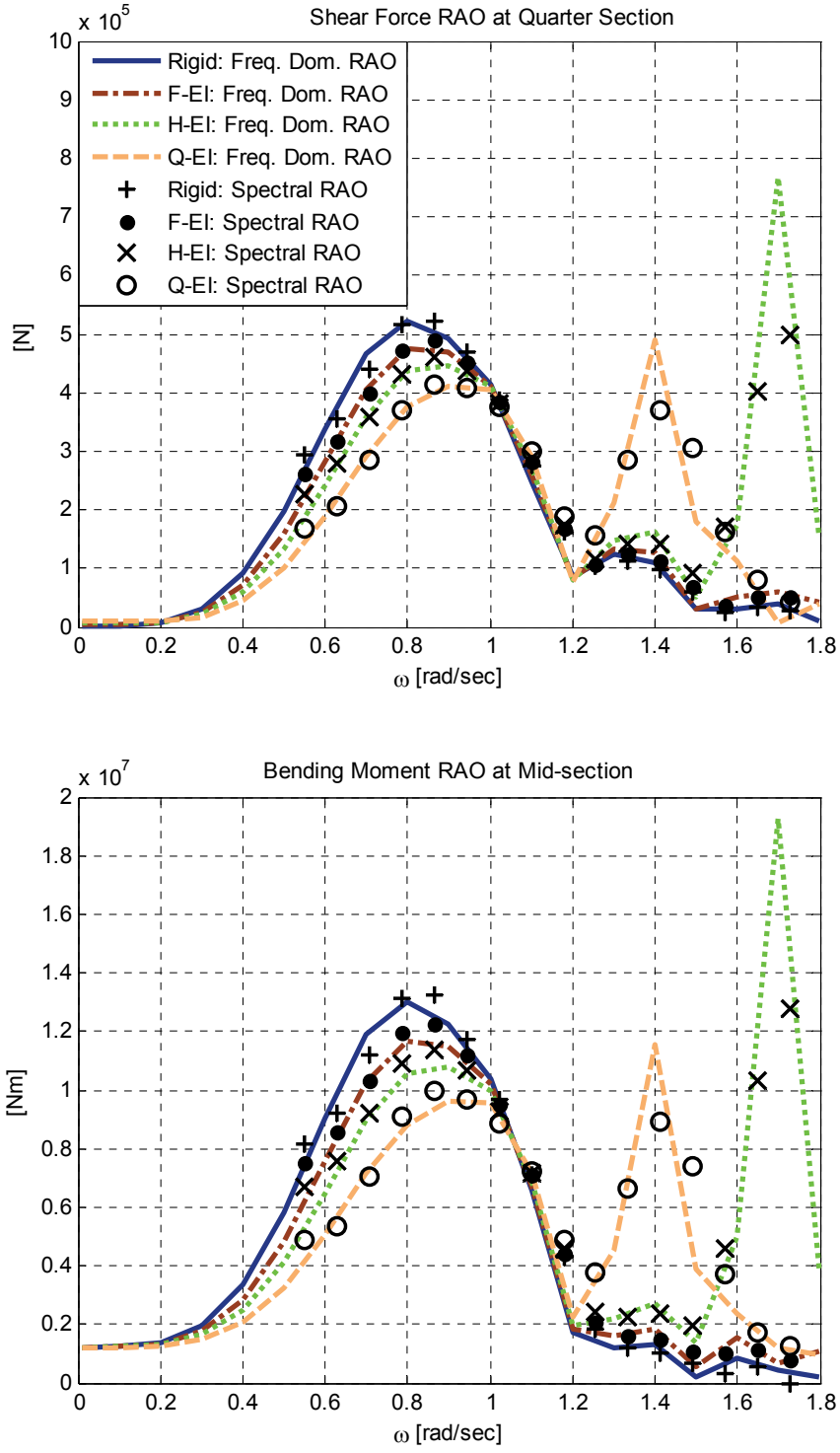

Figure 18. Verification of the hydroelastic structural analysis for slender pontoon

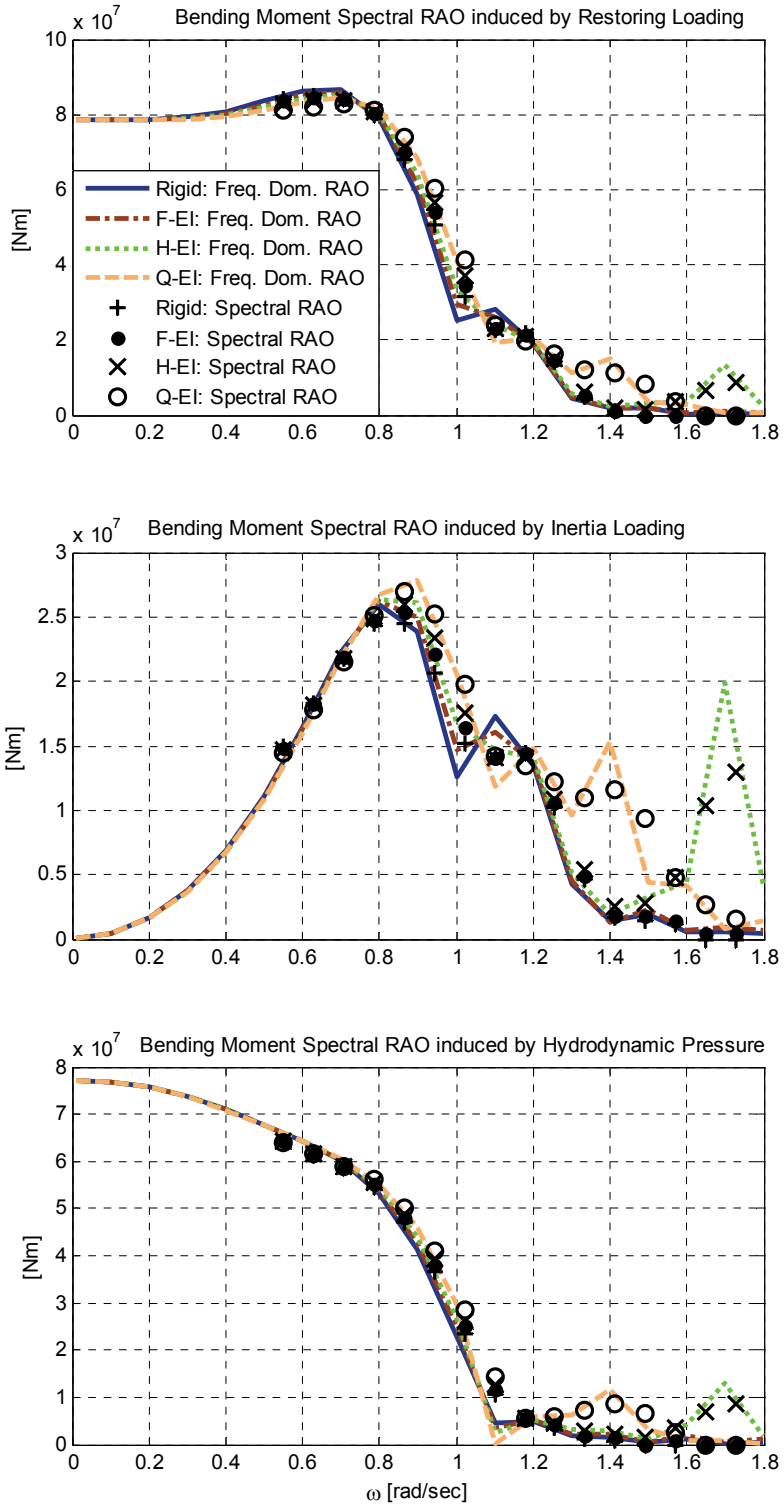

Figure 19. Componential verification of hydroelastic structural analysis for slender pontoon

Frequency Domain

As an additional verification of the frequency domain hydroelastic structural analysis, the stress resultants at 0.453 rad/sec are compared against results from an independent numerical analysis based on the plate theory by Kim et al [20] in Figure 20.

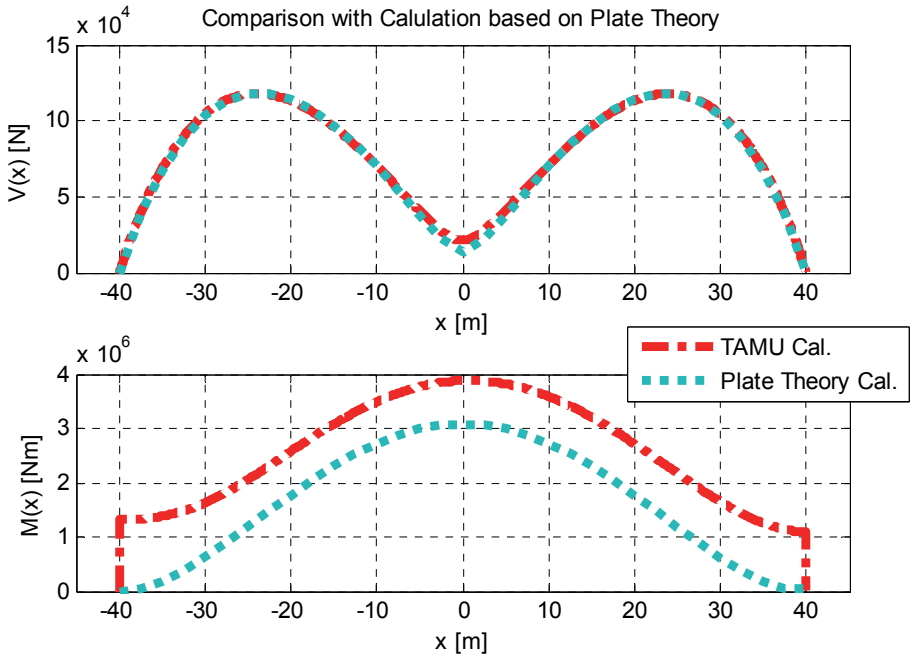

Figure 20. Verification of the frequency domain hydroelastic structural analysis (reprinted with permission, Kang and Kim [13])

In the comparison, the shear forces show excellent agreement and the bending moments have shifted upward as much as horizontal pressure effects at the side walls with well-matched tendency. The correspondences prove the validity of the hydroelastic structural analysis. Moreover, the difference in the bending moments represents the advantage of the present method such that the side wall effects, which are normally

ignored in the plate theory method, are significant in the bending moments especially for the low frequency waves.

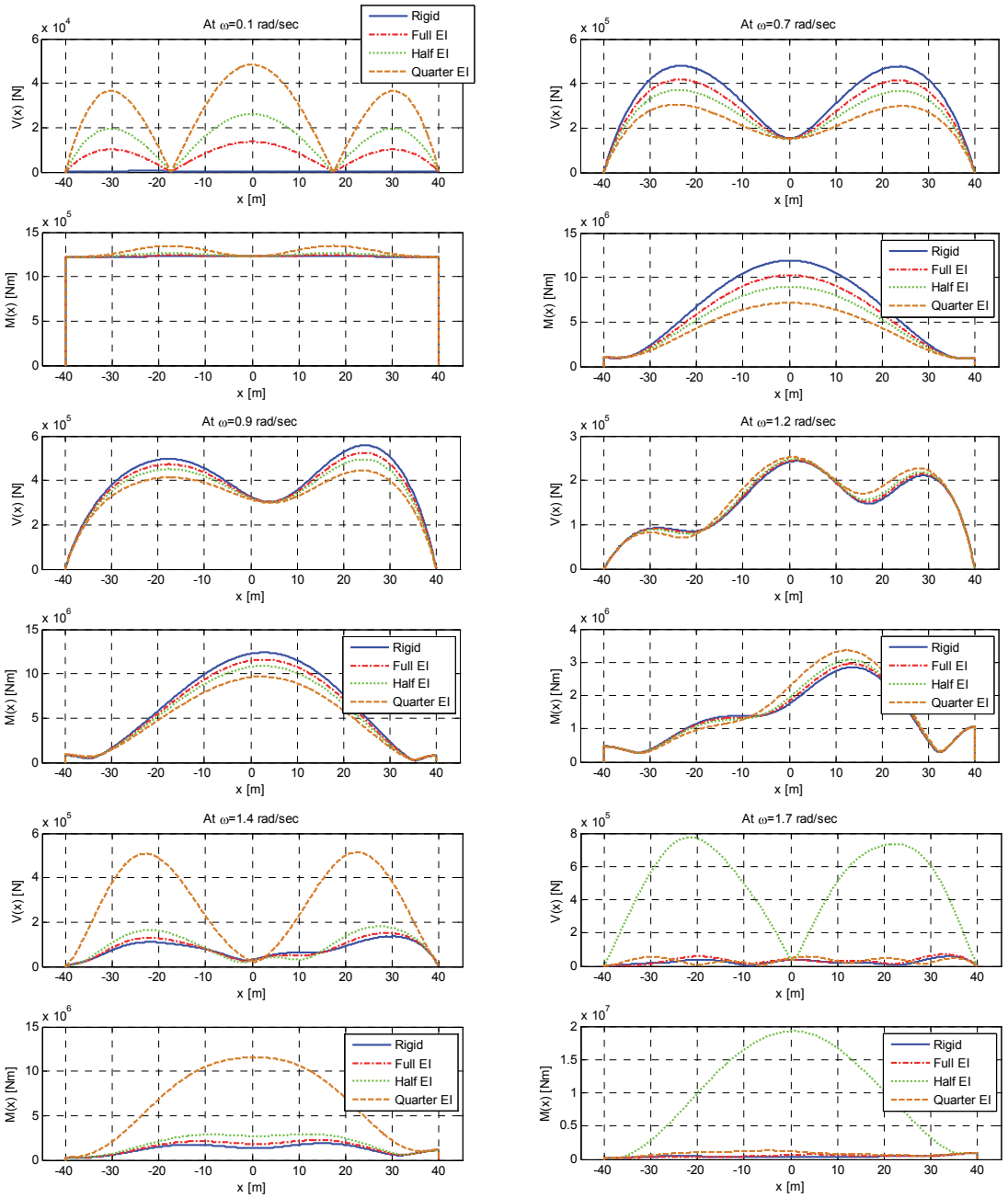

Figure 21. Results of the frequency-domain hydroelastic structural analysis for the slender pontoon (reprinted with permission, Kang and Kim [13])

The stress resultants for the slender pontoon on the frequency domain are given in Figure 21.Among the 20 discrete incident wave frequencies from 0.01 to 2.1 rad/sec, 6 frequencies are demonstrated, which are representative of each group categorized by the distribution shape. The long waves up to the frequency 0.3 rad/sec, which are longer than of the barge length, the bending moments, have overwhelming components from the side wall effects, which the shear forces are proportional to the flexibility. In the moderately long waves from 0.3 to 0.8 rad/sec wave frequency, the stress resultants are symmetric with respect to the body origin and thus the maxima of shear forces bending moments occur at the quarter section and mid-section, respectively. In addition, the less flexible body has the larger bending moment. The higher frequencies from 0.8 to 1.3 rad/s imply the less dependency on the hull flexibility and the distribution shape becomes more asymmetric. In the frequencies over 1.2 rad/sec, the more flexible body has the larger maximum stress resultants. Near the natural frequency of the respective lowest elastic modes, the resonances induce the overwhelming stress resultants.

Collecting the maximum stress resultants, it is seen that the slender pontoon is vulnerable at the frequency region from 0.4 to 1.1 rad/sec and natural frequencies from Figure 22. In the intermediate region, the more flexible body generates the less stress resultants. Therefore, if the hell elasticity is ignored, the overall stress resultants may get overestimated in that frequency range. In addition, the neglected resonance of the elastic modes will induce the significant underestimates of stress resultants.

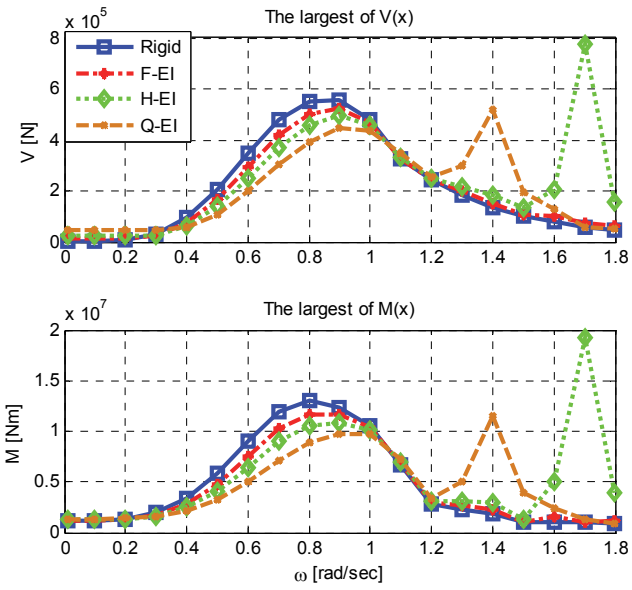

Figure 22. Maxima of the stress resultants for the slender pontoon (reprinted with permission, Kang and Kim [13])

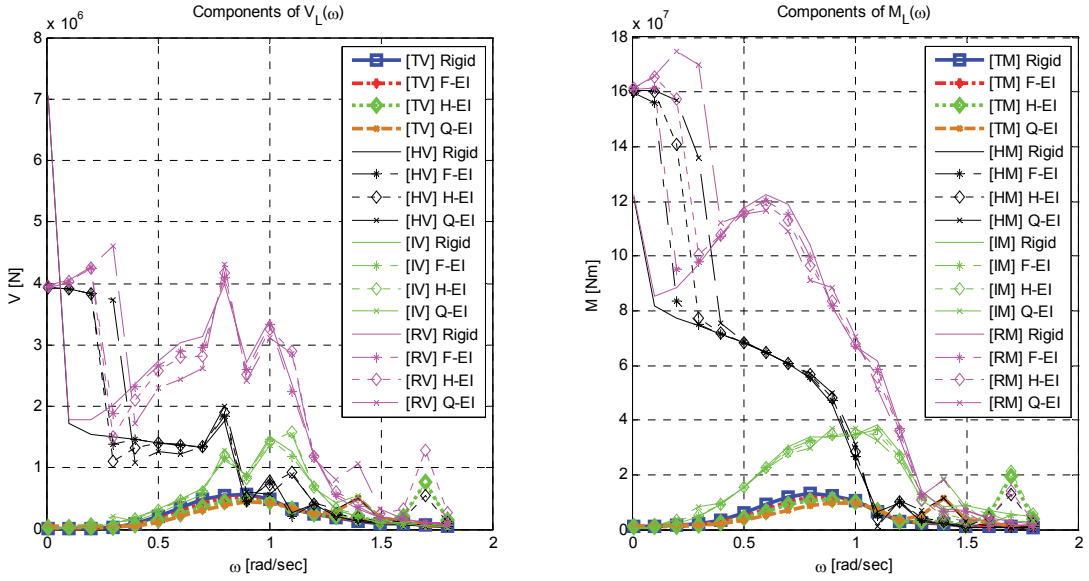

Figure 23. Componential comparison of maximum stress resultants (reprinted with permission, Kang and Kim [13])

To identify the relative importance of the respective components, the componential comparison of the maximum stress resultants are plotted. In Figure 23, H stands for the hydrodynamic pressures-induced stress resultants, I and R stands for the inertial and restoring-induced stress resultants, respective. T means the total stress resultants. In general, the restoring and hydrodynamic pressure components are dominant. The tendency may vary with different mass and elasticity distributions.

Time Domain

After the verification given in Figure 18 and Figure 19, the stress resultants induced by the random seas are investigated. First, the shear forces at the quarter section and bending moments at the mid-section are compared among the four cases with the 3 sea states in Figure 24.

Along with the severity of the sea state, the stress resultants tend to get doubled from the previous sea state. Although there exist no significant differences among the four different full flexibilities, the Quarter *EI* case in general has the least stress resultants. The developed hydroelastic structural analysis enables to achieve the stress resultants from the rigid floating body. It is useful to calculate the stresses on the conventional floating body in the random seas with the rigid body assumption, which is infeasible in the deflection-based structural analysis.

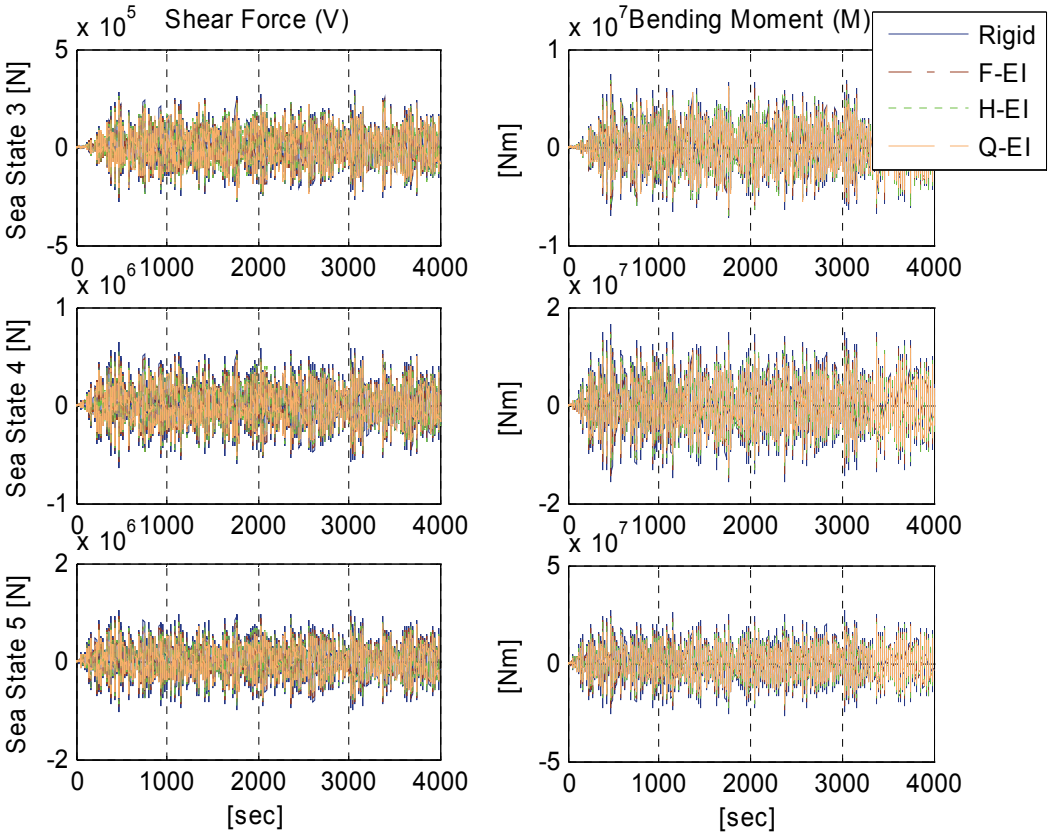

Figure 24. Variations of the stress resultants for severer sea states

The resonance effects to the stress resultants are investigated by the hydroelastic structural analysis for the JONSWAP spectrum. In Figure 25, all the four cases are compared.

Without the resonance the Full *EI* case has almost identical shear forces and bending moments, whereas the Quarter and Half *EI* cases clearly show the amplified stress resultants in Figure 25. The closer peak energy to the natural frequency induces the larger shear forces and bending moments. Comparing them with the sea state 4 results, the sea state 4 have large amplitudes and it is consistent with the tendency of the

stress resultants RAO such that the moderate frequency range has RAO dominantly wider than the natural frequency zone.

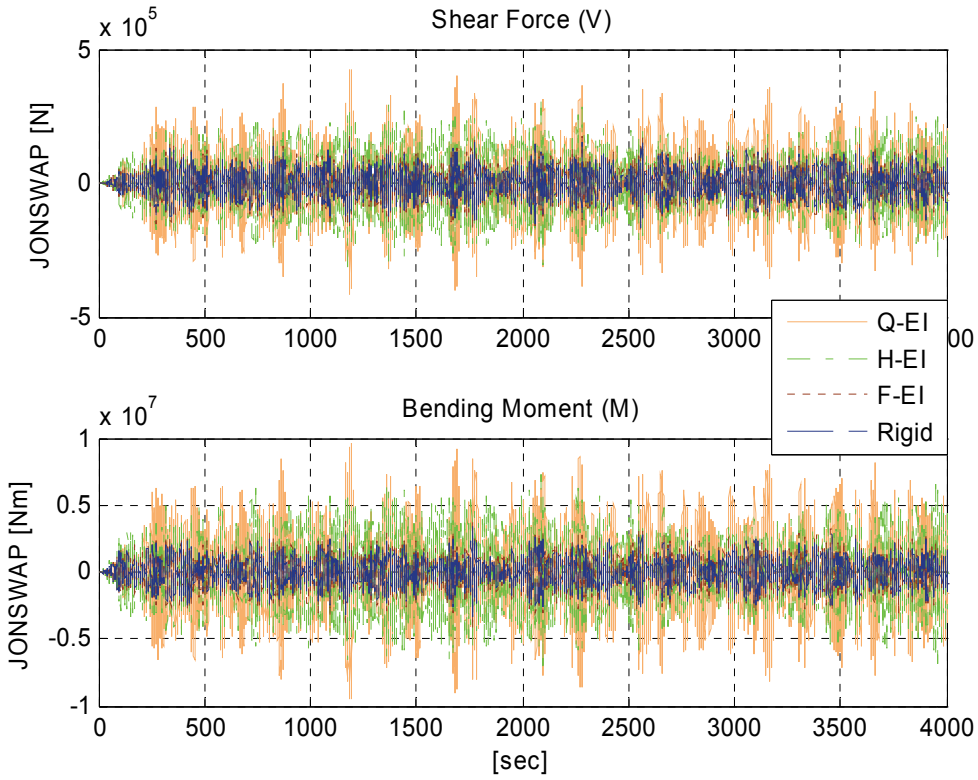

Figure 25. Resonated stress resultants of slender pontoon

Subsequently, a couple of advantages of the developed hydroelastic structural analysis are herein discussed. As pointed out earlier, the time-domain hydroelastic structural analysis includes the side wall effects and convolution term effects.

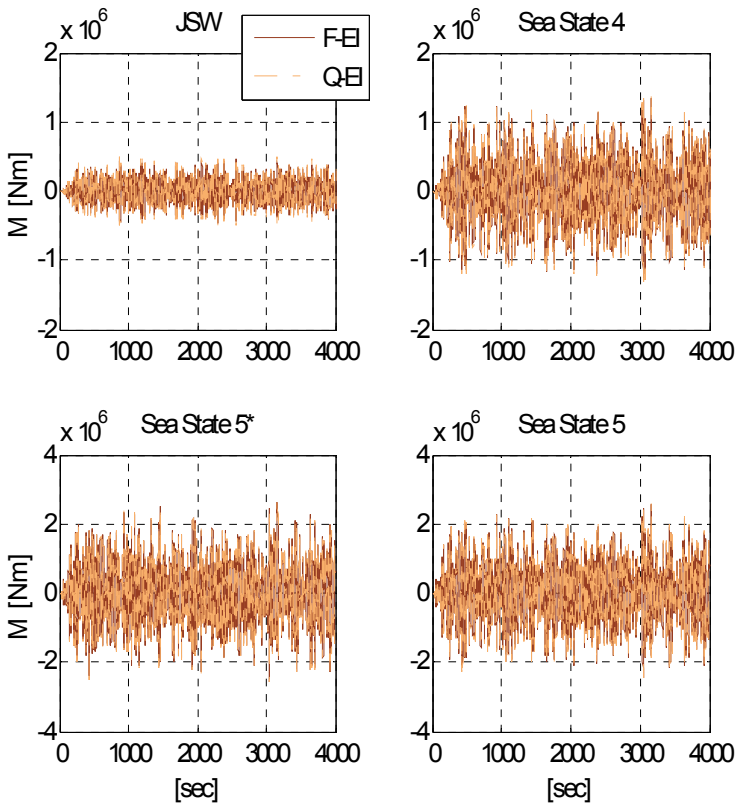

Figure 26. Bending moments purely induced by the side wall effects

In comparison of the bending moments between the JONSWAP and the sea state 4 or the sea state 5* and sea state 5 in Figure 26, the bending moments induced by the side wall effects are increased by more energy in the low frequency region. The JONSWAP with the peak frequency at about 1.4 rad/sec induces about 1/3 bending moments than the sea state 4 at the side wall. The small shift of the peak period at the sea state 5* generates corresponding small increases as 5 ~7 % of the sea state 5. Overall, the side-wall induced bending moments are about 10 % of the total bending moments.

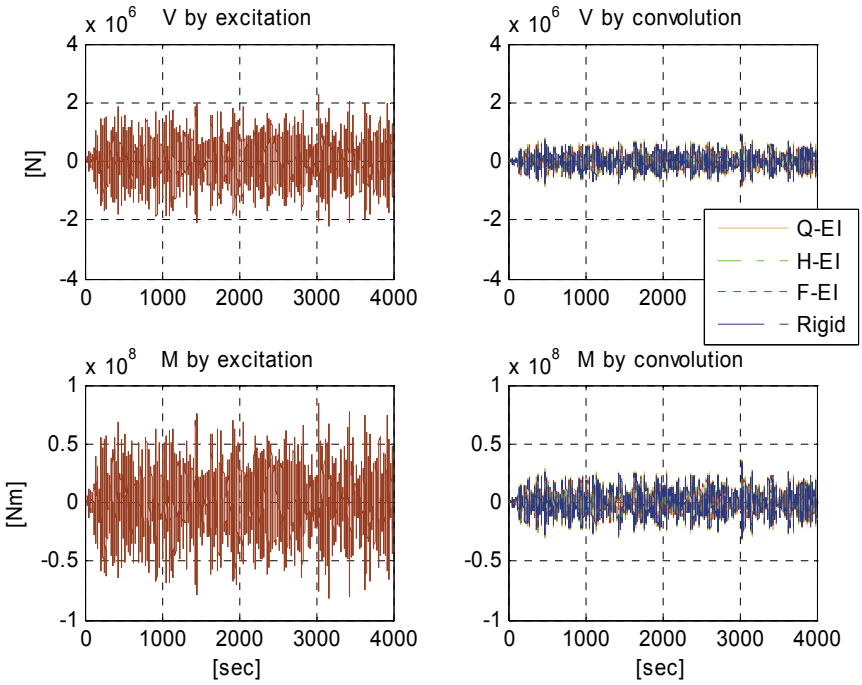

Figure 27. Stress resultants induced by the convolution terms

In simplified hydroelastic analyses, the convolution integral terms are neglected due to the numerical difficulties. To clarify its relative importance, the contribution of the impulse-related convolution term is compared with wave excitation contribution in the sea state 5 as shown in Figure 27. The stress resultants induced by the convolution term reaches about 30 ~ 40 % of the wave excitation contributions and it is about 10 % of the total stress resultants.

Therefore, the simplified hydroelastic structural analysis in the time domain may impose errors over 10 % of the stress resultants, and the developed hydroelastic structural analysis is applicable to various applications with higher accuracy.

Hydroelastic Analysis Coupled with Mooring-Riser

The slender elastic pontoon is moored by 4 vertical taut mooring lines at the corners as shown in Figure 28. The flexibility of the pontoon is assumed as the Quarter *EI* case and the taut mooring lines are modeled as polyester ropes. The water depth is assumed as 125 m. To generate the random seas, the sea state 5 is applied without the second order wave loading. The particulars of the mooring lines are given in Table 4.

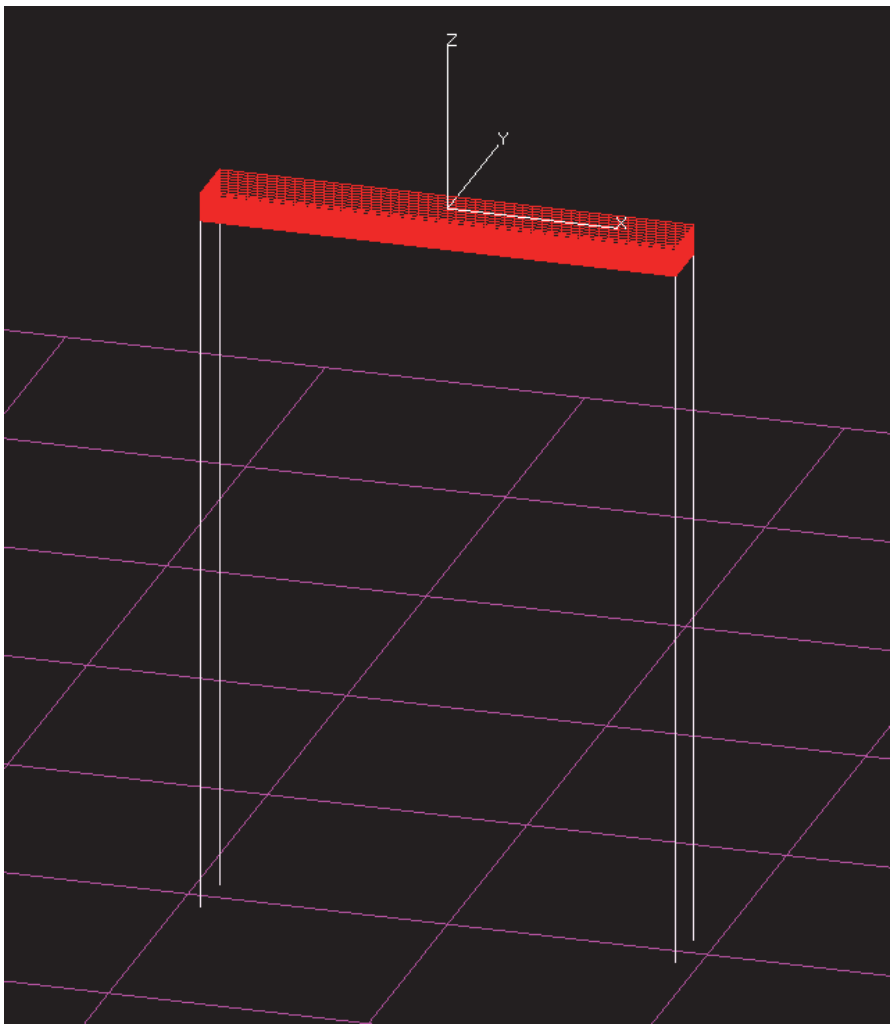

Figure 28. Schematic view of the moored slender pontoon

Table 4. Particulars of mooring lines

Line length	120 m
Wet weight, Dry weight	24.79, 29.01 kg/m
Axial stiffness (EA)	3.53337E+08 N
Bending stiffness (EI)	1.37824E+05 Nm^2
Diameter	0.079 m
Ca, Cd	1, 1.5

Before the dynamic motion responses and stress resultants, the mode shapes need to be checked for the moored condition since the mode shapes are dependent on the boundary conditions. For verification purpose, two models are compared. To represent the freely floating Euler-Bernoulli beam, the beam with free ends is modeled. Meanwhile, the moored beam is modeled by combinations of the beam elements, connection springs, and rod elements as given in Figure 29.

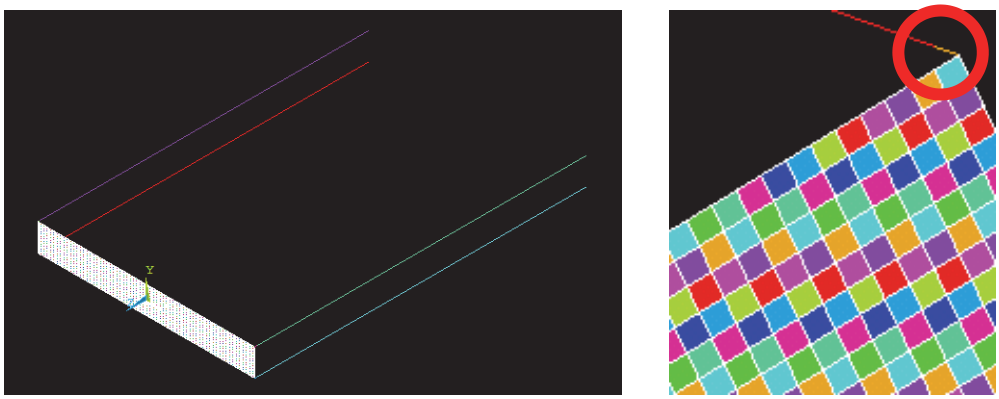

Figure 29. Finite element model of the moored slender pontoon: (a) schematic view and (b) local view at the connection

The moored slender pontoon requires the FEM for robust verification purpose since it is not capable of solving the beam equation with the nonlinear mooring lines without simplification to the linear spring. Both models are analyzed by the FEM, using Ansys and the mode shape and natural frequency are compared at each elastic mode.

All 8 elastic modes are checked and they show excellent agreement. The correspondence presents that the boundary conditions made by the mooring lines do not influence the mode shapes of the hull significantly, and thus it would be practically correct to use the analytic mode shapes for the free end condition. The comparisons for the first two elastic modes are demonstrated in Figure 30.

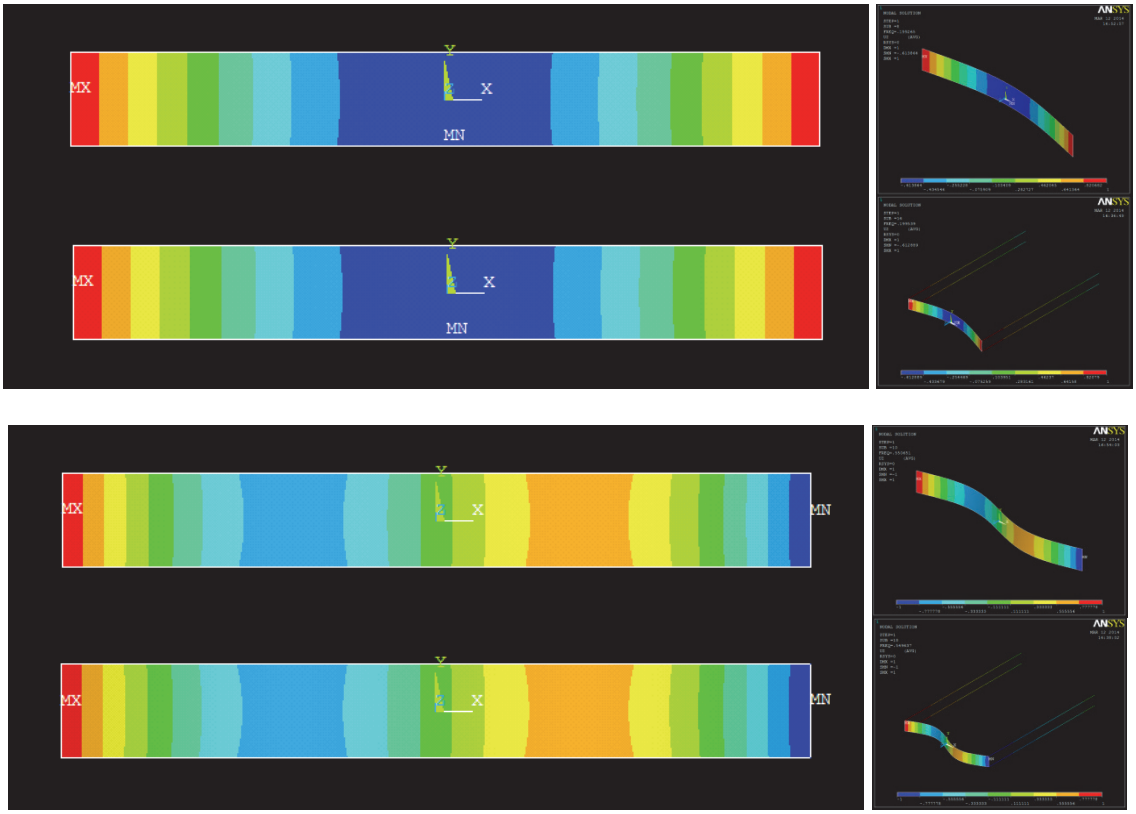

Figure 30. Modal analysis of the moored slender pontoon by FEM

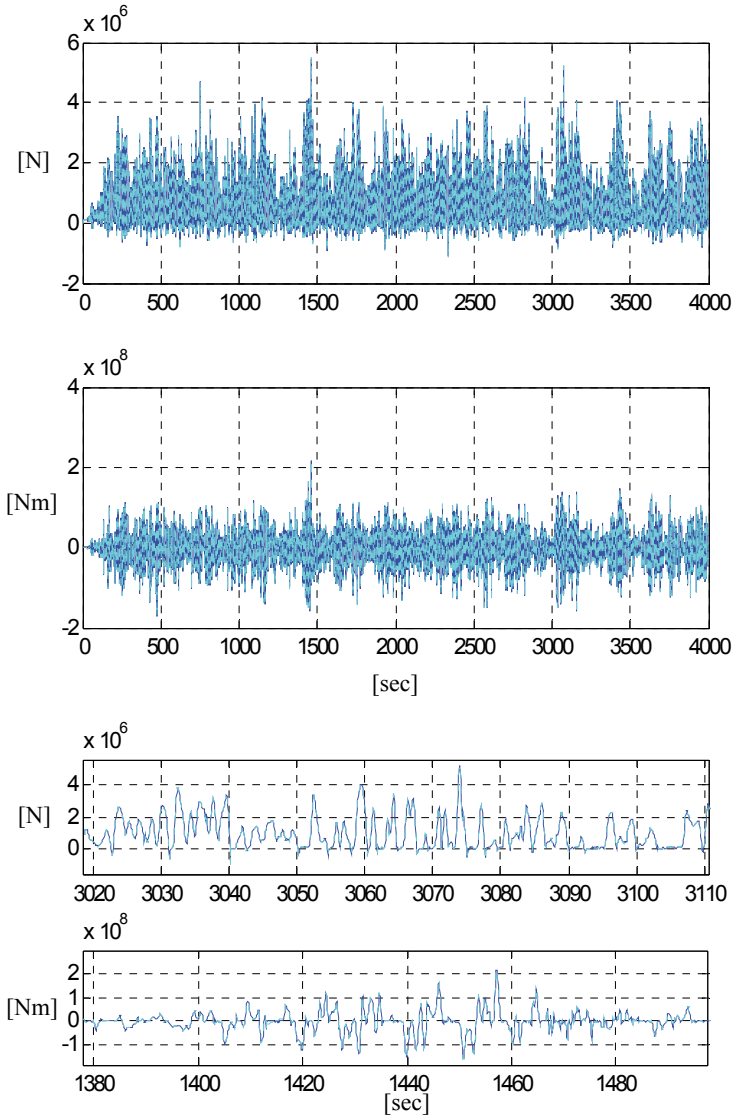

Figure 31. Comparison of the mooring-induced loads (cyan) with the rest of loads (blue) in the coupled hydroelastic analysis

For the verification purpose of the coupled hydroelastic analysis for the moored deformable body, the equilibrium of momentum is examined at each DOF. The excitation induced by the mooring tensions at each time step is compared against the rest

of loads of the governing equation. The correspondence of two proves the validity of the coupled hydroelastic analysis with the Jacobian matrices.

The equilibria for the heave and pitch are demonstrated in Figure 31. The mooring-induced forces and moments show excellent agreement with the rest of loads, which represents the satisfactory equilibrium. Therefore, the coupled hydroelastic dynamic analysis for the moored deformable body is successfully verified. To achieve such accuracy, the convergence test with respect to the time interval is indispensable along with the verified hydroelastic analysis for the freely floating deformable body.

Dynamic Motion Responses

To investigate interactions of the nonlinear mooring lines with the hull flexibility, the motion responses are compared between the freely floating and moored conditions in Figure 32. It is seen that the 8 elastic modes undergo signified excitations due to the interacting tensions of the mooring lines and the 6 DOF rigid motions show the conventional responses of the moored floating body.

To clarify the excitations of the elastic modes, the response spectra are compared with the modal excitation spectra purely generated by the mooring tensions in Figure 33.

It turns out that the elastic modes are mainly excited by the tensions in the high frequency region after 1.5 rad/sec and there exist amplified responses due to the resonance phenomena. For instance, the second elastic mode has notable responses in the natural frequency zone around the 2.82 rad/sec, although the modal excitations have very low energy. The resonance phenomena induce the shifted energy in the response spectra from the excitation spectra.

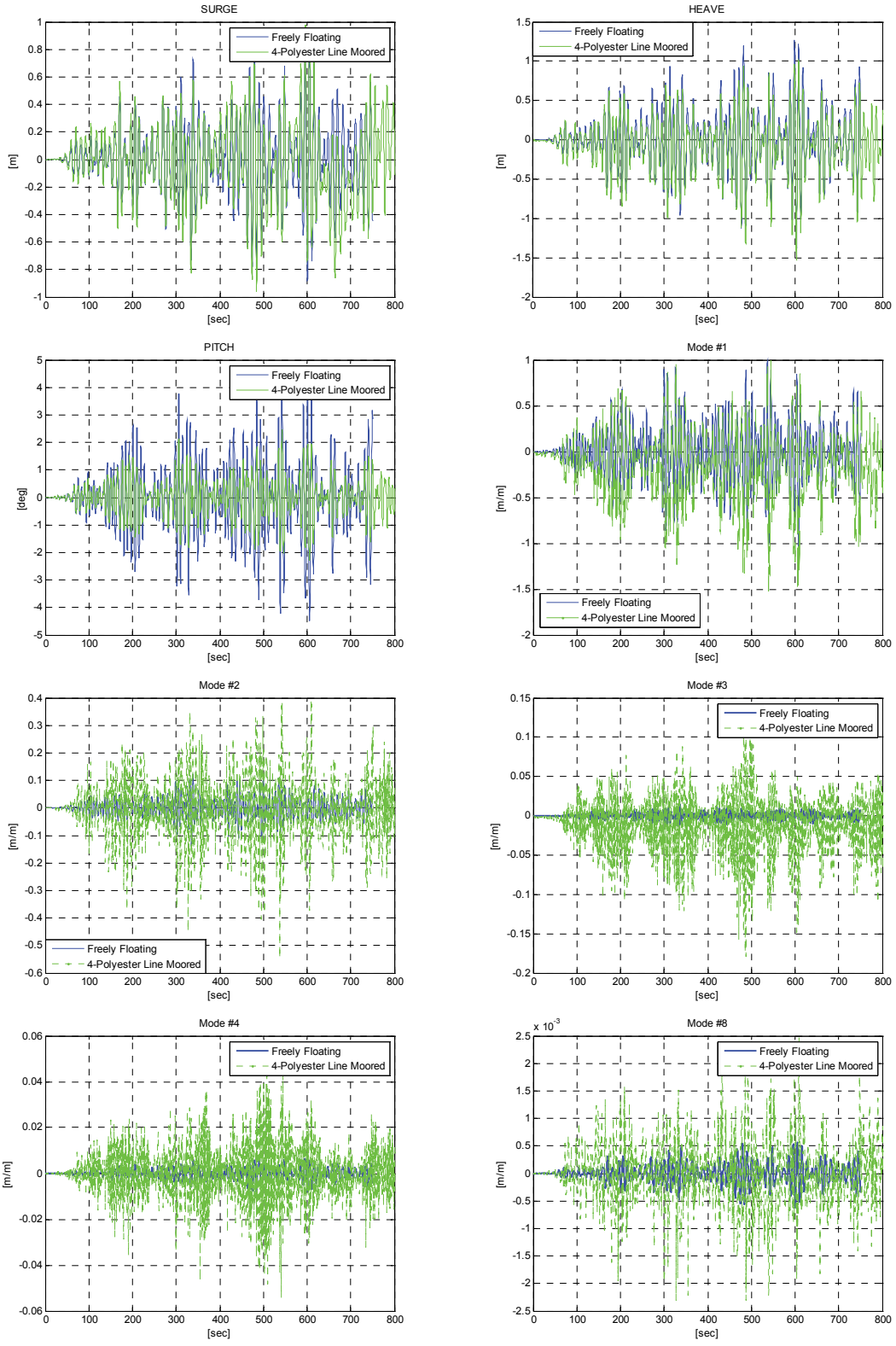

Figure 32. Hydroelastic dynamic motion responses for the moored slender body

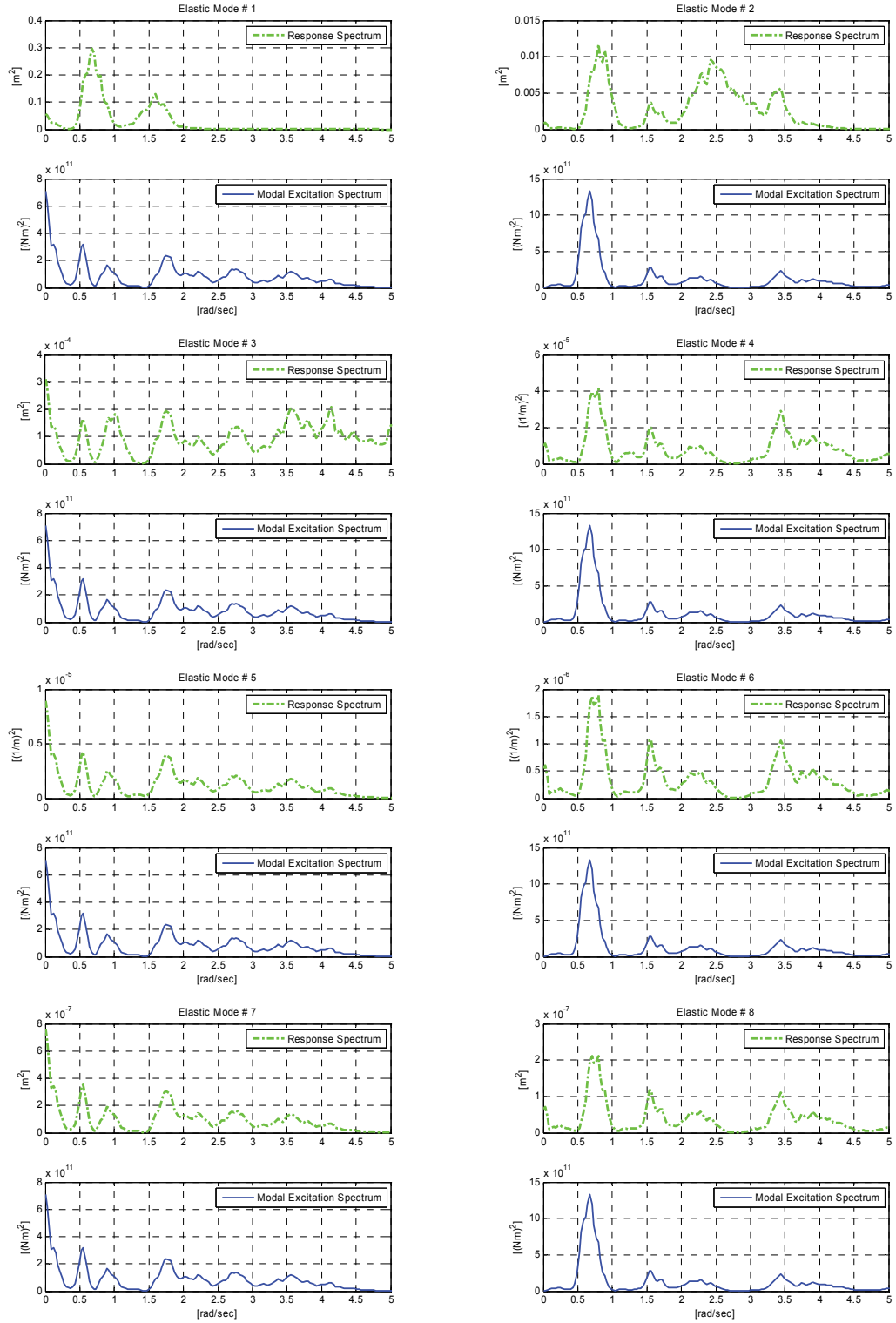

Figure 33. Correspondences between elastic modal responses and tension-induced modal excitations

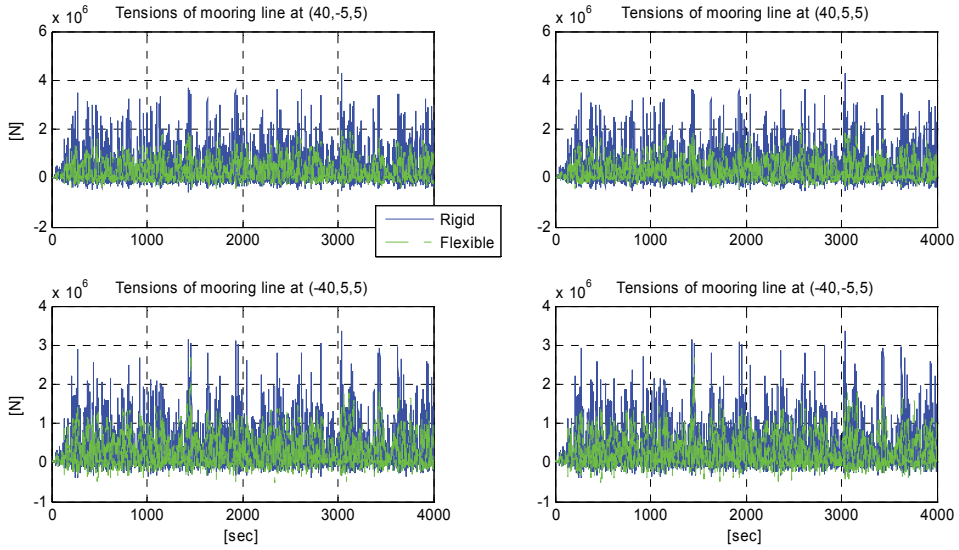

Figure 34. Tension comparison between the flexible and rigid body assumptions

To study the effects of the hull deformation into the mooring tensions, the tension records are compared between the rigid-assumed moored body and the moored deformable body in Figure 34. An interesting result is the tensions are reduced by the interacting hull deformation by about 50~60 %.

Dynamic Stress Resultants

The mooring tensions significantly influence overall stress resultant distributions when the mooring lines are taut conditions as shown in Figure 35. In such cases, the heave forces and pitch moments induced by the taut mooring tension are dominant components over the environmental loads, inertia loads, and restoring loads.

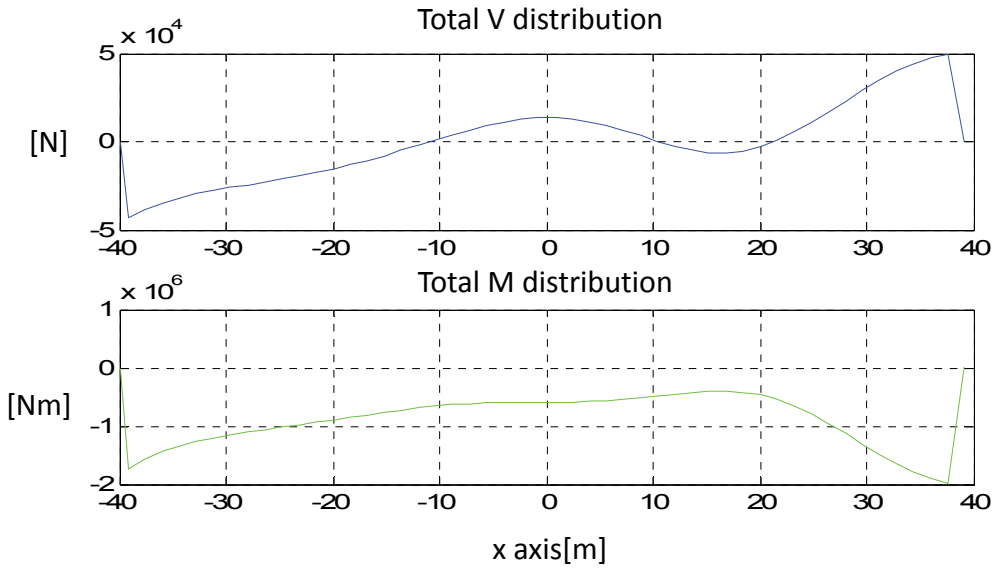

Figure 35. Dominant effects from mooring tensions

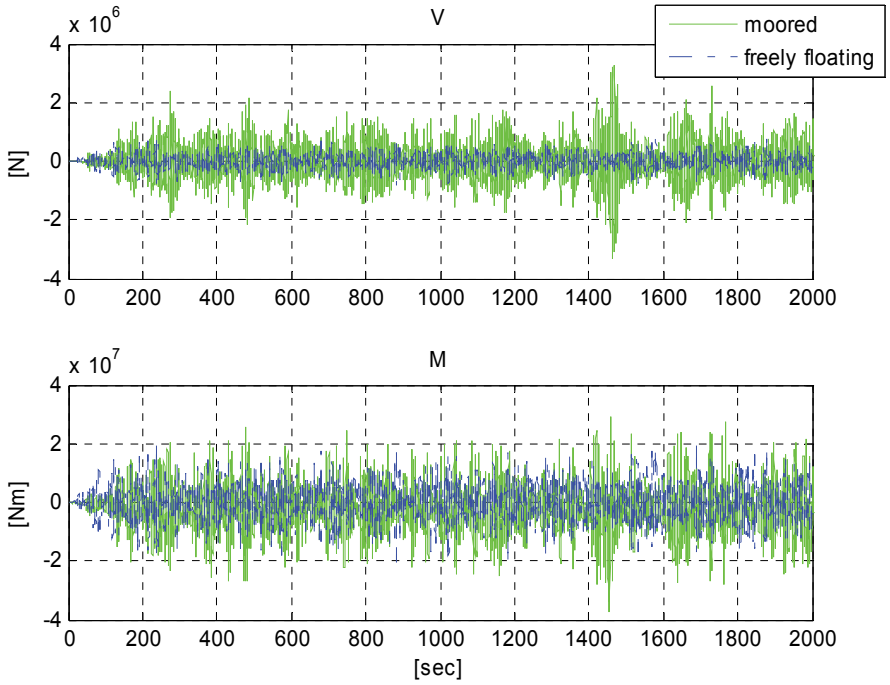

Figure 36. Stress resultant comparisons between the moored and freely floating conditions

The fully coupled hydroelastic structural analysis for the moored deformable body provides with overall larger magnitudes of the stress resultants than the freely floating condition. The shear forces and bending moments are compared between the freely floating and moored conditions at the quarter section and the mid-section, respectively, in Figure 36. The moored conditions generate larger stress resultants than the freely floating conditions.

To identify relative importance, the respective stress resultant components are compared in Figure 37. R, I, H stand for restoring, inertia, and hydrodynamic pressure effects, respectively, and L presents the stress resultants induced by the mooring lines.

In that the given random sea conditions for both freely floating and moored cases are fixed, the input energy can be regarded as same in both. Although overall scales are smaller in the moored condition, there exists an additional component induced by the mooring lines and it causes the larger magnitudes of the total stress resultants. Such tendencies are common in both shear forces and bending moments, and the details may vary at different measuring points.

Therefore, for a moored deformable body the coupled hydroelastic structural analysis provides more accurate stress resultants including significant interactions of the mooring line tensions. Based on the investigation, the uncoupled hydroelastic structural analysis may imply potential errors, which can be over 50 % from about 10 %, in stress resultants due to the absent mooring line effects.

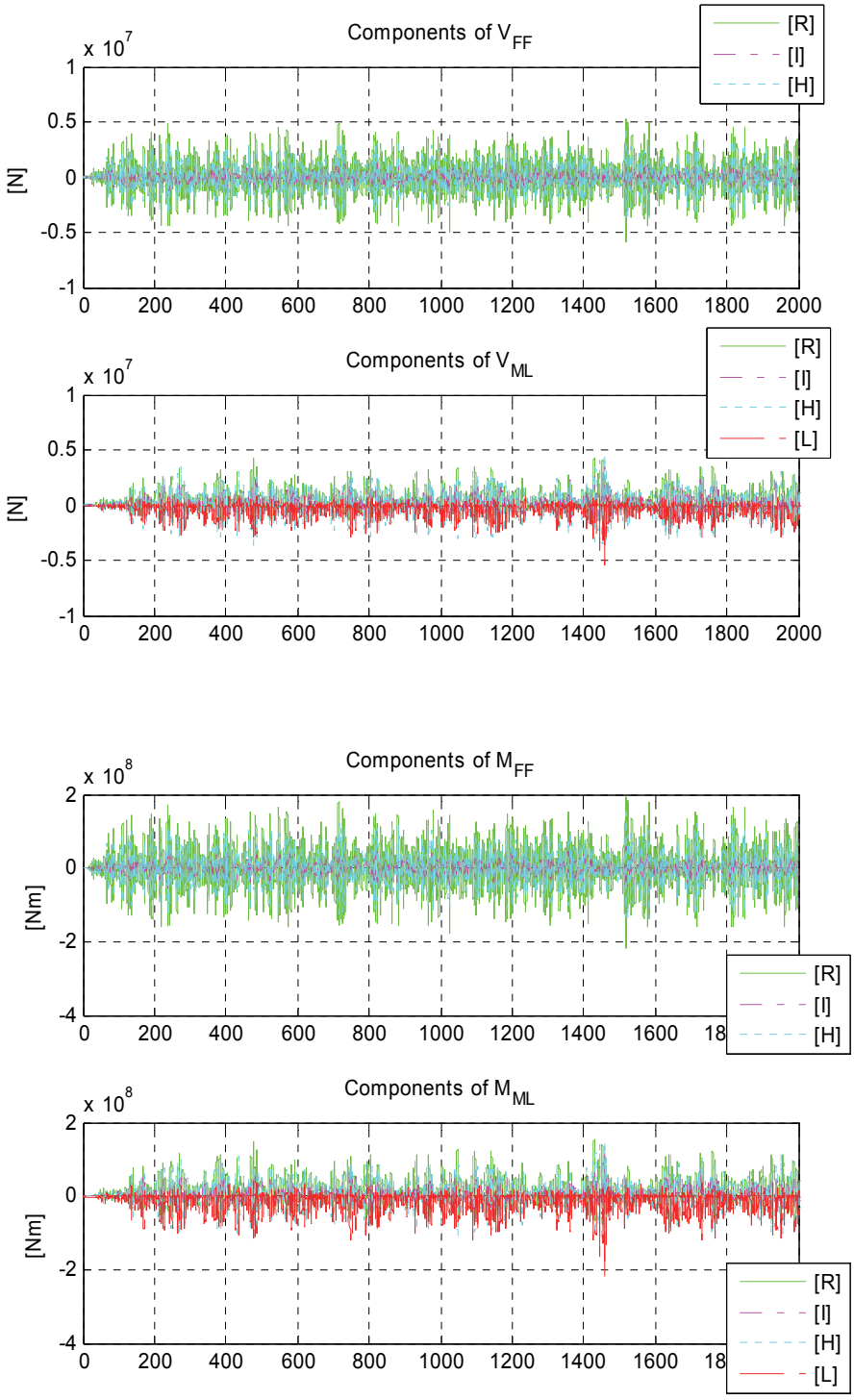

Figure 37. Componential comparison of irregular stress resultants for slender pontoon

Simplified 2nd Order Time Domain Analysis

Similarly to the freely floating case, the second order wave loads for the sum and difference frequencies are included into the random sea loads on the moored slender pontoon. The second order wave loads induce both of slowly varying motions and high-frequency oscillations to the moored slender pontoon. Subsequently, the second order induced motions of the pontoon interact with the mooring system.

The difference frequency wave loads generate the slowly varying motions in surge, and it causes the subsequent low frequency oscillations of the 2nd elastic mode. When the slender pontoon has the offset in the *x* axis, the corresponding axial tensions from the taut mooring system create the modal excitations for the 2nd elastic mode as compared against the 1st order analysis in Figure 38. Moreover, the coupling between the surge and 2nd elastic mode results in the negligible set-down of the pontoon.

The contributions from the 2nd order waves can be clearly seen from the response spectra comparison with the linear results in Figure 39. The comparison presents that the first elastic mode is dominantly excited by the sum-frequency wave loads and the second elastic mode has significant difference-frequency excitations.

The second order wave loads also influence the tensions of the mooring system as shown in Figure 40. The effects are mainly due to the deformations and rigid motions of the slender pontoon excited by the random wave loads including the second order wave loading. In this study, the tensions have about 20~30 % increments especially in the rear side mooring lines.

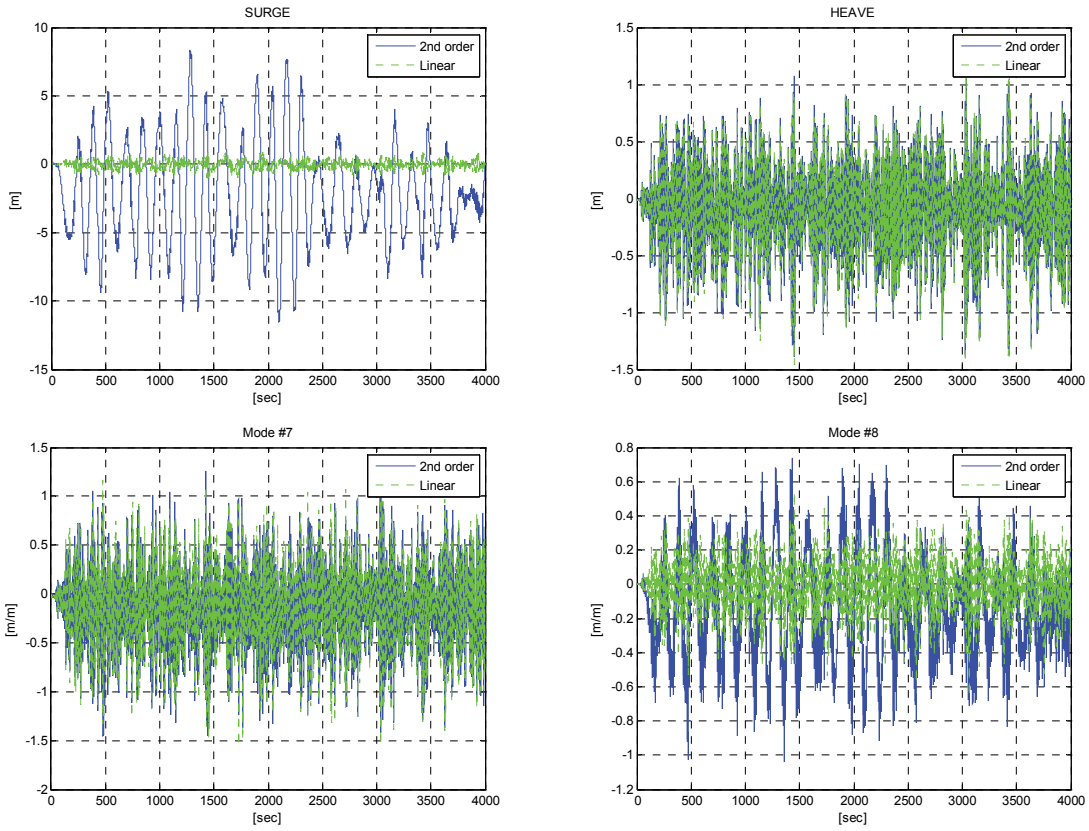

Figure 38. Time responses of slender pontoon including 2nd order wave loads

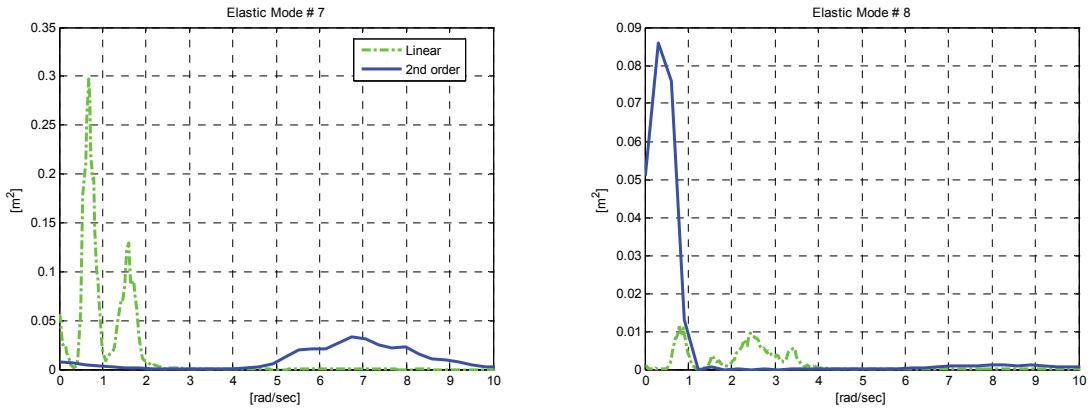

Figure 39. Elastic response spectra of slender pontoon including 2nd order wave loads

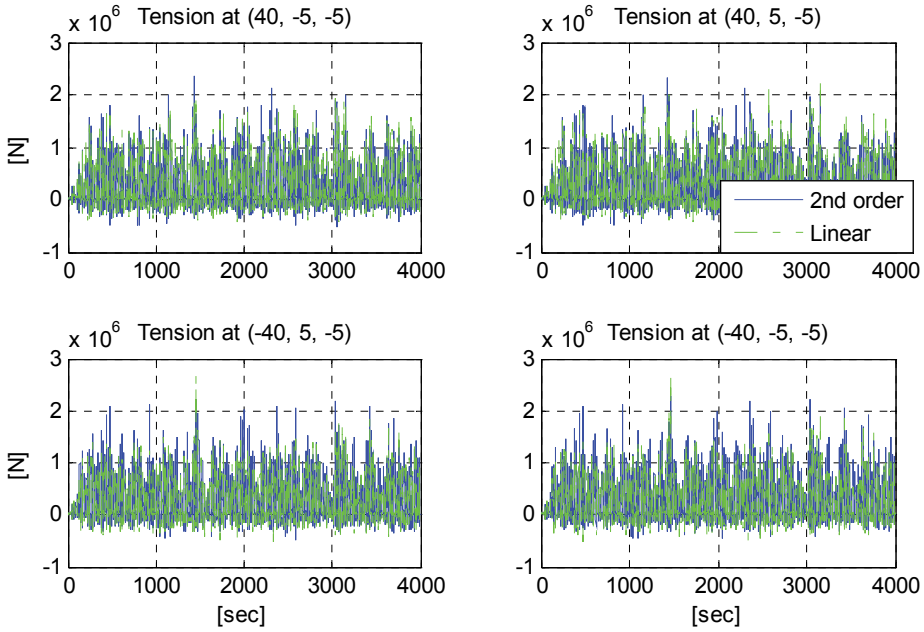

Figure 40. Tension comparison of mooring system for slender pontoon between linear order and 2nd order

7. NUMERICAL HYDROELASTIC ANALYSIS OF A THREE DIMENSIONAL STRUCTURE

The developed hydroelastic analysis is applied to a three dimensional large volume pontoon, which has about a unit aspect ratio in 400 m scale. The box barge with 480 m length, 400 width, and 8 m draft in Figure 41 is designed for the three dimensional hydroelasticity. The mass is 1.539E+9 kg, and the mass moment of inertia is 2.051E+13 kgm^2 for roll, 2.952E+13 kgm^2 for pitch, 4.997E+13 kgm^2 for yaw.

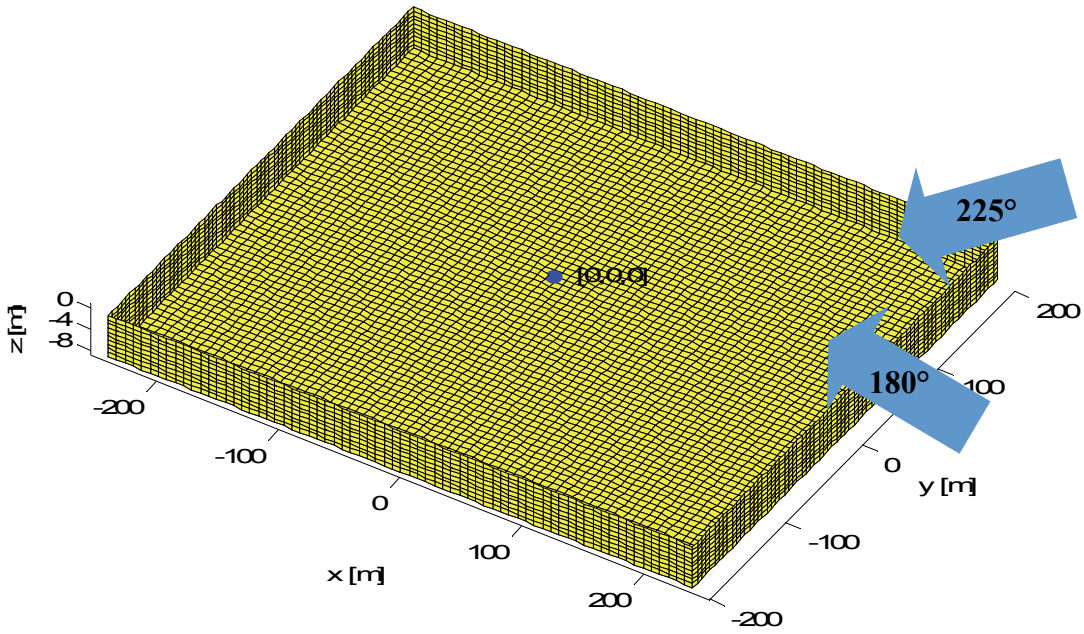

Figure 41. Schematic view of box barge for 3D hydroelasticity (reprinted with permission, Kang and Kim [15])

The modal analysis is implemented by the FEM. Although such a wide pontoon is in general modeled by the plate theory, the analytic solution for the all free boundary conditions is not available. As simplification, one can use the Rayleigh dimensional

analysis, which consists of the product series of two beam theory solutions for the *x* and *y* axes. The Rayleigh dimensional analysis, however, can be regarded as semi-analytic method in that it requires experimental coefficients at each term to correspond to the experimental mode shapes. It is more beneficial to adopt the FEM for the cases with the analytic solutions unavailable. In this study, an example of the generalized hydroelastic analysis with the FEM adopted is described in order to account for the 3D hydroelasticity.

Total 7957 elastic elements with 3 translational and 3 rotational DOFs at each element are used. The Poisson's ratio is assumed to be 0.3. The modal analysis is conducted by using Ansys as summarized in Table 5.

Table 5. Modal analysis of 3D large pontoon

Elastic mode number	Modal inertia [kgm^2]	Modal stiffness [Nm]	Dry Natural frequency [rad/sec]
1	2.123E+8	1.173E+9	2.351
2	3.075E+8	2.915E+9	3.079
3	2.502E+8	5.560E+9	4.714
4	1.841E+8	6.030E+9	5.723
5	2.363E+8	1.007E+10	6.530
6	2.308E+8	1.847E+10	8.946
7	1.767E+8	2.220E+10	11.207
8	2.309E+8	2.913E+10	11.233

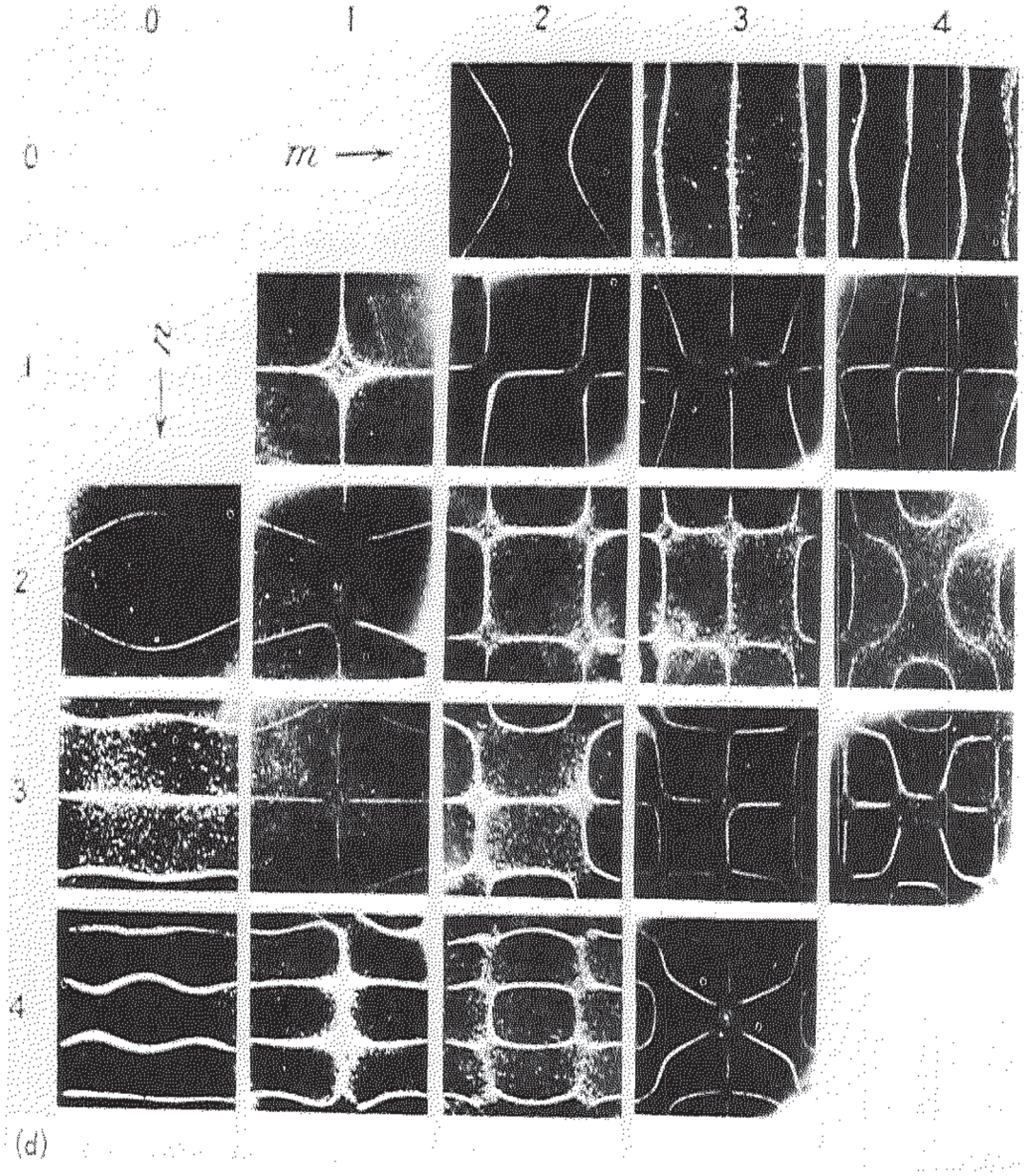

Figure 42. Experimental results of mode shapes for aspect ratio 1.09. Adapted from "Vibration of Plates" by Arthur W. Leissa, 1969, NASA, SP-160, p. 115 [26]

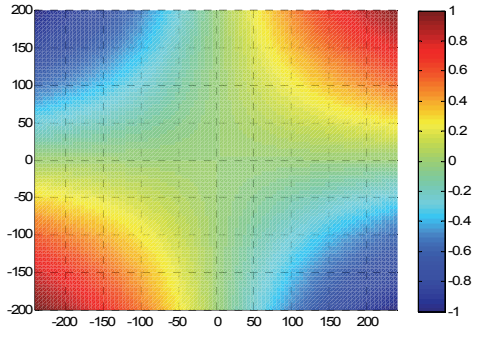

Elastic mode #1, corresponding n=1, m=1 in experiments

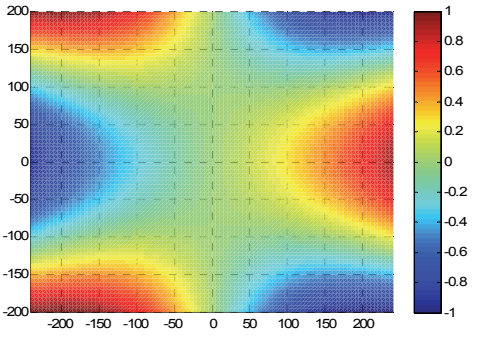

Elastic mode #5, corresponding n=2, m=1 in experiments

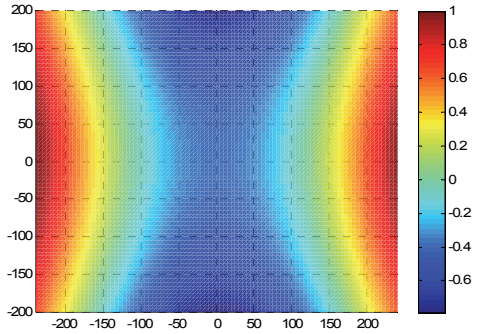

Elastic mode #2, corresponding n=0, m=2 in experiments

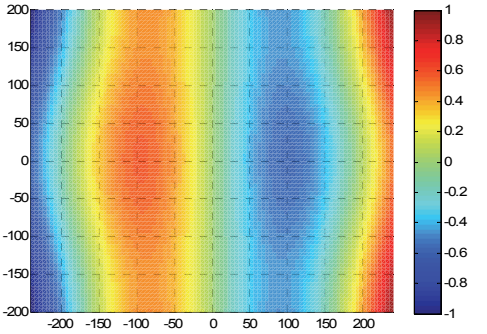

Elastic mode #6, corresponding n=0, m=3 in experiments

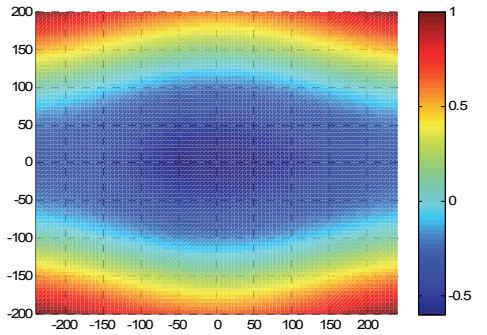

Elastic mode #3, corresponding n=2, m=0 in experiments

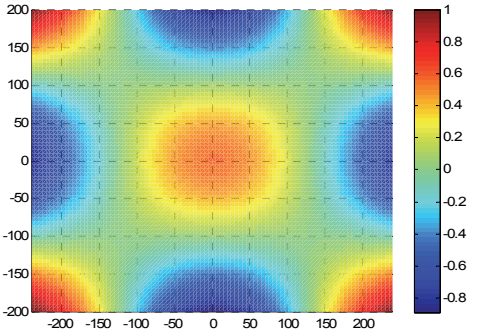

Elastic mode #7, corresponding n=2, m=2 in experiments

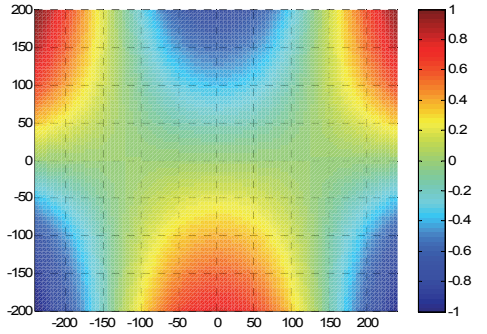

Elastic mode #4, corresponding n=1, m=2 in experiments

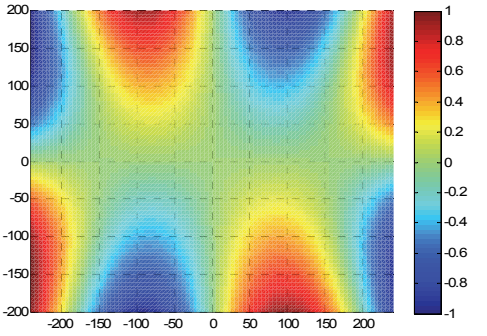

Elastic mode #8, corresponding n=1, m=3 in experiments

Figure 43. Total 8 mode shapes for 3D hydroelasticity and correspondences to experimental results (reprinted with permission, Kang and Kim [15])

The first elastic mode is designed to have the dry natural frequency at 2.351 rad/sec. To verify the mode shapes given by the numerical simulation, experimental results with the similar aspect ratio in Figure 42 are compared. The 3D pontoon has the aspect ratio 1.2, whereas the experimental plate is 1.09. Each of mode shapes from the numerical modal analysis has the coincided mode shape pattern with the corresponding experimental result as described in Figure 43.

The agreements of the mode shapes support the validity of the numerical modal analysis.

The elastic mode # 1, 4, 5, and 8 are torsional deformations. They have similarity of mode shapes. The higher number of torsional mode can be regarded as the higher order of torsional deformation as given in Figure 44. The 8 elastic modes including torsional effects are applied to the 3D hydroelastic analysis.

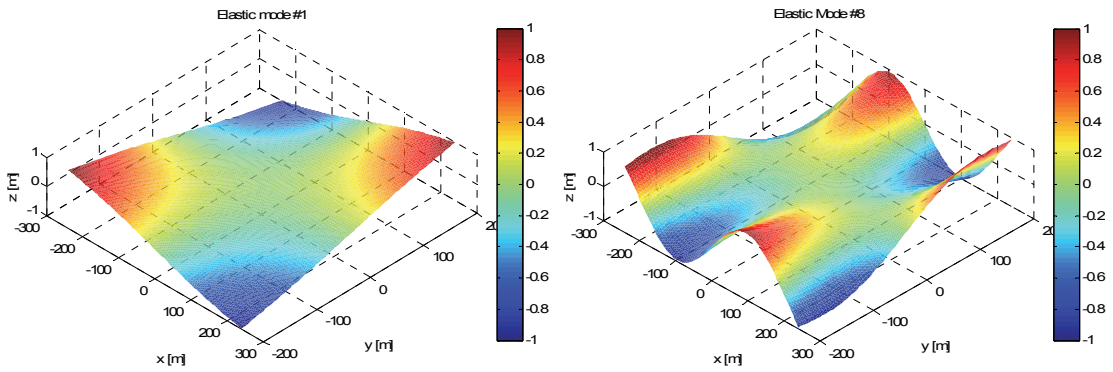

Figure 44. Similarity of mode shapes (reprinted with permission, Kang and Kim [15])

Hydroelastic Dynamic Analysis

Solving the present 3D hydroelastic problem, we can first identify the water contact effects are significant due to the very large submerged volume and there exist the notable coupling effects among the similar shapes of elastic modes.

The modal stiffness is affected by the hydrostatic stiffness as well as there are coupling hydrostatic stiffness effects among all the rigid and elastic modes. For instance, the first two elastic modes have about 30 % increased to 1.43E+9 and 3.92E+9 Nm of the modal hydrostatic stiffness. Geometric configuration of mode shapes induces strong coupling even between rigid modes and elastic modes. The first elastic mode has the strong coupling with yaw by $K_{7,6}$=−2.11E+9 Nm. It is because the first elastic mode is antisymmetric twisting deformation, which is vulnerable to yaw. In the elastic modes, the mode #1 and 8 have similarity of geometry and the corresponding coupling stiffness $K_{7,14}$=$K_{14,7}$=−4.13E+4 Nm. Moreover, elastic modes #5 and 6 with antisymmetric geometry in surge have notable coupling effects with surge similarly to the combination of mode #4 and sway. It is also notable that coupling effects are also promoted by weighty added inertia at those coupled modes.

Considering the main focus in this case study is the 3D hydroelasticity, both head seas (180 º) and quartering seas (225º) are applied to the 3D pontoon.

Frequency Domain

RAOs are compared between the head sea and quartering sea in Figure 45 to investigate the dependency of wave directions.

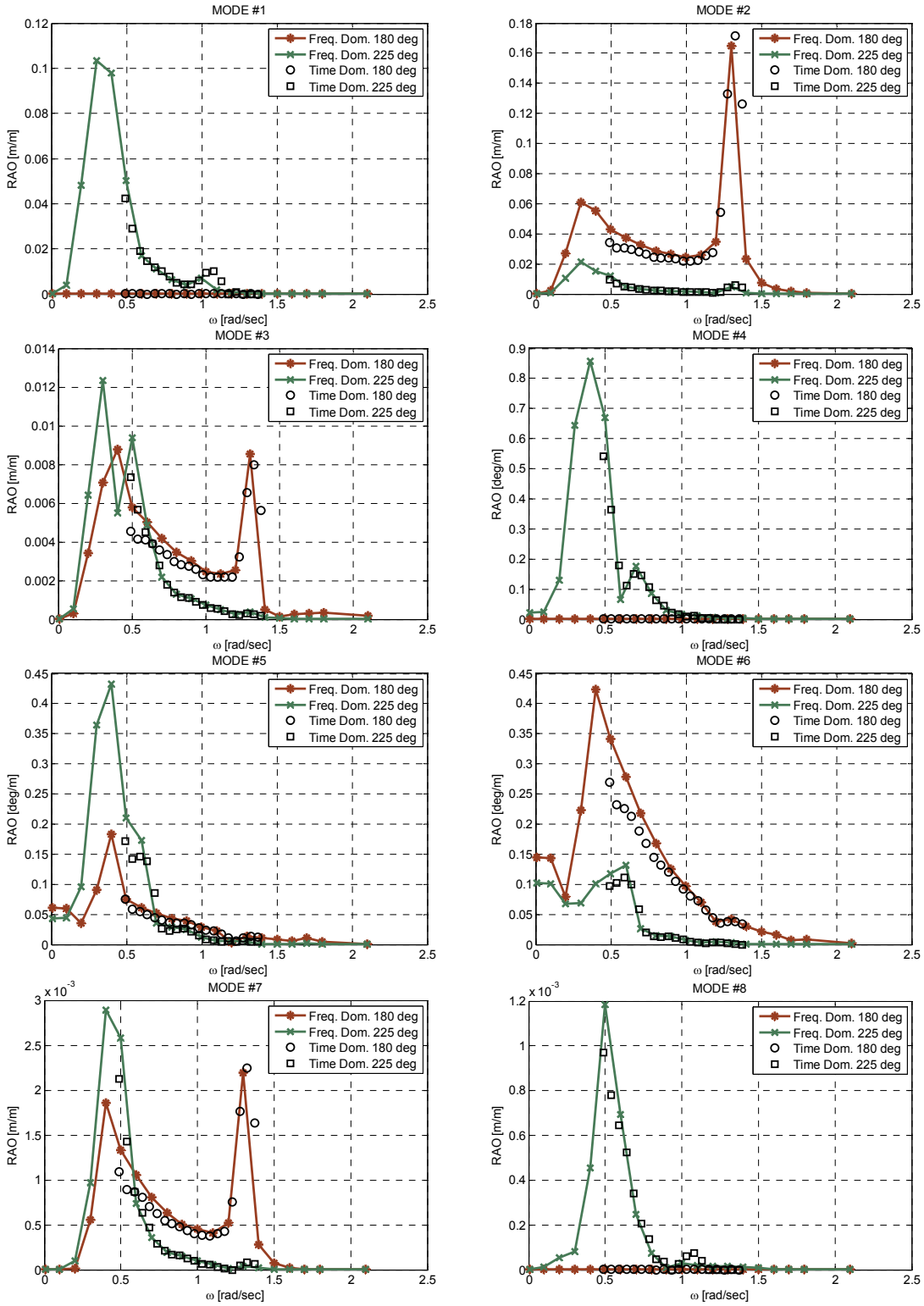

Figure 45. RAO comparisons of 3D hydroelasticity for head sea and quartering sea; MODE means elastic mode (reprinted with permission, Kang and Kim [15])

To represent the validity of the hydroelastic dynamic analysis in both frequency and time domain, the spectral RAO from the time domain is compared with the frequency domain RAO. The spectral RAOs from time domain show good agreements with the frequency domain RAOs and the correspondence represents the validity of the developed 3D hydroelastic dynamic analysis. Comparing the RAOs with respect to the wave heading, not only the 6 rigid modes but also the 8 elastic modes have strong dependency on the wave heading. The elastic modes 1, 4, 5 and 8, which have torsional deformations, are notably responded to the oblique waves, whereas the elastic modes 2, 3, 6, and 7 are promoted by the head sea waves.

In resonance wise, the first elastic mode has the resonance peak at about 1.1 rad/sec and the second mode is resonated at about 1.35 rad/sec. Moreover, the second elastic mode induces the coupled resonance peaks at the elastic modes 3 and 7. The natural frequencies of the elastic modes are mainly reduced due to the dominant increases by the added inertia. Even in small scale, the elastic mode 8 has the coupled resonance peak with the first elastic mode. The coupling effects among the elastic modes are induced by the geometric similarity of the elastic mode shapes.

Along with the wave heading dependency and geometric similarity dependency, another interesting phenomenon can be found, excitation feasibility. Focusing on the resonances of the first two elastic modes in both headings, the first mode has even lower resonance peak than the second mode. It is mainly due to the feasibility of wave excitation for each elastic mode. From the comparison of wave excitation for each

elastic mode in Figure 46, it turns out that the torsional mode is harder to be excited and thus the modal excitation of that mode is smaller than bending deformation.

In same scale, the second elastic mode has much large modal excitation at the resonance peak for the head sea condition than the first elastic mode in the quartering sea condition. From the modal excitation comparison, one can conclude that the feasibility of the modal excitation, which is dependent on the mode shape, is another main factor to determine the hydroelastic dynamics beyond the wave heading dependency.

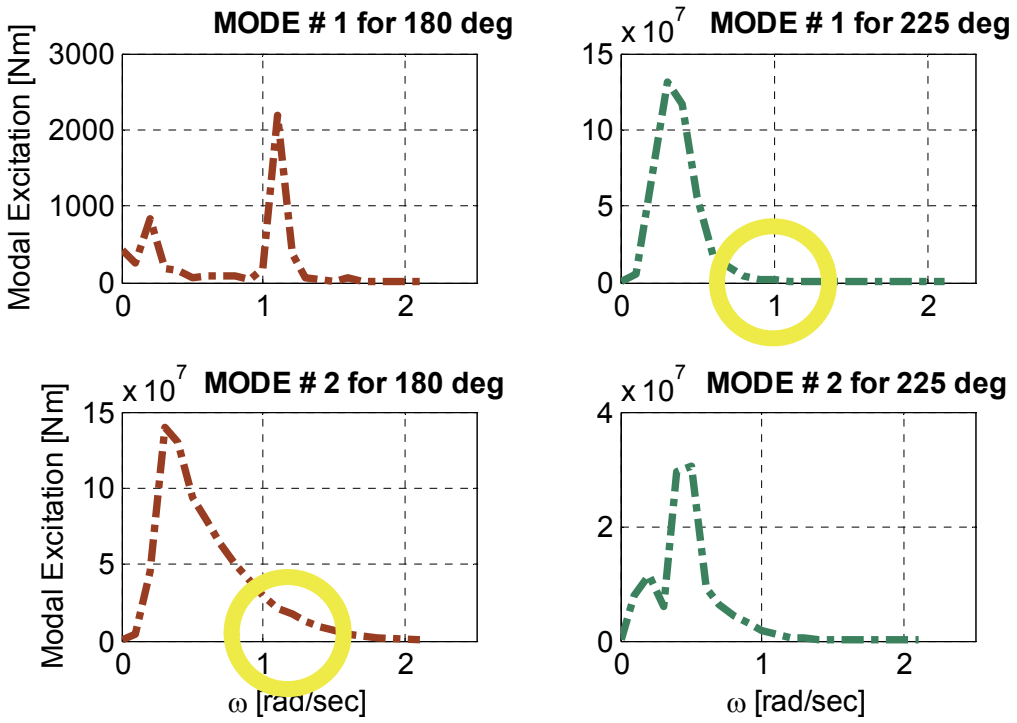

Figure 46. Feasibility comparison of modal excitations (reprinted with permission, Kang and Kim [15])

Numerical Hammer Test

The real wet natural frequencies are calculated from the numerical hammer test as shown in Figure 47. The large volume of the 3D pontoon implies significant change of the natural frequency due to the water contact effects such as added inertia and hydrostatic stiffness. After the instant vertical impact at the top right corner, the total deformations are measured at the left bottom corner along the time and the response spectrum of the free vibration is obtained. From the free vibration spectrum, the natural frequencies of respective elastic modes are identified. In the free vibration spectrum of Figure 48, the peaks represent resonance peaks.

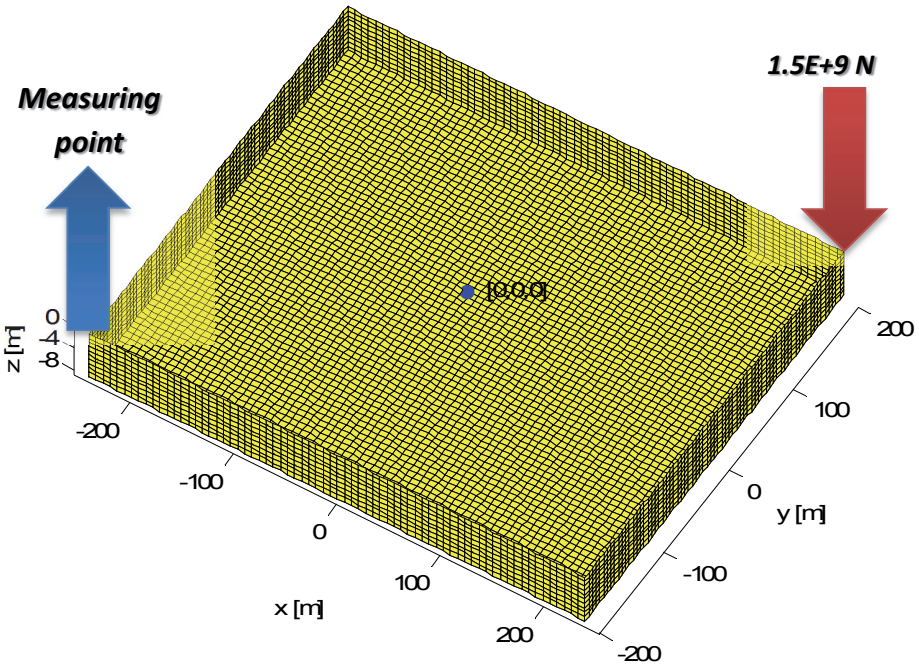

Figure 47. Numerical hammer test of 3D pontoon

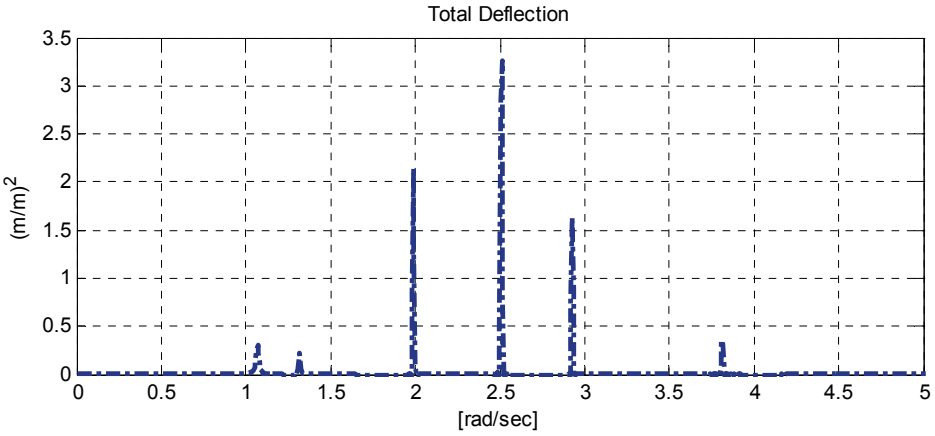

Figure 48. Response spectrum of responses to free vibration

Taking the peak frequencies from 1 to 5 rad/sec, the first 6 elastic modes are compared between the wet and dry natural frequencies. The wet natural frequencies summarized in Table 6 are significantly reduced from the dry ones since the increase of added modal inertia is relatively dominant than the hydrostatic effects.

Table 6. Comparison of wet and dry natural frequencies

Elastic mode number	Wet Natural Frequency [rad/sec]	Dry Natural Frequency [rad/sec]
1	1.04	2.351
2	1.30	3.079
3	2.00	4.714
4	2.50	5.723
5	2.90	6.530
6	3.70	8.946

The first two elastic modes confirm that the peaks around the frequencies in the RAOs are resonance peaks. Moreover, the resonance phenomena are well-captured in the hydroelastic dynamic motion RAOs.

Time Domain

The head random seas and quartering random seas for the sea state 5 are investigated with cross-comparisons in Figure 49. The 6 rigid modes show conventional tendency as normal floating body interactions such that the oblique waves excite both *x* and *y* directional motions simultaneously with the yaw motions.

In Figure 50, the first 2 elastic modes show the resonance phenomena for the oblique waves and head waves, respectively. The promoted resonance peaks can be found in the response spectra of Figure 51.

Although both elastic modes have resonance peaks, main wave energy frequency is dominant in the first elastic mode and the second elastic mode has significant peak at the natural frequency. The energy difference of the both resonance peaks is mainly due to the excitation feasibility.

The torsional elastic modes such as mode # 1, 4 and 8 are heavily excited by the oblique waves and the elastic mode # 5 has relatively small amount of amplification than the three torsional modes since the wave energy is decreasing in the range where the promoted responses occur in the RAO. As a higher order of bending deformation, the elastic mode #6 has large motions in the head sea condition, which represents the wave heading dependency.

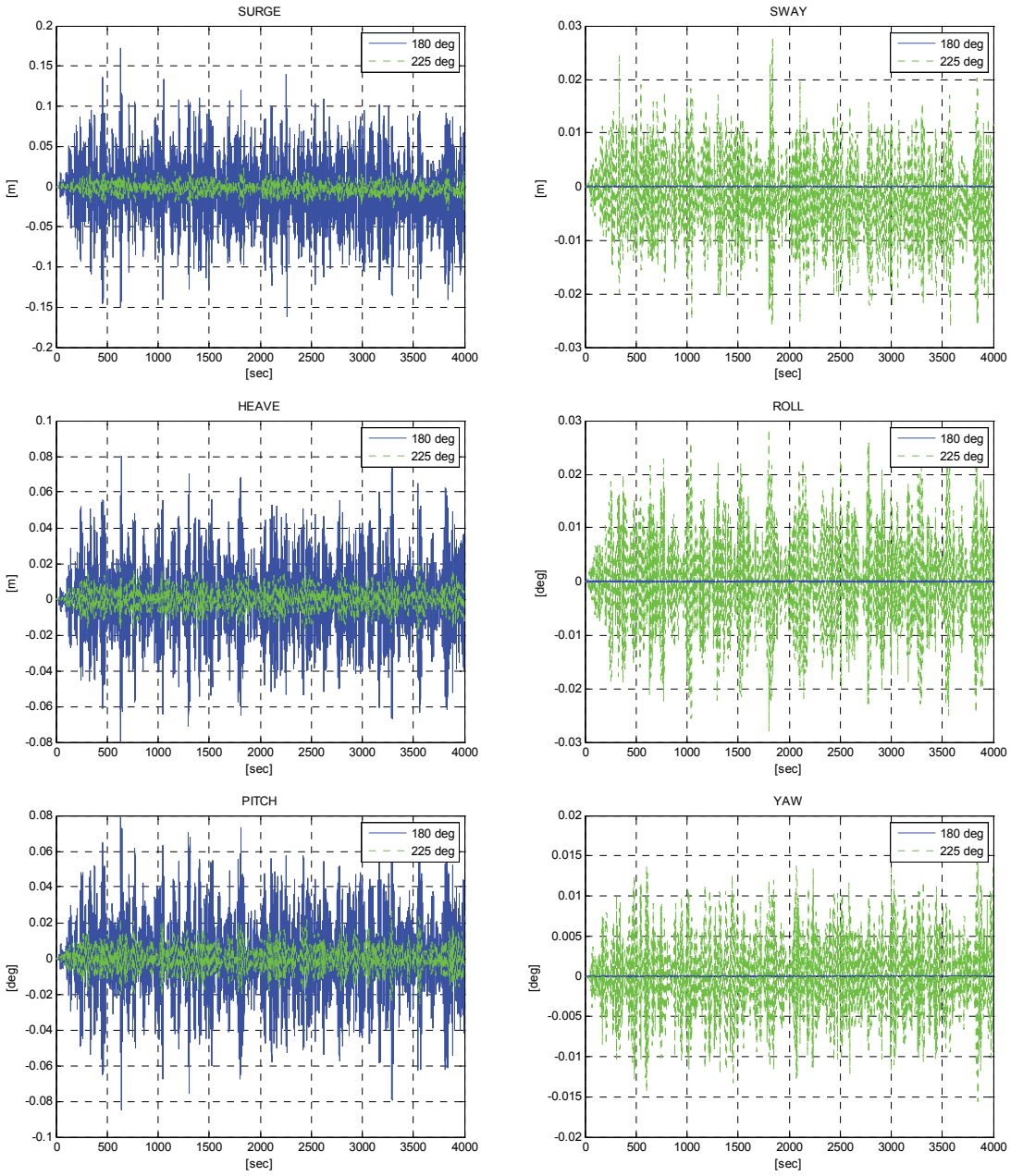

Figure 49. Comparison of 6 rigid mode responses for 3D pontoon

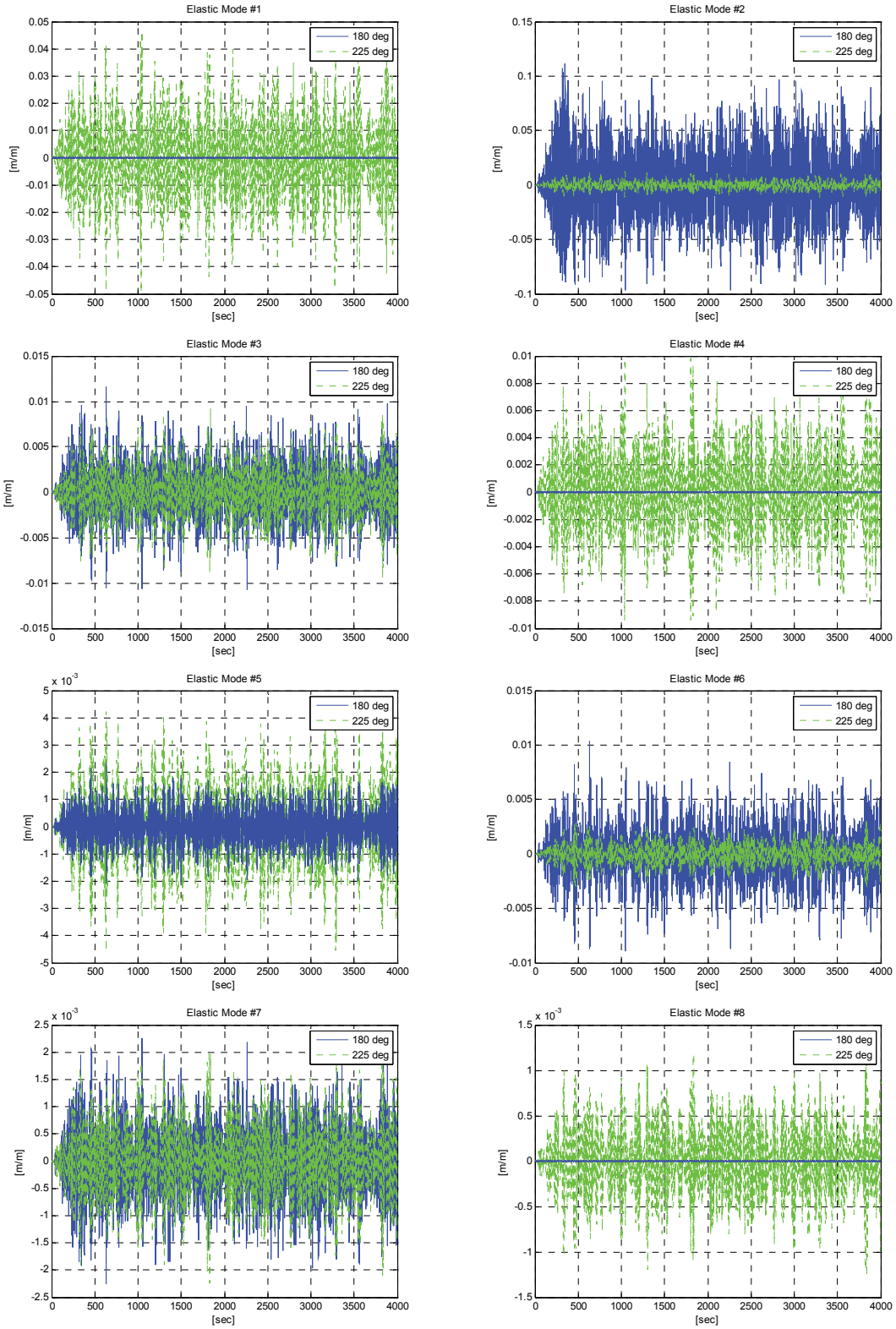

Figure 50. Comparison of 8 elastic mode responses for 3D pontoon

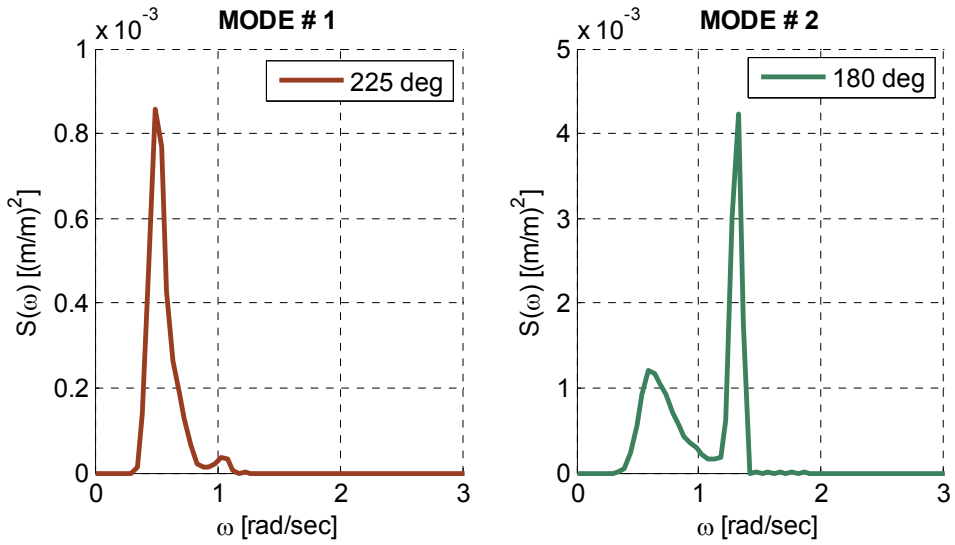

Figure 51. Response spectra of elastic mode #1 and 2 for 3D pontoon (reprinted with permission, Kang and Kim [15])

Simplified 2nd Order Time Domain Analysis

The second order wave loads are included to the time-domain hydroelastic dynamic analysis for the 3D pontoon. The pontoon is freely floating and only sum-frequency wave loads are applied in order to identify the high frequency resonance.

To generate the random seas, the JONSWAP spectrum with Hs=5, Tp=10.6, and Gamma=1.6 is used. In comparison between the linear case and 2nd order case in Figure 52, the elastic modes undergo amplified high-frequency oscillations after the first elastic mode. In the freely floating condition, it turns out that the first and 2nd order waves rarely generate the first elastic modal excitations and subsequent higher-order twisting elastic modes such as elastic modes #4, 6, 7 and 8.

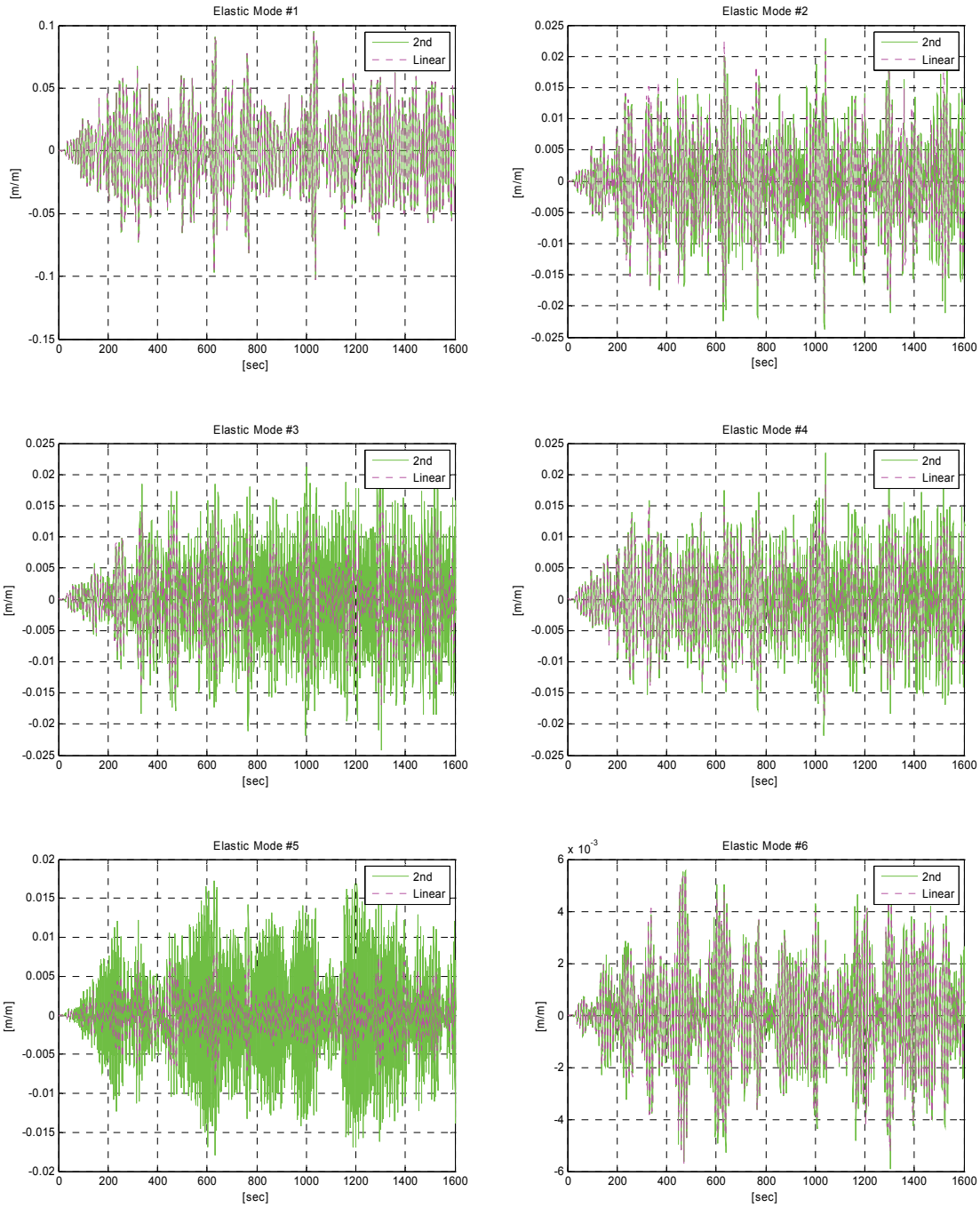

Figure 52. Time series of resonated elastic modes due to 2nd order wave loads for 3D pontoon

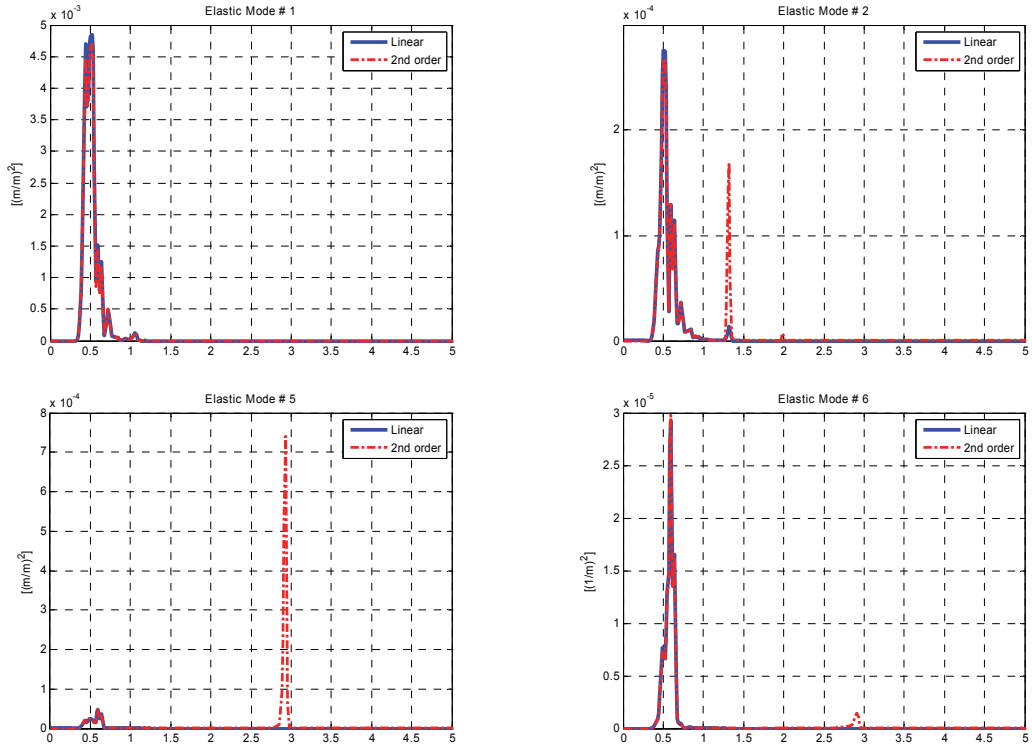

Figure 53. Response spectra of resonated elastic modes due to 2nd order wave loads for 3D pontoon

Contrary to the twisting elastic modes, the deflection deformation in the *x* and *y* axes are significantly excited by the second order wave loads. Especially, the elastic mode # 5 is dominantly amplified by the sum-frequency wave loads. The differences are clearer in comparison of response spectra.

The second elastic mode has amplified resonance peak in the 2nd order case, and the higher motions have the resonance peaks only in the 2nd order analysis. While the twisting elastic modes have dominant response energy from 0.3 to 1 rad/sec as given in spectra for elastic mode #1 and 6, non-twisting elastic modes undergo strong or overwhelming resonance peaks as the elastic mode # 2 and 5 shown in Figure 53.

Hydroelastic Structural Analysis

In the present 3D hydroelastic structural analysis, three types of stress resultants, shear forces V(x,y), bending moments M(x,y), and torsional moments T(x,y), are achieved for both x and y axes as given in Figure 54. The oblique random wave case is adopted for the comprehensive structural analysis.

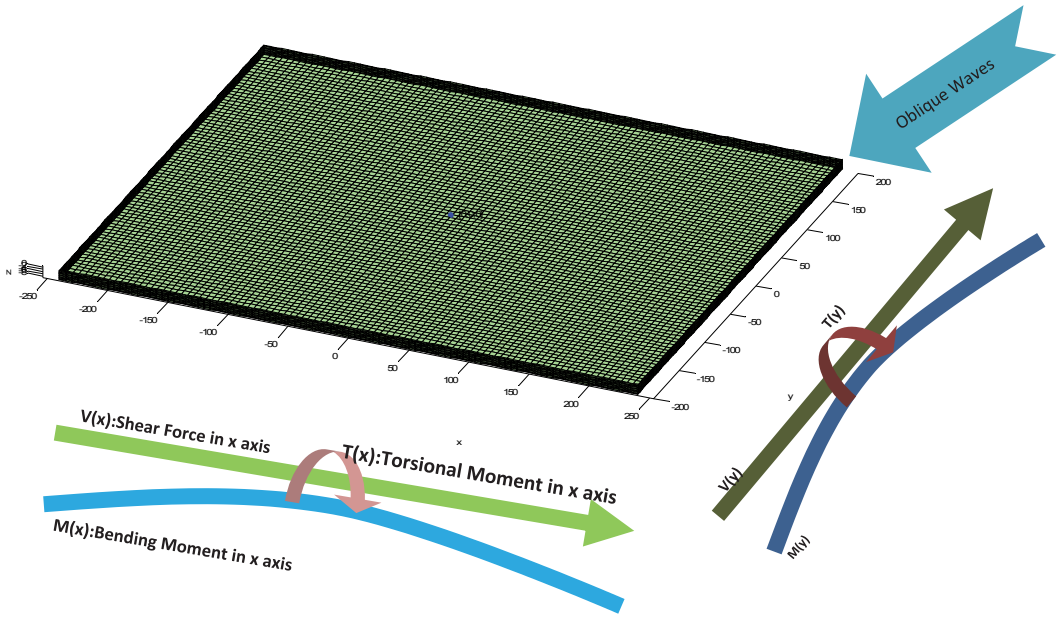

Figure 54. Schematic view of 3D stress resultants

For the purpose of robust verification, respective stress resultants are compared between the frequency and time domains in terms of stress resultants RAOs. Not only the total stress resultants but also the componential stress resultants are verified.

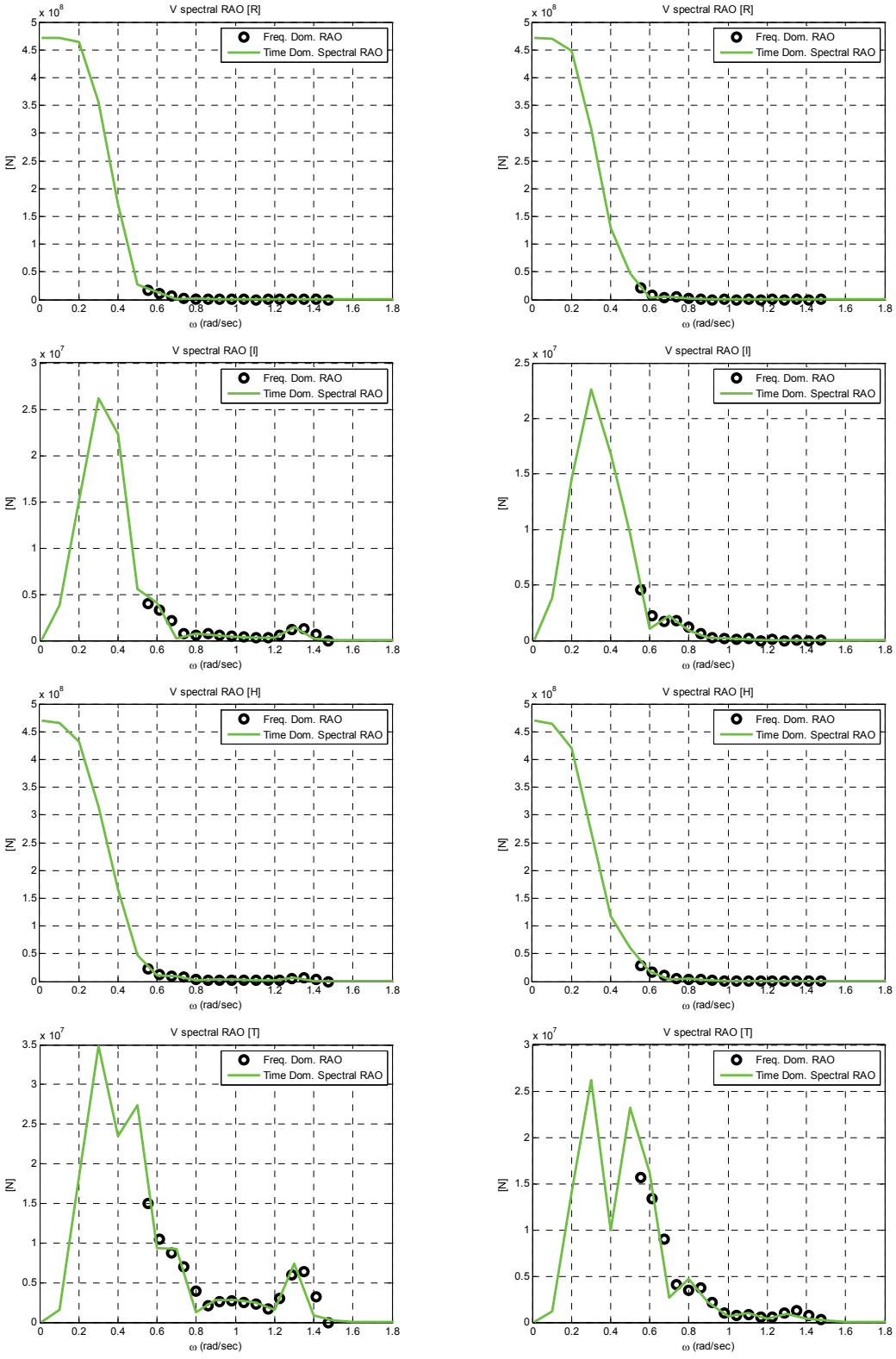

Figure 55. Verification of 3D hydroelastic structural analysis for shear forces

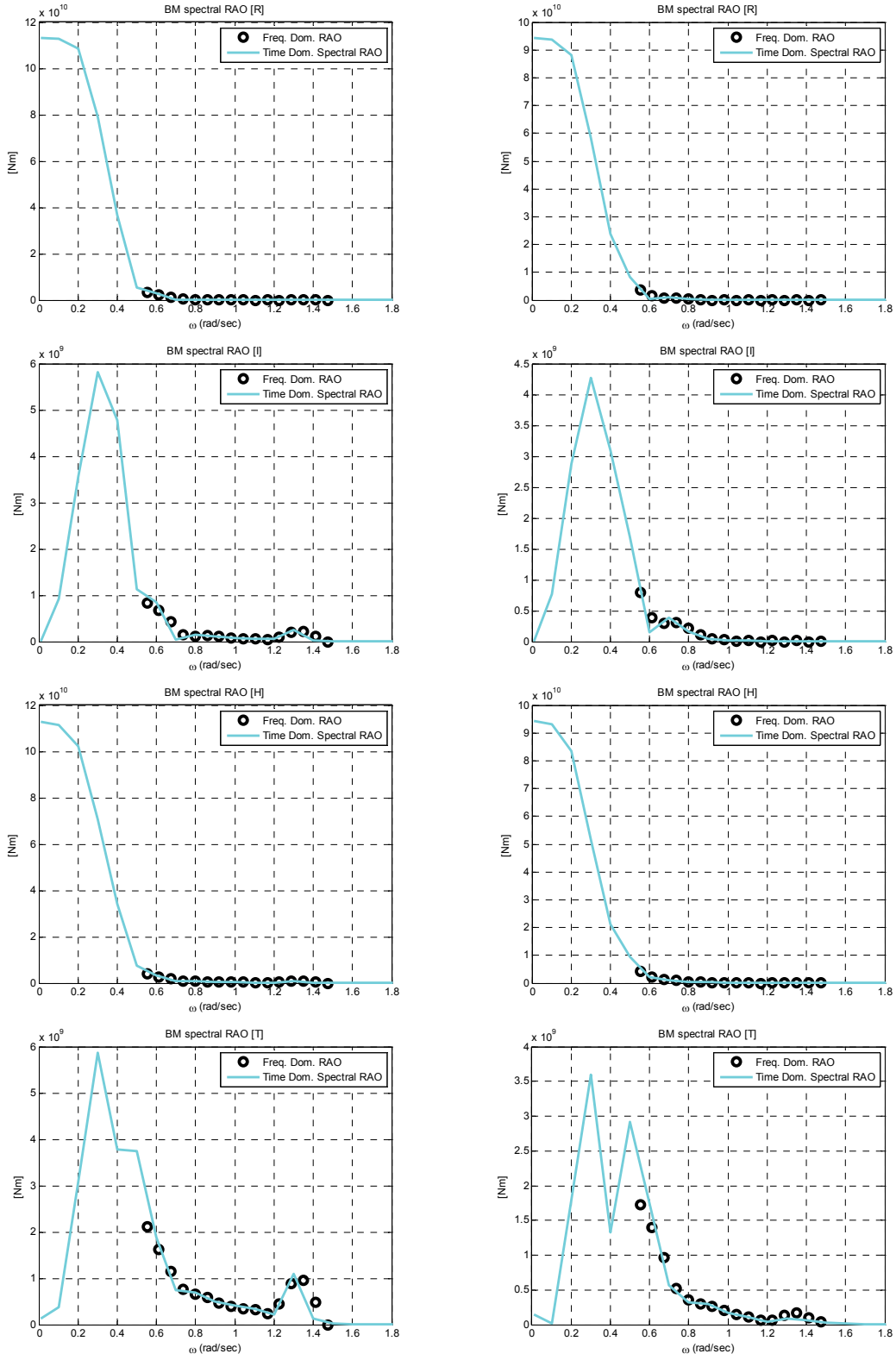

Figure 56. Verification of 3D hydroelastic structural analysis for bending moments

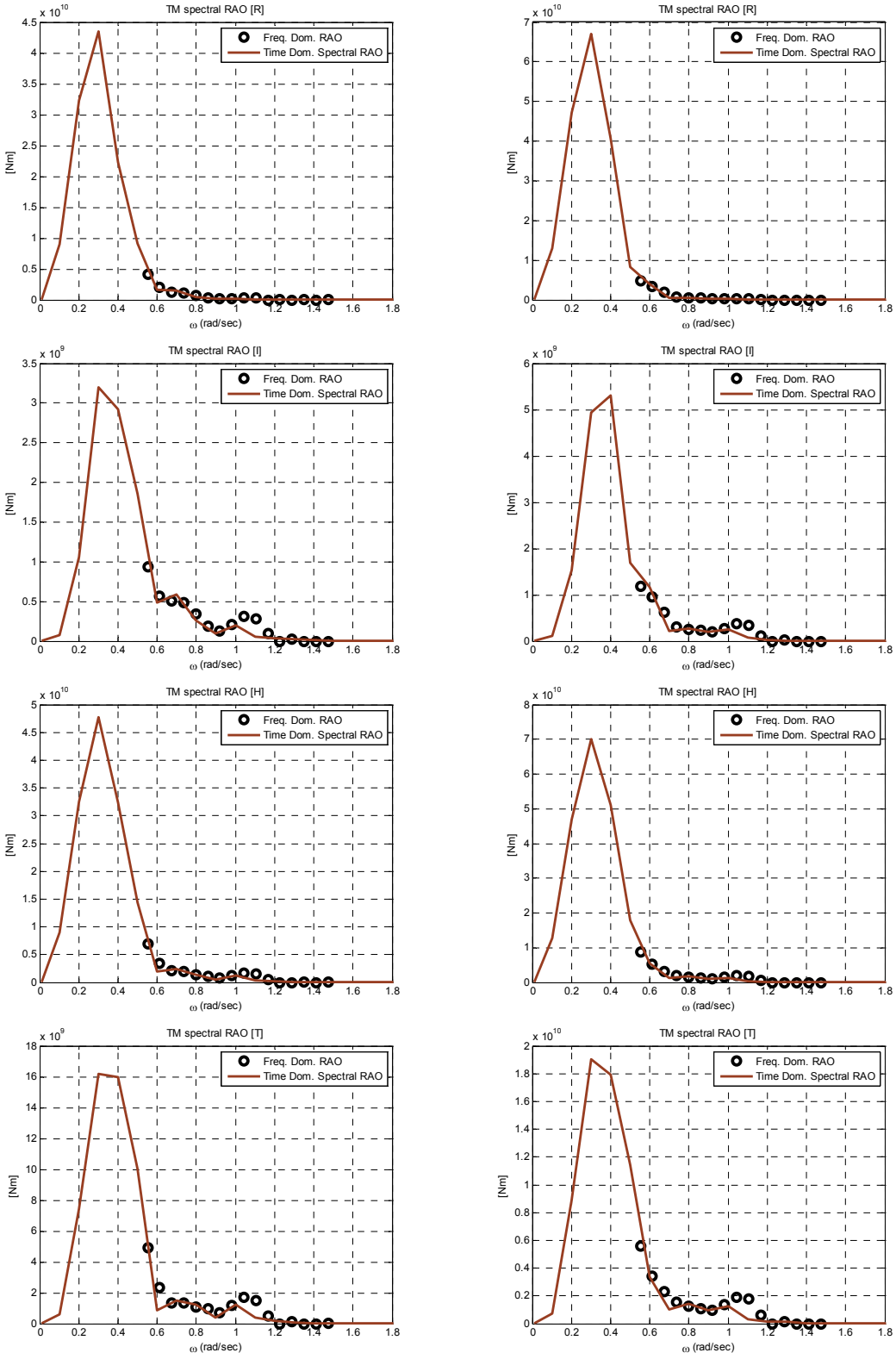

Figure 57. Verification of 3D hydroelastic structural analysis for torsional moments

The shear forces (V) in Figure 55, bending moments (BM) in Figure 56, and torsional moments (TM) in Figure 57 represent the verified results. In each comparison, the left column figures are the stress resultants for the *x* axis and the right column figures are those for the *y* axis. For the respective types of stress resultants, the restoring-induced stress resultants (R), the inertia-induced stress resultants (I), the hydrodynamic pressure-induced stress resultants (H), and the total resultants (T) are compared.

The spectral stress RAOs are calculated within the range where the non-negligible wave energy exists and they show excellent agreements with the frequency domain stress RAOs. The componential correspondence represents that the respective phase effects of componential stress resultants are correctly included in the time domain analysis. The overall well-matched correspondences prove the validity of the 3D hydroelastic structural analysis.

Frequency Domain

The full distributions of shear forces, V(x,y), bending moments, M(x,y), and torsional moments, T(x,y) are given at each incident wave frequency. All the results satisfy the free stress condition at the boundaries. In the low frequency region, the 3D pontoon has the distribution shapes of stress resultants, which are generally induced by the uniform distributed loads, since the long waves relatively to the pontoon length. The maxima occur around the quarter section for the shear forces and mid-section for the bending and torsional moments. From the 0.1 rad/sec in Figure 58, the shear forces and bending moments in the *x* axis are larger than those in the *y* axis, and the torsional

moments have larger magnitudes in the *y* axis than the *x* axis. Up to the 0.1 rad/sec, the bending moments have significant effects from the side walls.

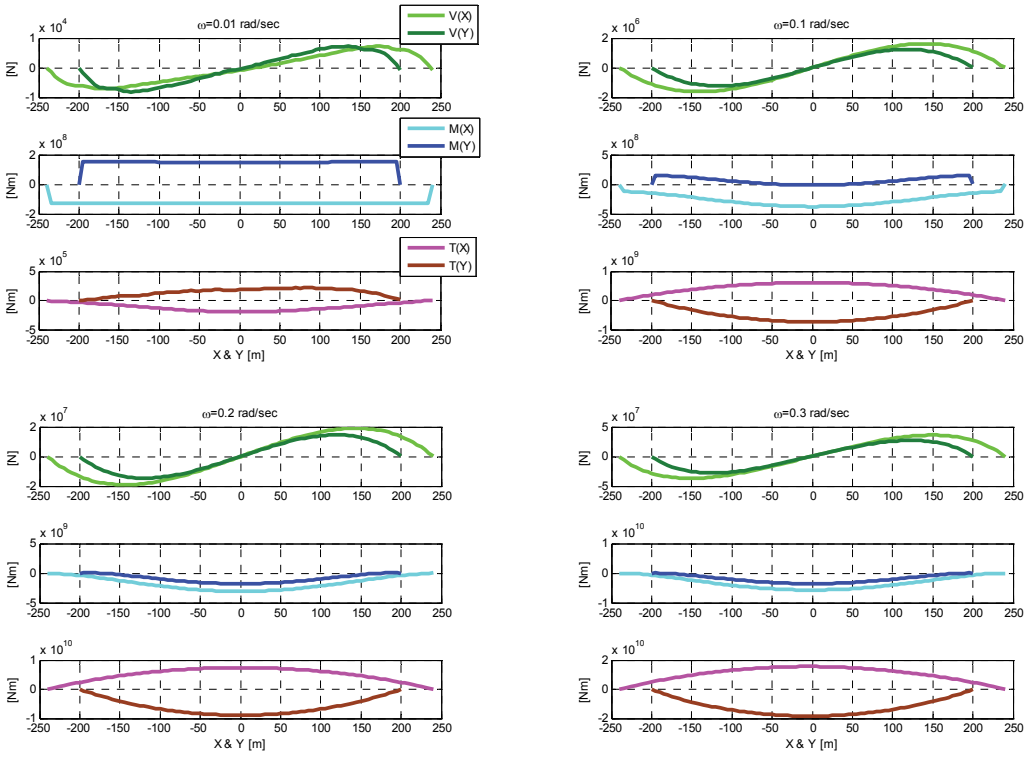

Figure 58. 3D Stress resultants in low frequency region

Starting from the 0.4 rad/sec in Figure 59, the short waves start generating the oscillating distribution shapes. It is not guaranteed to have maxima around the quarter section and mid-section. The distribution shapes of stress resultants are strongly dependent on the wave length.

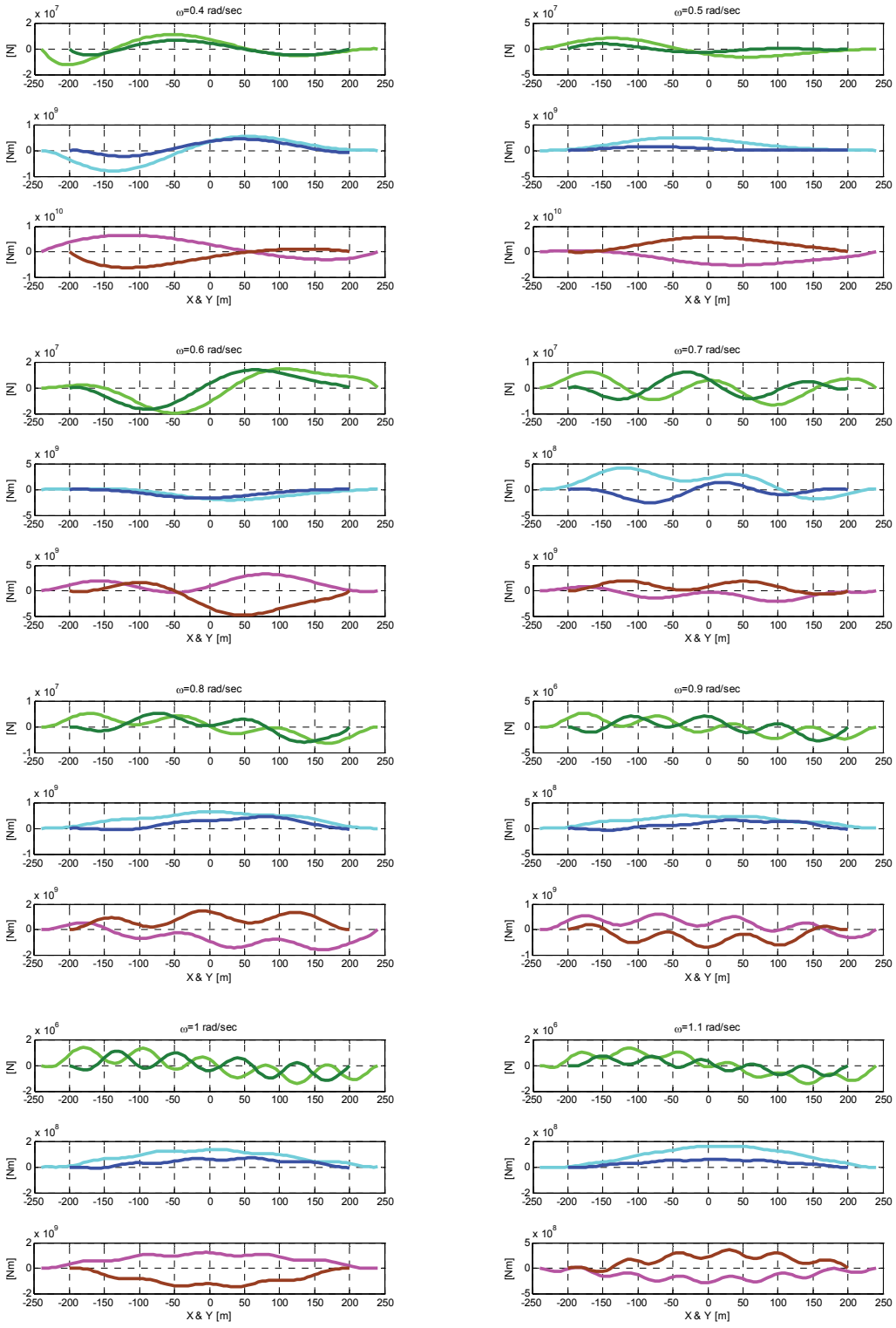

Figure 59. 3D Stress resultants in intermediate frequency region

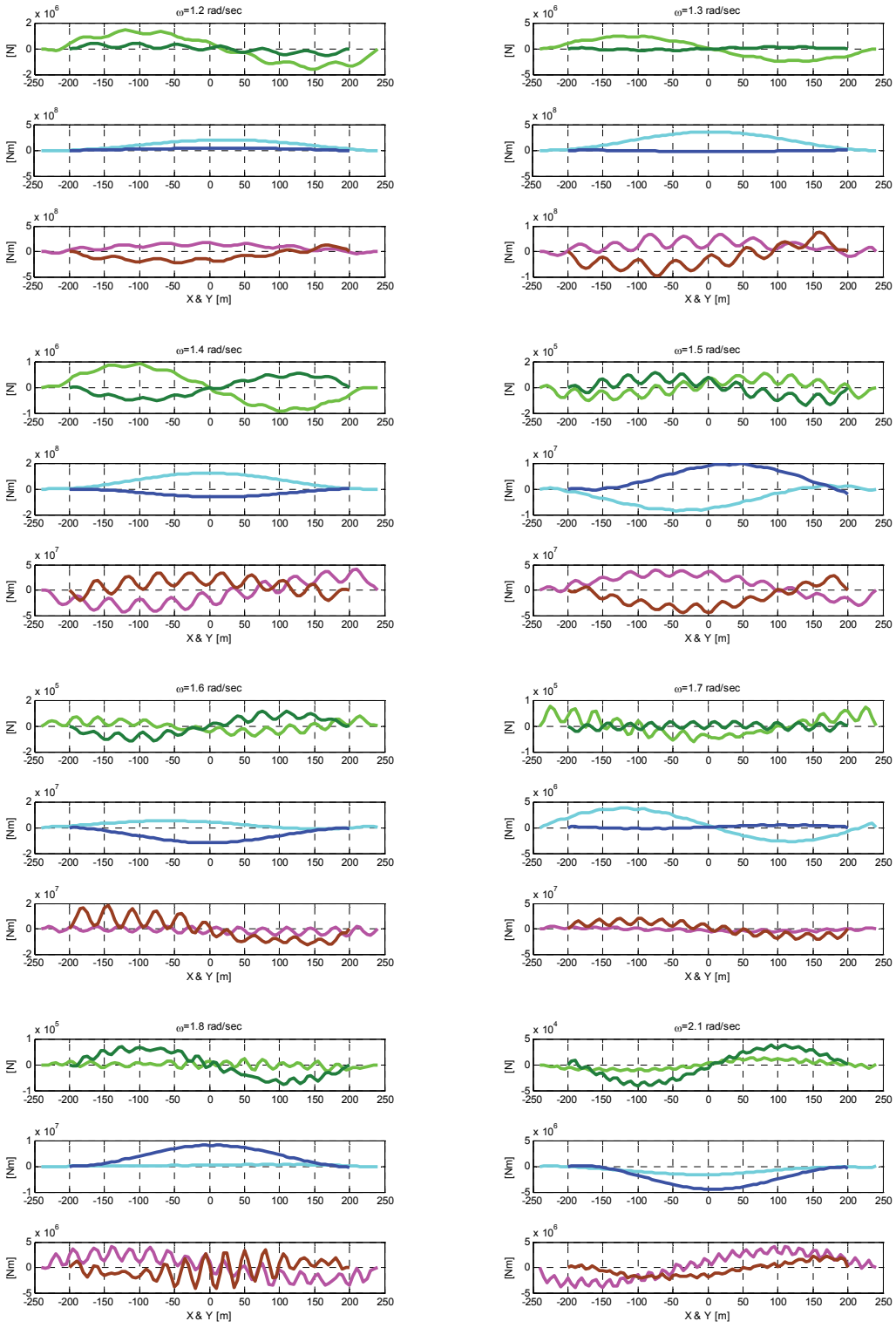

Figure 60. 3D Stress resultants in high frequency region

In the intermediate frequency region, the share forces and torsional moments have the more active oscillation of the distribution shapes for the shorter waves. Moreover, the variations have high frequency components simultaneously with the slowly varying oscillations. The bending moments are larger in the *x* axis than the *y* axis.

In the high frequency region over the 1.1 rad/sec shown in Figure 60, the shear forces and torsional moments have strong oscillations, whereas the bending moments have dominant slow-varying tendency. The high frequency oscillations are proportional to the wave frequency. The shorter waves induce more oscillations of the stress resultants in the same length.

The maxima at each frequency are collected in Figure 61, and the respective components at the maxima are compared in Figure 62. The maxima are taken from the magnitudes of the complex stress resultants.

The maxima of the stress resultants are dominant up to the 1 rad/sec from 0.1 rad/sec. The shear forces and bending moments have resonance peaks induced by the second elastic mode, which is pure bending deformation. Meanwhile, the torsional moments have the first elastic mode resonance, which is the torsional deformation. The correlation of the resonances and peaks in the maxima are mainly due to the geometric similarity to the definitions of stress resultants.

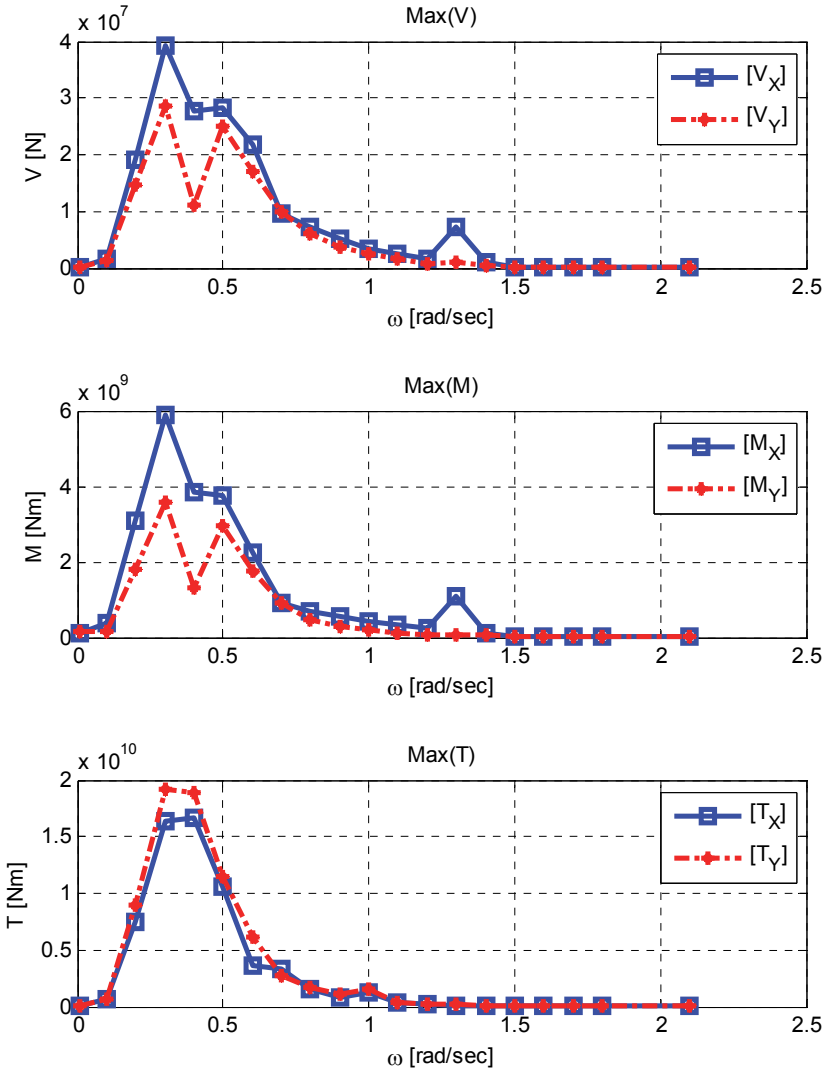

Figure 61. Maxima of stress resultants at each frequency

In Figure 62, T stands for the total, H means hydrodynamic pressure effects, I is for the inertia effects, and the R means restoring effects. From the componential comparisons of the maxima stress resultants, it turns out that the 3D stress resultants are heavily induced by the hydrodynamic pressures and restoring loading. The minor effect

from the inertia loading is because of the non-resonance dynamics in the low and intermediate frequency region.

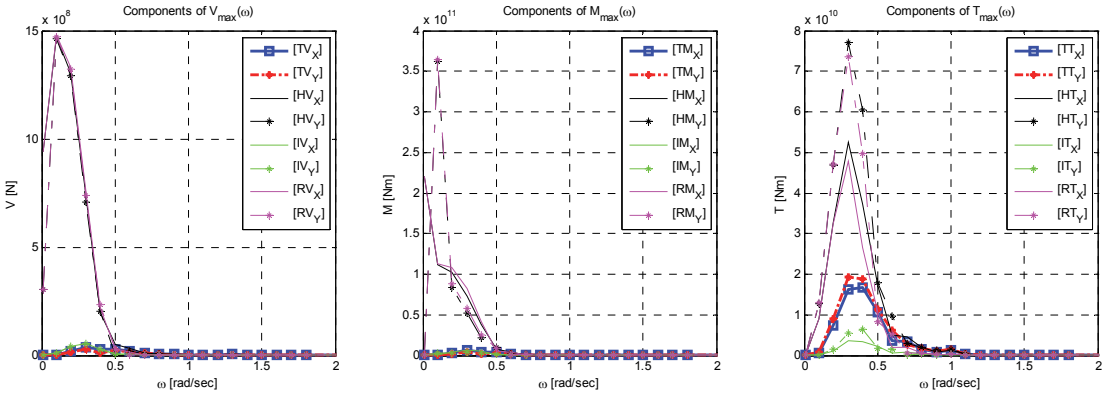

Figure 62. Componential comparison of the maxima 3D stress resultants

Time Domain

The time-domain 3D hydroelastic structural analysis is carried out for the sea state 5. The random sea-induced stress resultants are achieved as functions of space and time for shear forces, bending moments, and torsional moments with respect to the *x* and *y* axes. The irregular stress resultants are compared against counterparts in the frequency domain by the spectral stress resultants RAOs and show excellent agreements as given in Figure 55, Figure 56, and Figure 57. For the random sea of sea state 5 with main wave energy from 0.4 to 1.4 rad/sec, the stress resultants are investigated comprehensively.

From the oblique waves proceeding from positive *x* and *y* axes, in Figure 63 the shear forces are larger in the negative *x* and *y* axes, bending moments are mainly distributed in the center area, and torsional moments are larger in the positive side. In

comparison of *x* and *y* axes, the shear forces and bending moments are larger in the *x* axis than the *y* axis, while the torsional moments have the larger maxima in the *y* axis.

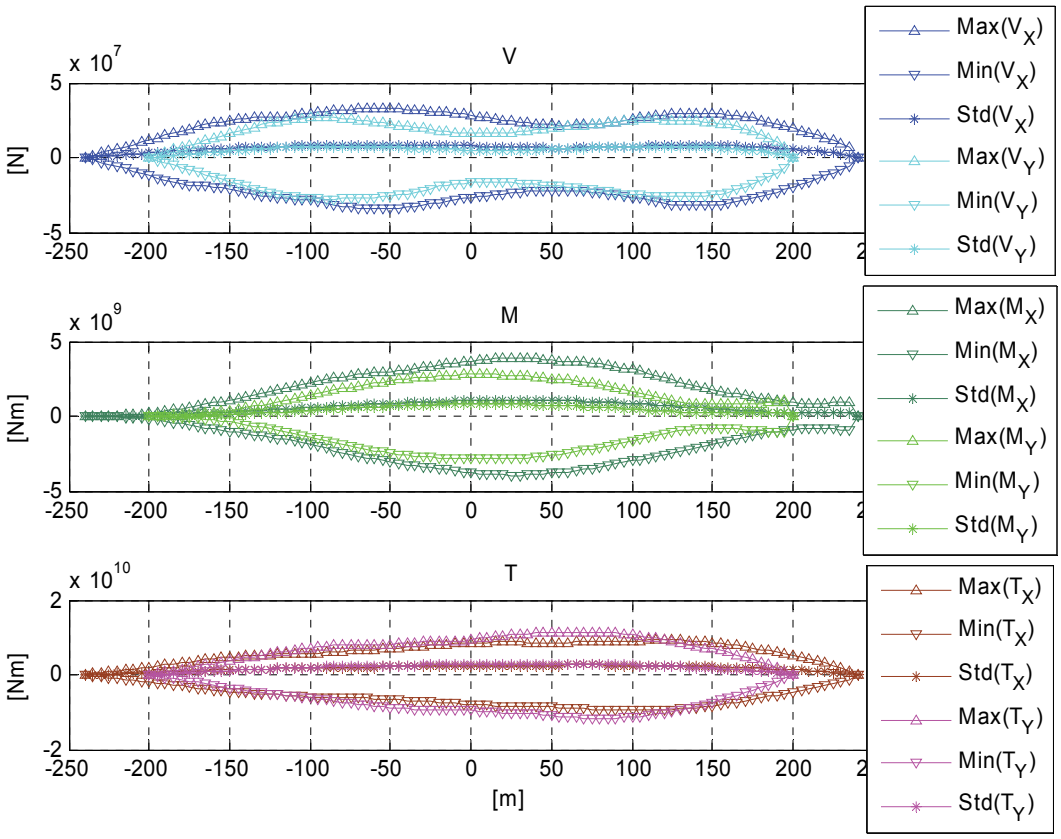

Figure 63. Statistical distributions of stress resultants for 3D pontoon

Based on the statistical distributions of stress resultants, the irregular stress resultants are investigated in more detail at specific points. The shear forces are measured at *x*=−50 m, y=−100 m, bending moments are studies at the *x*=25 m, y=10 m, and torsional moments are given at the *x*=125 m, y=70 m, where the largest maxima occur.

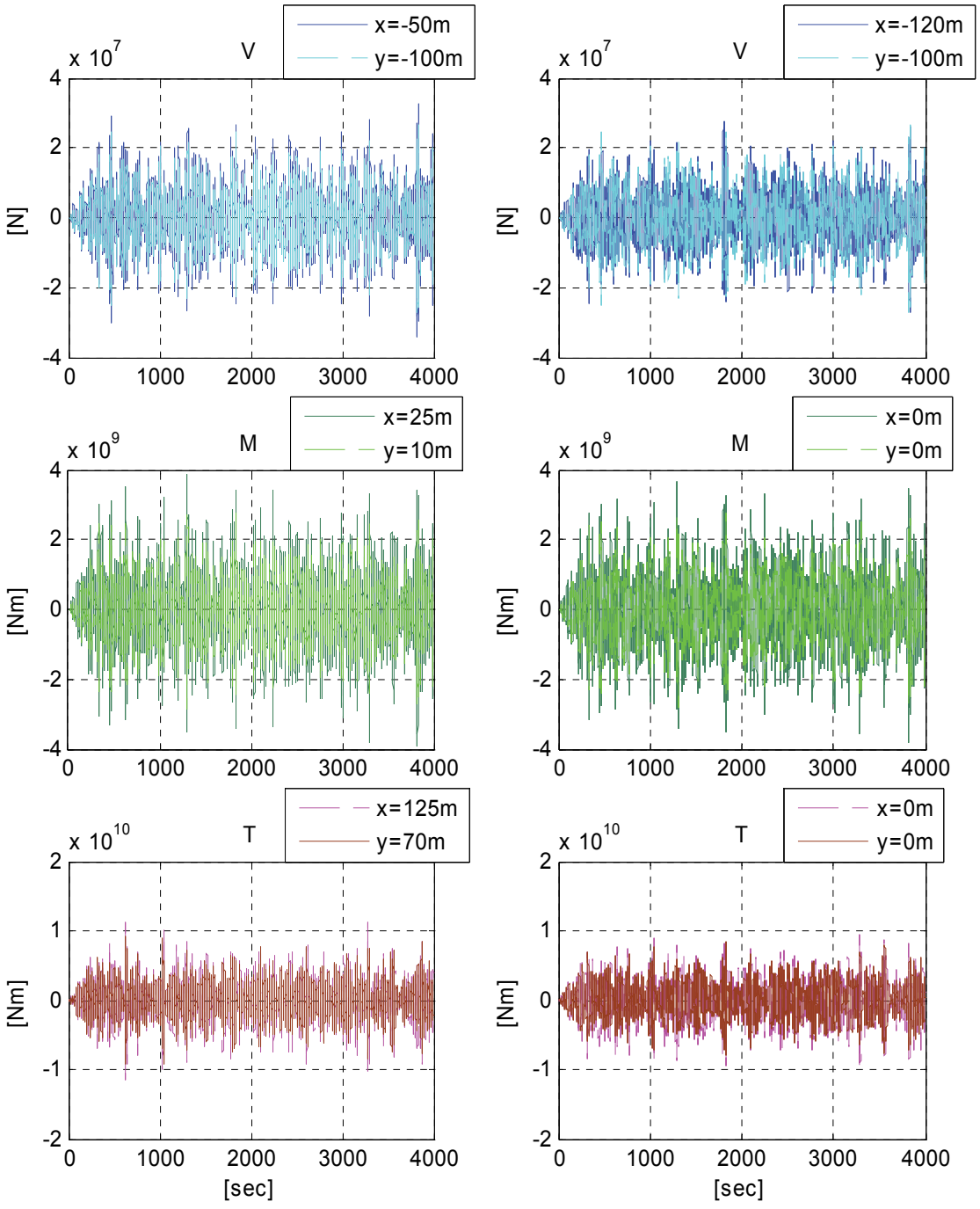

Figure 64. Stress resultants time series at maxima occurrences and quarter, mid-sections for 3D pontoon

In addition, they are copared with the results at the quarter section for shear forces and mid-section for bending and torsional moments. The stress resultants at the maxima occurrences are in overall larger than those at the quarter and mid-sections.

Similarly to the statistical investigation, the irregular stress resultant time serieses in Figure 64 show that the shear forces and bending moments are more intensive in the *x* axis, and the torsional moments are more concentrated in the *y* axis, although the amplitudes are same order of scale in both directions. Reminding of directions of respective stress resultants, the *x* axis motions such as surge and pitch induce more stresses than the *y* axis. Such a tendency can be dependent on the geometric shape of the floating body, wave headings, and deformation functions. Furthermore, the detail local structural analyses or fatigue life estimations are applicable by adopting all the clarified 3D stress resultants.

Hydroelastic Analysis Coupled with Mooring-Riser

In the present coupled hydroelasticity study, two sets of mooring systems are considered. To identify influences of the mooring line interactions, one taut and one slack mooring systems are modeled as Figure 65. Water depth is assumed to be 600 m and oblique waves are applied.

The taut mooring system is intended to realize strong interactions between the floating body deformation and mooring lines, whereas the slack mooring system represents the weak interactions as summarized in terms of particulars in Table 7.

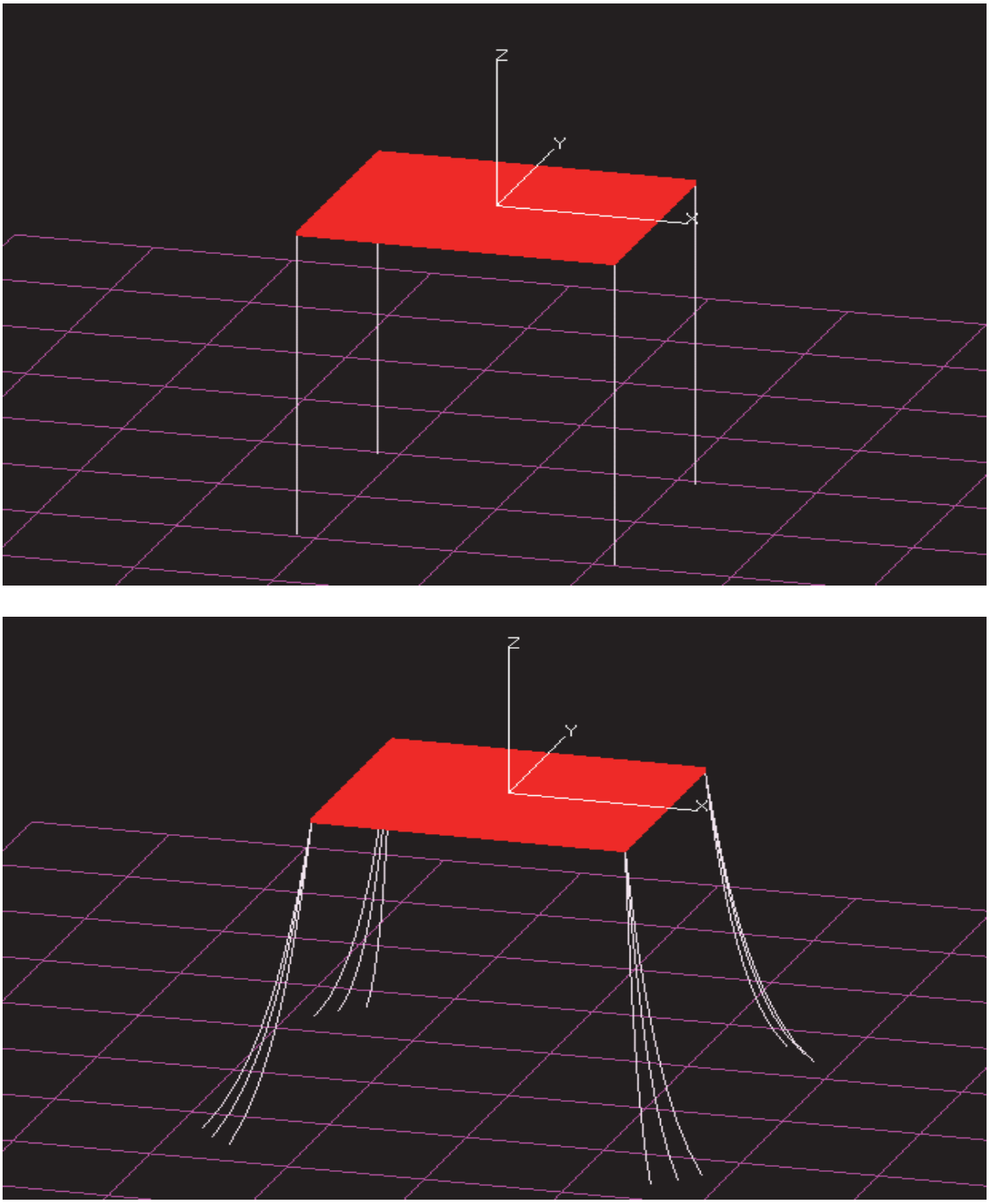

Figure 65. Schematic view of 2 mooring systems for 3D pontoon

Table 7. Particulars of two mooring systems

	Taut mooring system	Slack mooring system
Line length	595 m	620 m
Wet weight, Dry weight	24.79, 29.01 kg/m	24.79, 29.01 kg/m
Axial stiffness (EA)	8.45837E+10 N	3.53337E+08 N
Bending stiffness (EI)	6.54742E+07 Nm^2	1.37824E+05 Nm^2
Diameter	0.079 m	0.079 m
Ca, Cd	1, 1.5	1, 1.5
Number of mooring lines	4	12

Dynamic Motion Responses

In Figure 66, the coupled dynamic motions responses are compared with the freely floating case in order to investigate interaction effects between mooring lines and floating body deformation.

Not only in the rigid modes but also in the elastic modes, the interaction effects of the mooring system into the floating body deformations are not significant in the slack mooring case. For the taut mooring system, the deformations are heavily excited by the mooring tensions in all the elastic modes. Contrary to the freely floating condition, the taut mooring system signifies the first order twist elastic mode.

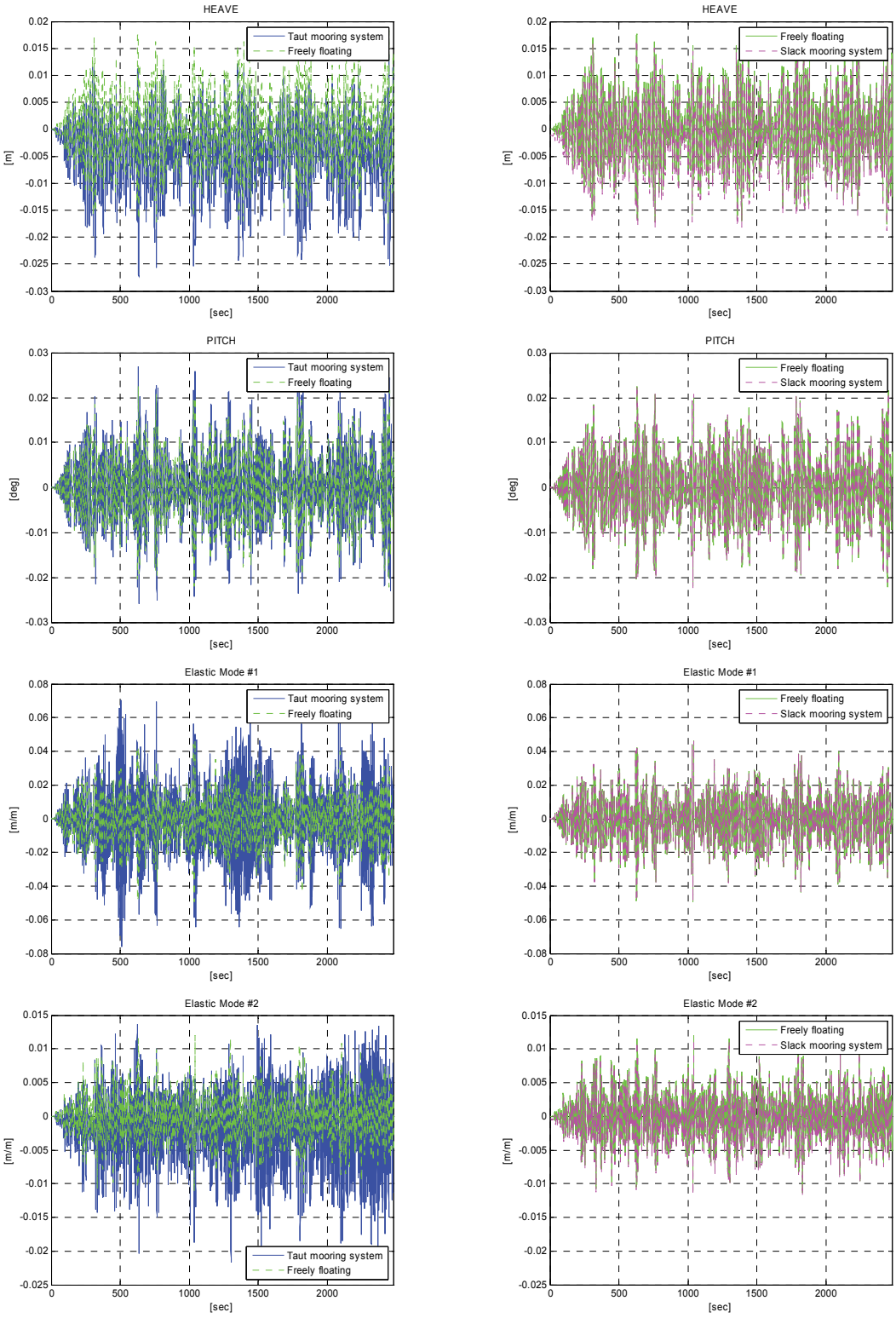

Figure 66. Comparison of hydroelastic dynamic responses for taut and slack mooring systems

Therefore, it can be concluded that the more taut mooring system involves the more noticeable interactions with the floating body deformation and it would entails the aggravation of fatigue life.

Dynamic Stress Resultants

Based on the significant interactions between the mooring lines and floating body deformations, the taut mooring system is investigated further by the coupled 3D hydroelastic structural analysis.

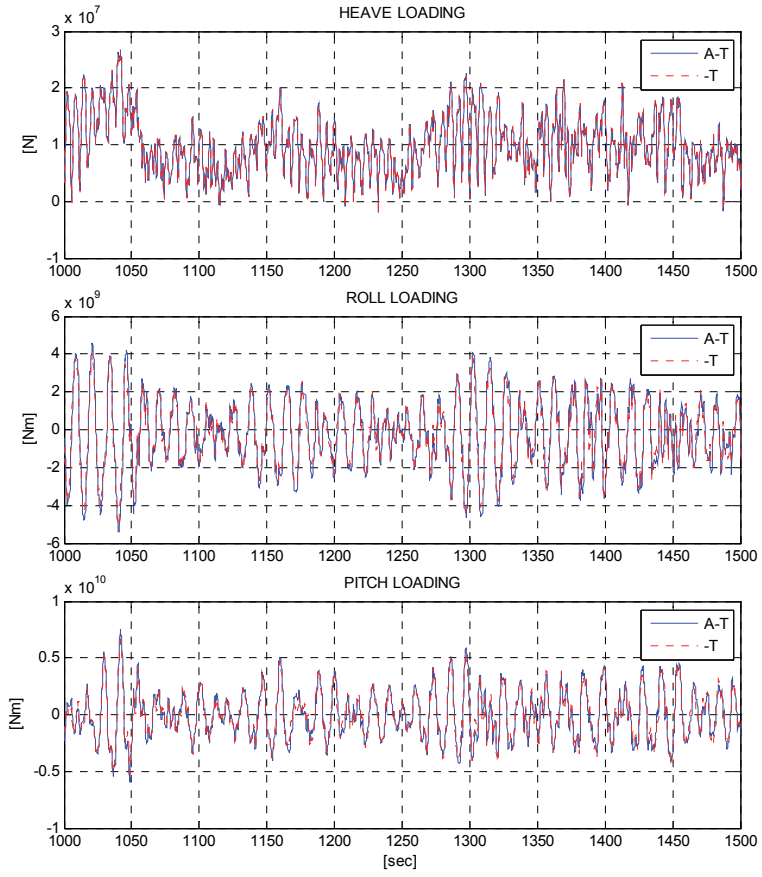

Figure 67. Verification of equilibrium for coupled 3D hydroelastic analysis

As prerequisite for the verifications, the equilibrium of the coupled 3D hydroelastic dynamic analysis is checked in Figure 67 and shows excellent agreements cross the whole simulation time and all of the modes. The satisfactory equilibrium ensures the more accurate dynamic stress resultants since it represents all the loads acting on the moored 3D deformable body are correctly identified.

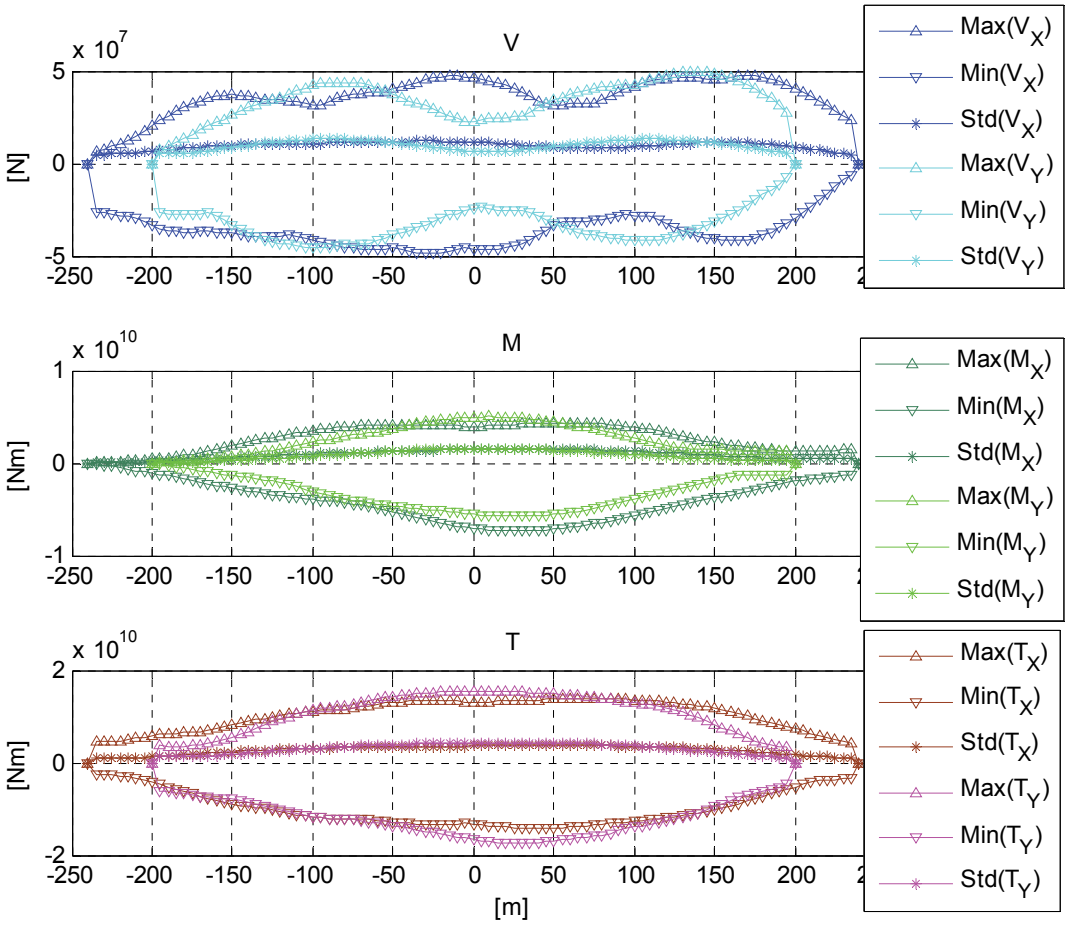

Figure 68. Statistical distributions of stress resultants for moored 3D pontoon

The statistical distributions of dynamic stress resultants for the moored 3D flexible pontoon in Figure 68 represent that the mooring interactions induce larger stress resultants overall. At both ends, the step-wise stress resultants are generated by the mooring tensions and they directly increase a level of scale.

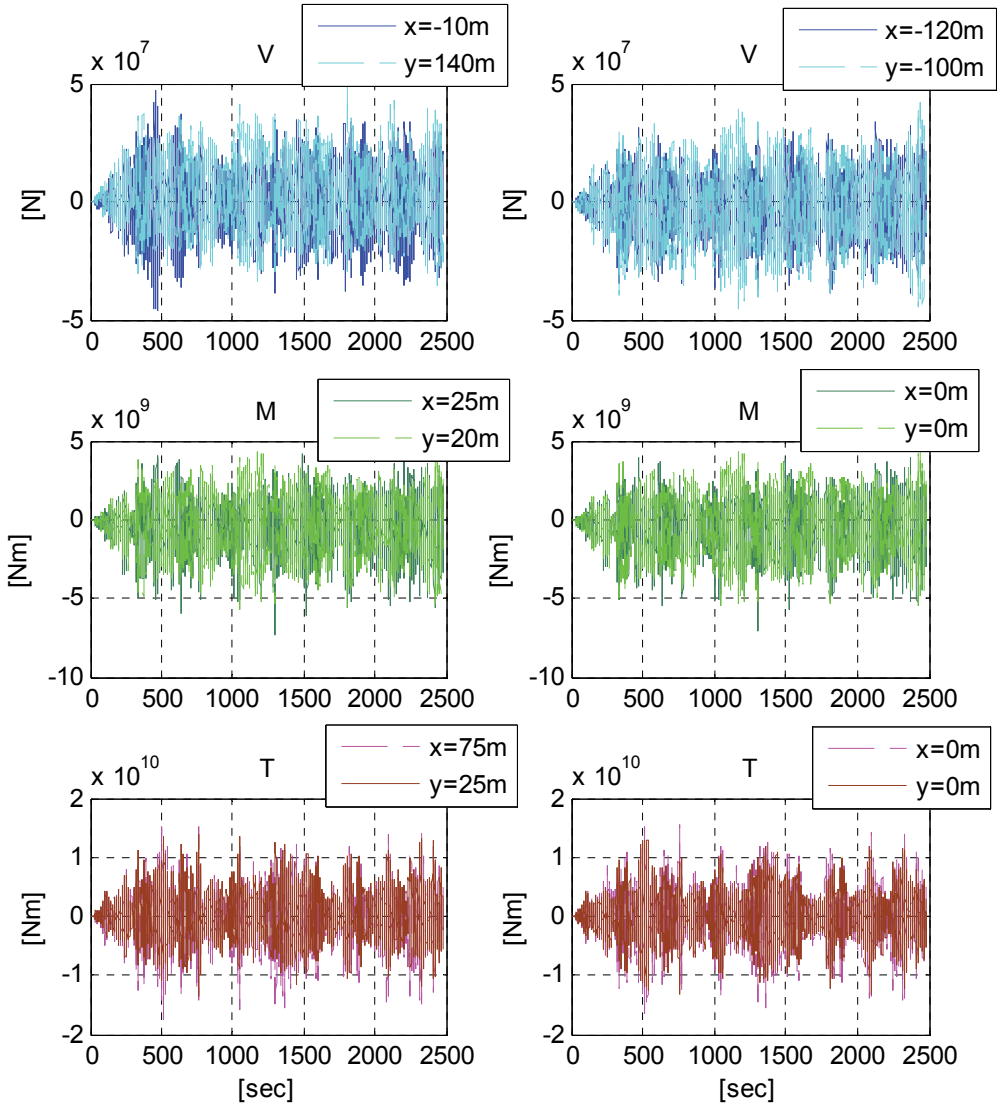

Figure 69. Stress resultants time series at maxima occurrences and quarter, mid-sections for 3D moored pontoon

Across the surface, the maxima occur at x=-10 m, y=140 m for shear forces, x=25 m, y=20 m for bending moments, and x=75 m, y=25 m for torsional moments. As an example, the time series of the dynamic stress resultants are shown in Figure 69.

The stress resultants at quarter section for shear forces and mid-section for bending and torsional moments are compared between the moored case and freely floating case in Figure 70.

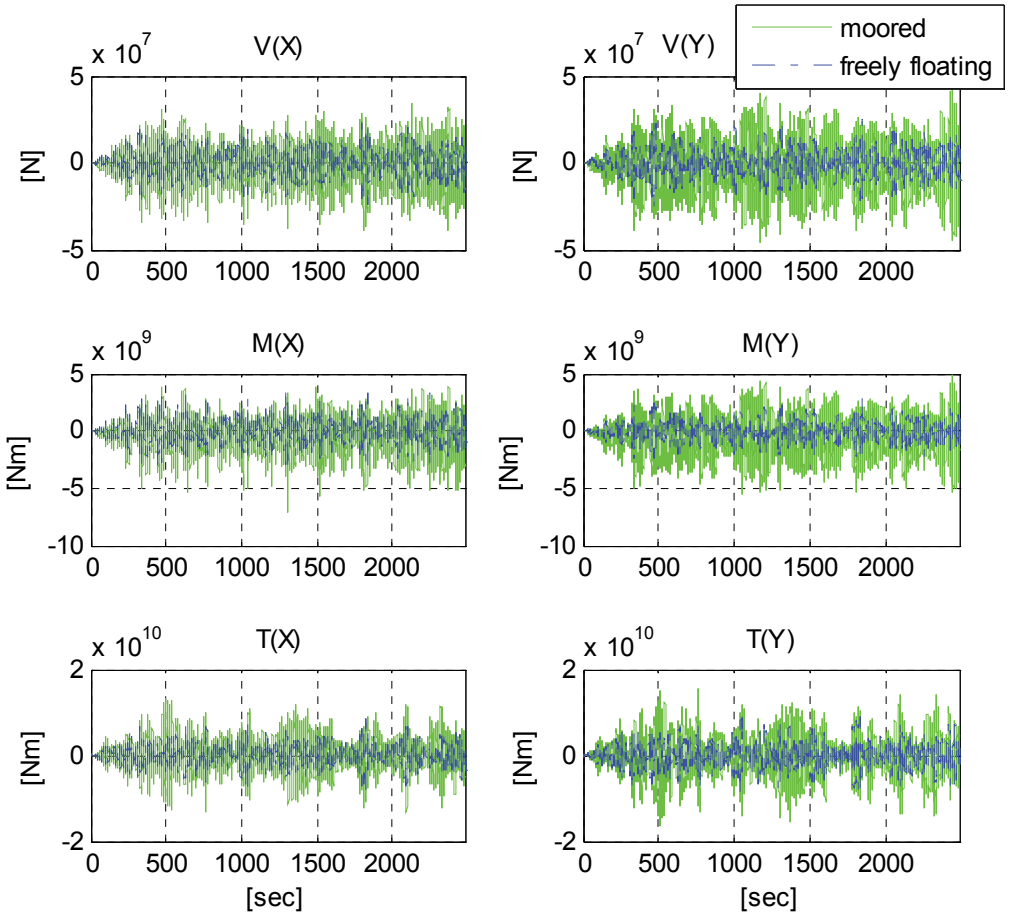

Figure 70. Stress resultants comparison between moored condition and freely floating condition for 3D pontoon

It is clearly seen that the mooring interactions significantly influence overall stress resultant distributions and the tension increases the magnitudes. Furthermore, the components are compared for respective types of stress resultants in Figure 71 for shear forces, in Figure 72 for bending moments, and in Figure 73 for torsional moments. As identified in the componential comparison in the frequency domain, the inertia effects are insignificant, whereas the hydrodynamic pressure-induced stress resultants have similar magnitude scale to the restoring-induced stress resultants.

The moored case has overall large maximum magnitudes in the componential comparisons than those for the freely floating case. The hydrodynamic effects include the convolution terms which are functions of velocities in addition to the pure diffraction pressures. Therefore, the increases of stress resultants in the moored case can be explained by the mooring tension-induced excitation toward the floating body dynamics, which is consistent to the larger motions in the moored case, especially in the elastic modes. That is the mooring interactions induce more active motions to the moored deformable body and the larger motions entail the increased stress resultants especially in terms of the displacements and velocities.

Moreover, the moored case has additional components from the mooring tension, and it can be regarded as direct addition to the stress resultants. In the relative scale, the mooring tensions generate one of main component stress resultants along with the restoring and hydrodynamic effects.

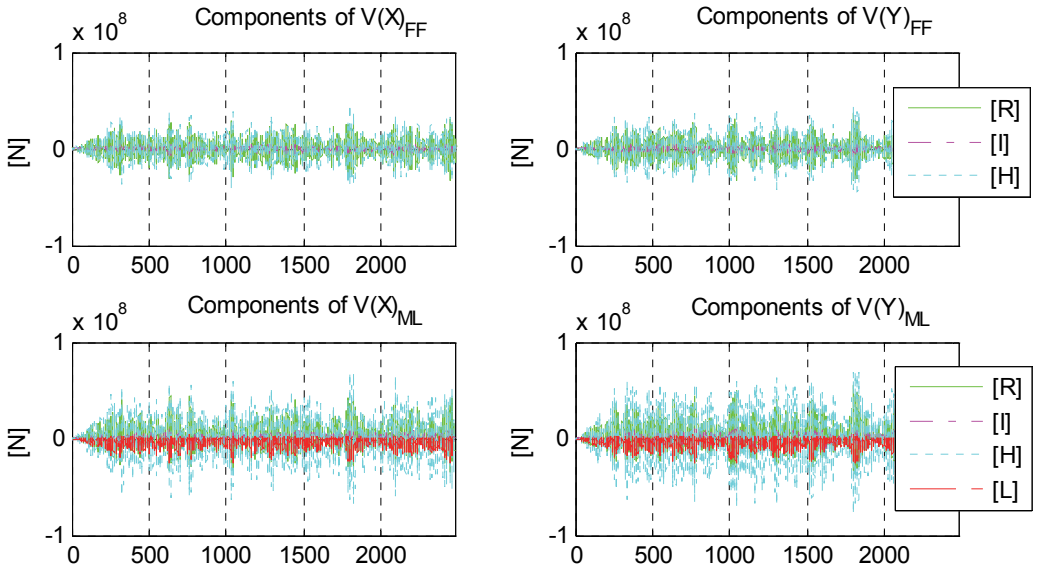

Figure 71. Componential comparison of 3D pontoon shear forces: moored vs. freely floating

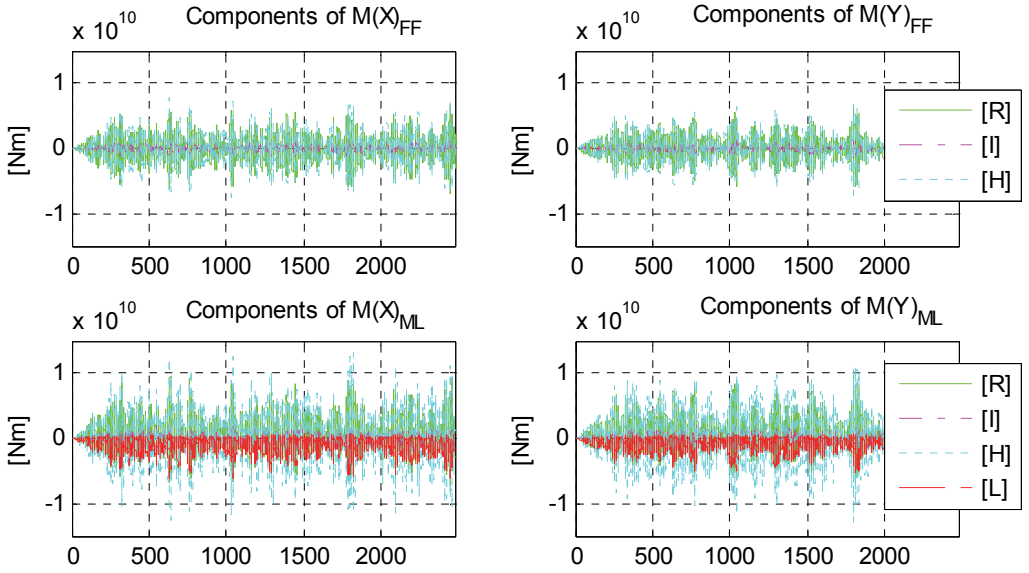

Figure 72. Componential comparison of 3D pontoon bending moments: moored vs. freely floating

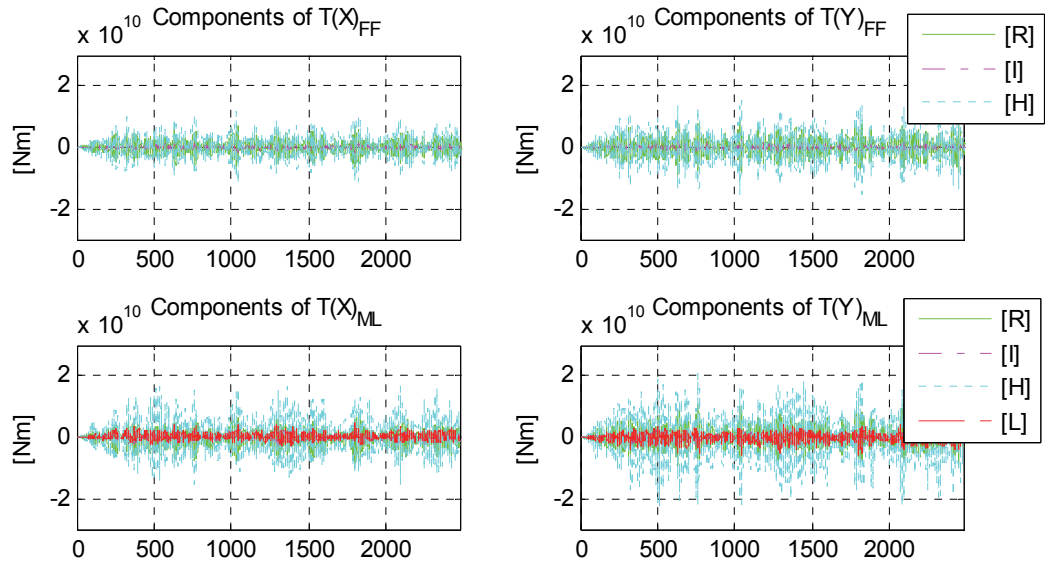

Figure 73. Componential comparison of 3D pontoon torsional moments: moored vs. freely floating

The fully coupled 3D hydroelastic structural analysis for the moored deformable body clearly represents interactions between dynamics of the deformable floating body and nonlinear mooring lines. The developed methodology can be used for more accurate stress resultants and more realistic fatigue analysis, including the coupled nonlinear mooring-riser dynamics.

Simplified 2nd Order Time Domain Analysis

The second order wave loads for the sum and difference frequencies are added into the 3D pontoon along with the hydroelastic dynamic analysis for the random seas. The random oblique waves of sea state 5 are applied including the simplified 2nd order loads.

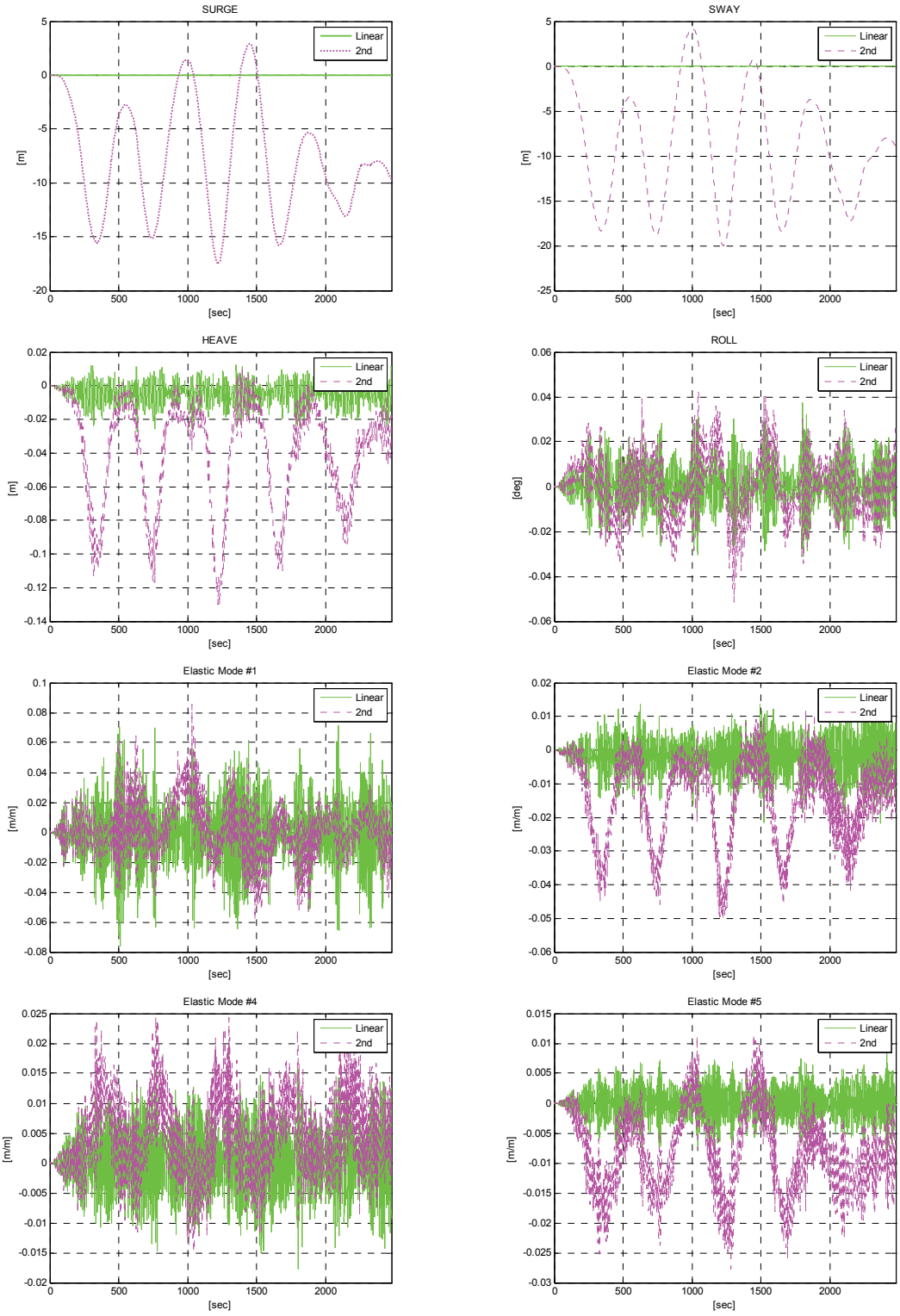

Figure 74. Time responses of 3D pontoon including 2nd order wave loads

As shown in Figure 74, the slowly varying motions in horizontal modes interact with heave and elastic deformation modes. The non-twisting elastic modes have significant interactions with the low frequency excitations which are induced by the sum-frequency waves. The twisting elastic modes have low-frequency motions corresponding to the roll and pitch motions. Moreover, there exist strong coupling effects among the twisting elastic modes or non-twisting elastic modes, respectively.

The high-frequency components as well as the low-frequency components signify the hydroelastic dynamic responses.

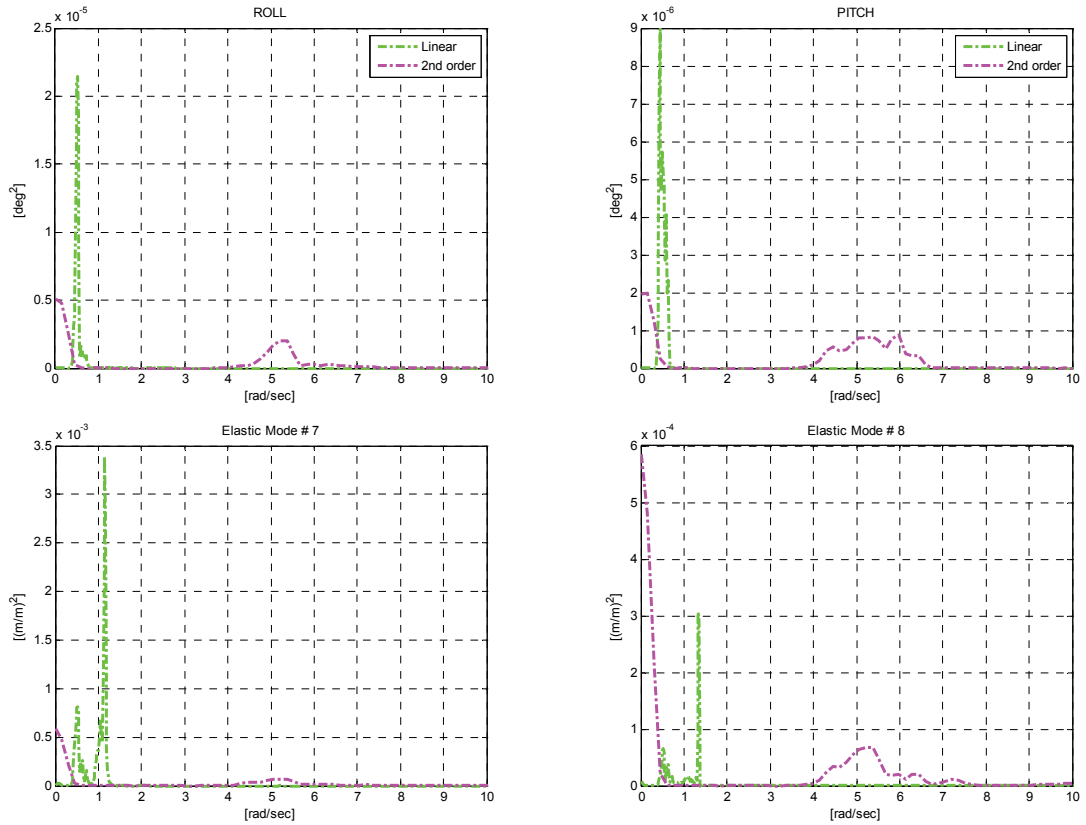

Figure 75. Elastic response spectra of 3D pontoon including 2nd order wave loads

Especially in roll and pitch motions, the high-frequency oscillations occur around 5 rad/sec and it subsequently influences the elastic deformations as given in Figure 75.

In comparison of response spectra between the linear and 2nd order cases, it is clearly seen that two main components of responses. The low frequencies are mainly induced by the horizontal motions such as surge, sway, and yaw, whereas the high frequencies are excitations driven by the roll and pitch motions.

As demonstrated by the set-down effect, the low-frequency horizontal motions induce significant tensions to the taut mooring system with slow variations as Figure 76.

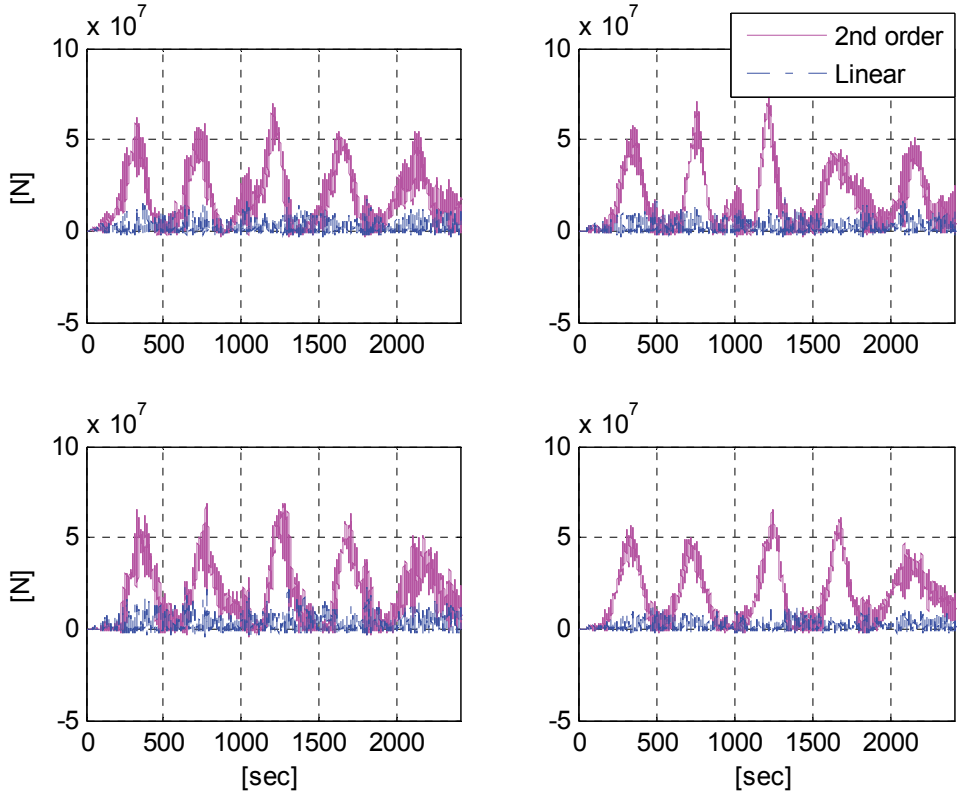

Figure 76. Tension comparison of mooring system for 3D pontoon between linear order and 2nd order

8. NUMERICAL SIMULATION OF HIGH ACCURACY DYNAMIC POSITIONING SYSTEM

The high accuracy of DP control is designed for the offshore float-over installation in order to achieve 1 or 2 m watch circles at the launching point. The optimum DP control consists of Kalman filter and PD feedback control. And the general allocation scheme is utilized to assure the least time lag until the counter loads generated. Due to the confidentiality, an alternative case study is chosen from the 3D pontoon analysis instead of the float-over example. With the high accuracy DP control achieved for the freely floating condition, the developed numerical DP tool is extended further to the mooring-riser coupled analysis.

High Accuracy DP System

Assuming the 3D pontoon is freely floating in the real ocean waves only with the DP control active, the optimal DP system is designed and the resultant dynamic responses and thrust loads are investigated. To realize the ocean waves, the second order wave loads for the difference frequency are included by Newman's approximation, and the Morison damping plates are adopted to account for energy dissipation induced by the viscous effects of ocean waves. With the projected area, the damping coefficient is assumed as 2. To implement the random sea test, the sea state 5 is adopted.

Optimal Kalman Filtering

To take the optimal states into the feedback control, Kalman filter is customized. In the two sets of noise parameters, the process noise parameters are estimated from the

linear wave excitation spectra corresponding to the sea state 5. With the process noise parameters automatically calculated, the measurement noise parameters are further tuned as given in Table 8 to extract the optimal slowly-varying motion responses.

Table 8. Estimated noise parameters

	SURGE	SWAY	YAW
Process noise (w)	1.849E+6	1.721E+6	7.286E+8
Measurement noise (υ)	5.0E−3	5.0E−3	1.0E−2

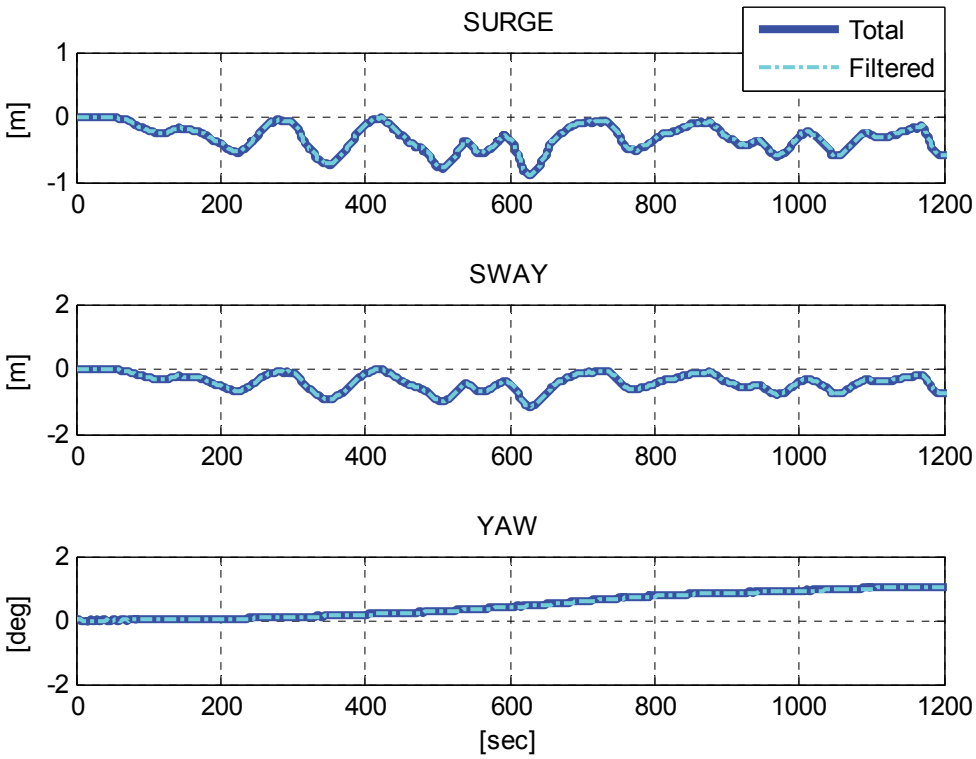

Figure 77. Filtered displacements of 3D pontoon with freely floating condition

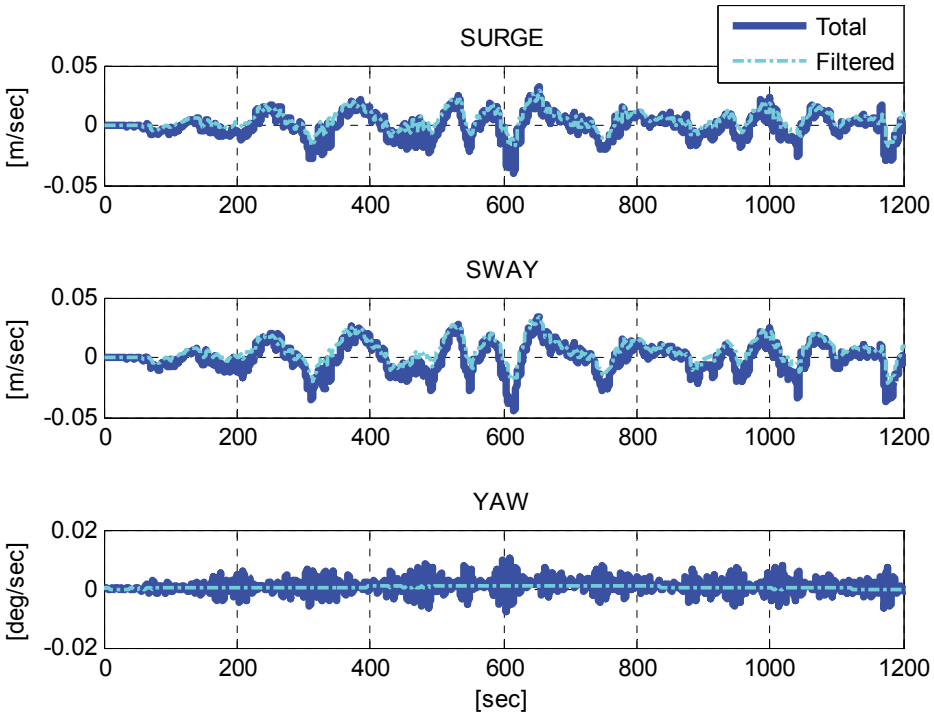

Figure 78. Filtered velocities of 3D pontoon with freely floating condition

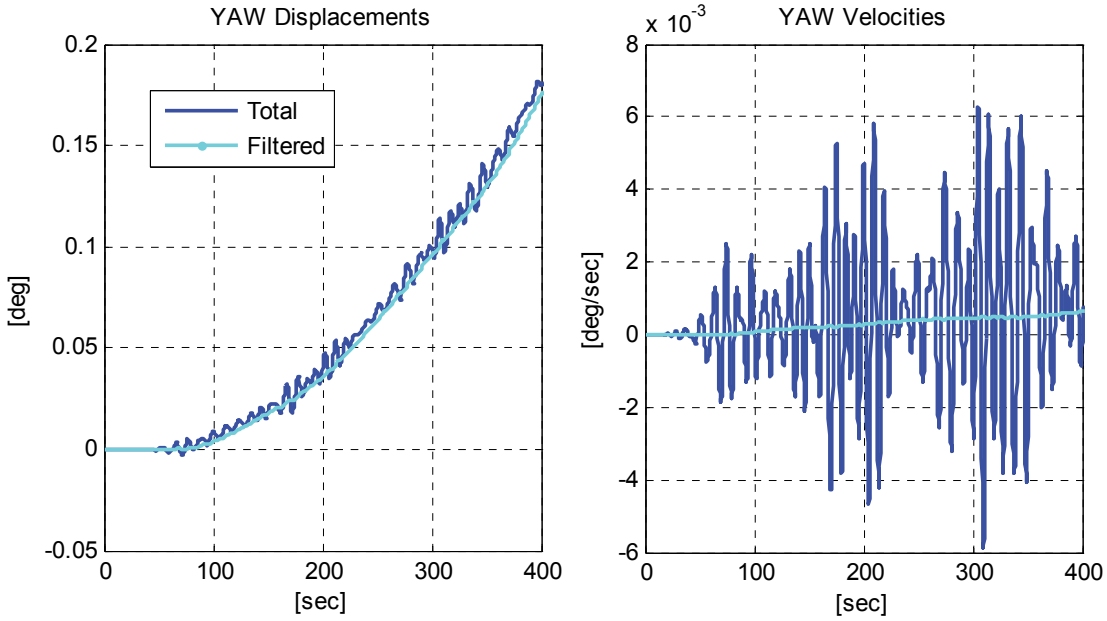

Figure 79. Enlarged yaw responses after Kalman filtering

The filtered displacements in Figure 77 and velocities in Figure 78 clearly show removal of the high frequency responses. As an example, the yaw motion can be regarded as the most desirable Kalman filter resultants in that the low frequency motions are clearly captured as demonstrated. The filtered responses exclude the high frequency oscillations as demonstrated in Figure 79. From the total responses, it turn out that the 3D pontoon with DP system achieves the watch circle 2 m in the sea state 5 random sea condition.

Optimal PD Control

With the responses filtered, the feedback loads are estimated from the optimal PD gains. The optimal PD gains are results from solving the Riccati equation given by the performance function. The performance function is defined by coefficients in the matrices, O and N. The larger numbers in the matrix O implies the more sensitive reaction loads, which means the larger PD gains are created to induce the larger counteracting loads. The larger numbers in the N enhance fuel efficiency and thus the PD gains are reduced.

The resultants PD gains are the unique and optimal feedback gain for the given performance function. Therefore, it is important to identify the effective scale of the elements in the O and N matrices.

Considering the dimension of the floating body and severe sea state, the matrices are defined as

$$O=\begin{bmatrix} 1\mathrm{E}+5 & 0 & 0 & 0 & 0 & 0 \\ 0 & 1\mathrm{E}+13 & 0 & 0 & 0 & 0 \\ 0 & 0 & 1\mathrm{E}+5 & 0 & 0 & 0 \\ 0 & 0 & 0 & 1\mathrm{E}+13 & 0 & 0 \\ 0 & 0 & 0 & 0 & 1\mathrm{E}+8 & 0 \\ 0 & 0 & 0 & 0 & 0 & 1\mathrm{E}+16 \end{bmatrix}, \quad (71)$$

$$N=\begin{bmatrix} 0.1 & 0 & 0 \\ 0 & 0.1 & 0 \\ 0 & 0 & 0.001 \end{bmatrix}.$$

The small scale of the N represents that the high accuracy is the top priority regardless of the fuel efficiency. Such the high accuracy DP system is feasible and advantageous for the offshore float-over installation, which normally requires the short period of operating time.

Subsequently, the optimal PD gains are calculated from the given Riccati equation as

$$G=\begin{bmatrix} 1.8\mathrm{E}+8 & 1.0\mathrm{E}+7 & 0 & 0 & 0 & 0 \\ 0 & 0 & 1.8\mathrm{E}+8 & 1.0\mathrm{E}+7 & 4.4\mathrm{E}+1 & -2.6\mathrm{E}+0 \\ 0 & 0 & 9.3\mathrm{E}+1 & 2.6\mathrm{E}-1 & 3.2\mathrm{E}+11 & 1.0\mathrm{E}+9 \end{bmatrix}. \quad (72)$$

The feedback forces and moments for surge, sway, and yaw are given in Figure 80. Based on the large scale of the system, the feedback loads are in large scales. The maxima occur after 600 sec where the largest offsets in surge and sway take place. In frequency wise, the feedback loads have minor high frequency oscillation due to the well-defined Kalman filtering scheme.

The total feedback loads are distributed into individual thrusters and they generate counteracting loads.

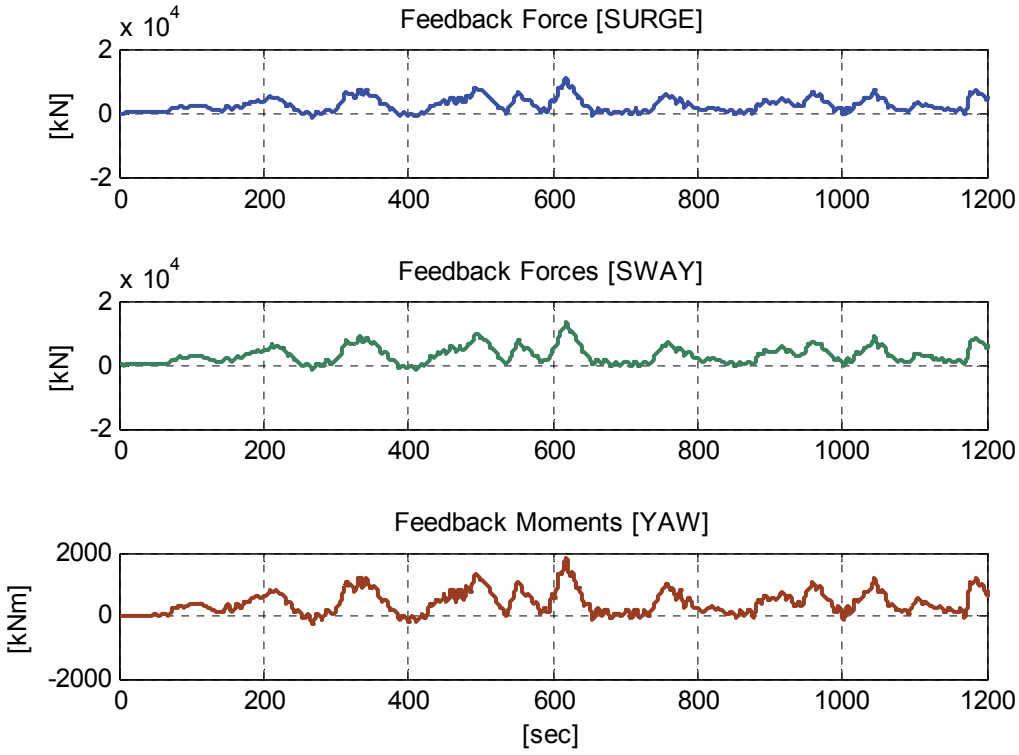

Figure 80. Feedback loads of 3D pontoon with DP only

Generalized Thrust Allocation

In this study, the thruster system is assumed to have 4 azimuths thrusters and 2 fixed thrusters. The azimuth type is marked as a blue circle and the fixed type is given as a red triangle in Figure 81. The given arrangement of thrusters forms the matrix D as

$$D = \begin{bmatrix} 1 & 0 & 1 & 0 & 1 & 0 & 1 & 0 & 1 & 1 \\ 0 & 1 & 0 & 1 & 0 & 1 & 0 & 1 & 0 & 0 \\ -190 & 230 & -190 & -230 & 190 & -230 & 190 & 230 & -100 & 100 \end{bmatrix}. \quad (73)$$

The first 8 columns represent the 4 azimuth thrusters and the last 2 columns are the fixed thrusters in the *x* axis. The Pseudo-inverse matrix enables the generalized thrust allocation.

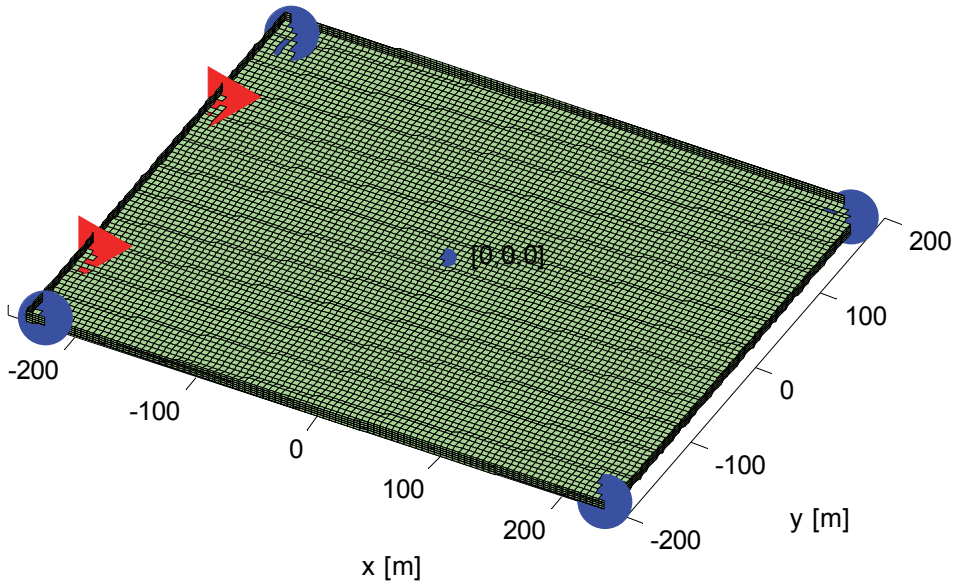

Figure 81. Schematic view of thruster system

Allocated thrust force records in Figure 82 show that each azimuth thruster with the maximum capacity of 4MN would be indispensable to achieve 2 m watch circle. The fixed thrusters have the half maximum thrust loading. The maximum thruster loading occurs at the largest offset within the negligible time lag. Respective azimuth thrusters occur with the azimuth angles in time series. As an example, the first thruster's azimuth angle is investigated. The azimuth angle is defined as direction of the thruster forces from 0 degree to 360 degree. And each thruster is set to activate once the required thrust is over 1 KN to avoid meaningless wear and tear of the thruster system.

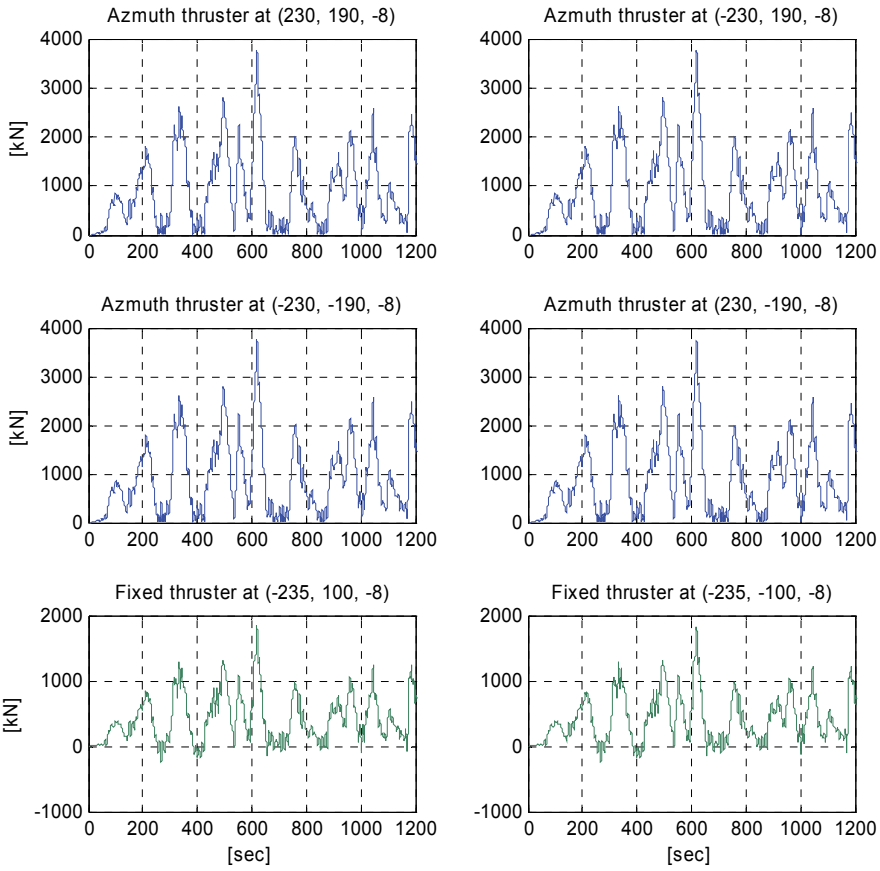

Figure 82. Allocated thrusts at each thruster

The angles in general vary in several ten seconds period with main direction to 60 degree. In 12000 sec, the series is combination of slow and fast variations with overturning occasions. In Figure 83, the top left figure is the overall time series. The top right figure shows the slowly varying azimuth angles. After the slow variation, a fast variation gets started from 250 sec and accompany with sudden overturning occasions in bottom left figure. And such a combination continues.

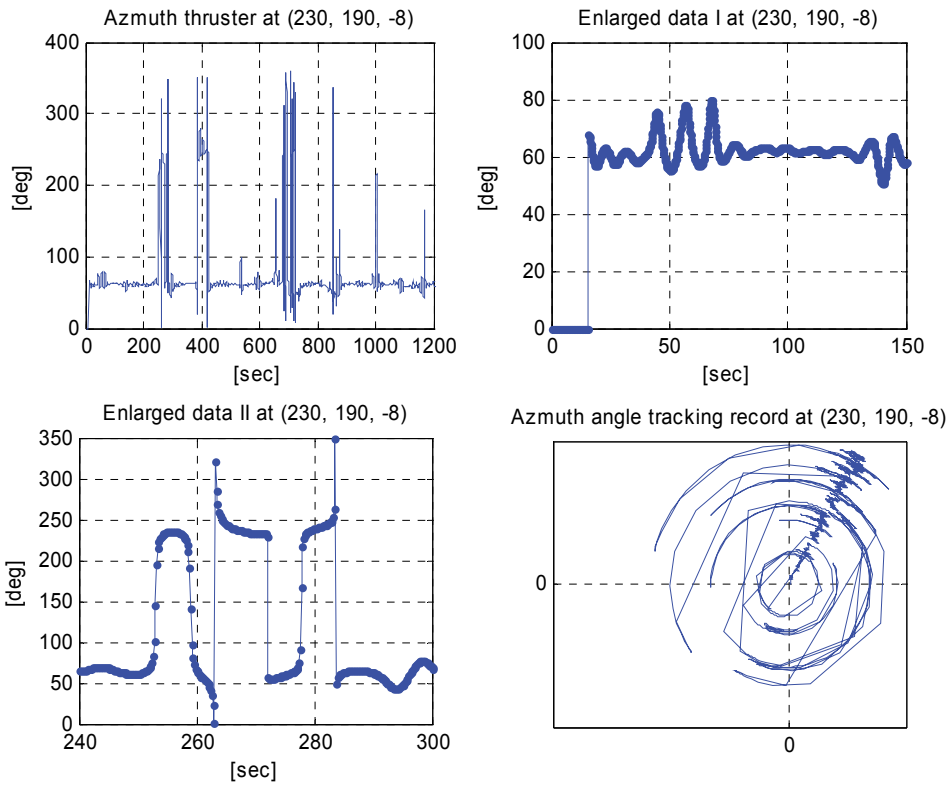

Figure 83. Angle records of azimuth thruster at (230 m, 190 m, 80 m)

The rapid changes or overturning occasions occur at where the low level of thrust is needed and the direction of thrust change happens as shown in Figure 84.

If the thrust is higher than the 1 KN, the angle varies step wise in high speed. In case the thrusts lower than 1 kN, the thruster get dormant at the previous azimuth angle and the overturning of thrust direction take place once the thrust is over 1 kN Reminding that angle is repeated every 360 deg and excluding the graphical illusion, it can be seen that the first thruster undergoes 2 rapid changes, 1 overturning, and then 1 rapid change from 250 sec.

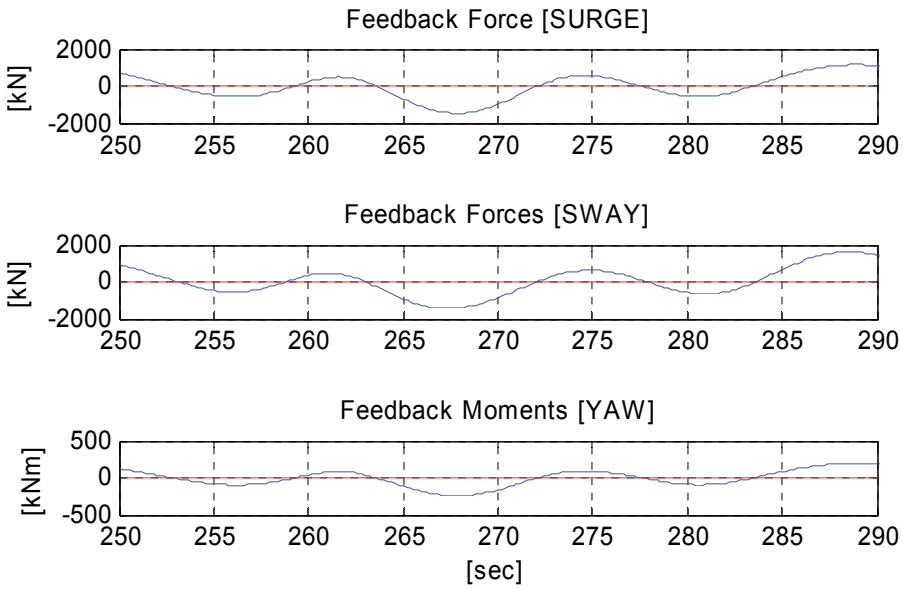

Figure 84. Enlarged feedback loads record at 250 sec to 290 sec

The tracking records of azimuth angles demonstrate the angle variations clearly as given in the bottom right figure in Figure 83. In the x-y plane view assuming the positive x axis as 0 degree with counter-clock wise direction, the angle is plotted at every time step with the instant time as the radius. The dense distribution at about 60 degree direction represents the main thrust reaction angle, and circular lines mean the rotating azimuth thruster. Furthermore, the cross straight lines are the overturning incidents. Other three azimuth thrusters have similar resultants.

As a case study, the high-accuracy DP system achieves the 2 m watch circle for the 3D pontoon in the sea state 5. Each azimuth thruster needs capacity over 4MN and the fixed thruster needs 2MN per each. The overturning incidents are feasible by changing the rotating direction of thruster propellers without impractical rapid rotating.

Mooring-combined DP System

The developed DP control is further extended to couple with the mooring-riser dynamics. Based on the taut mooring system of the 3D pontoon, the identical DP system is embedded into the fully coupled hull-mooring-riser dynamics as Figure 85.

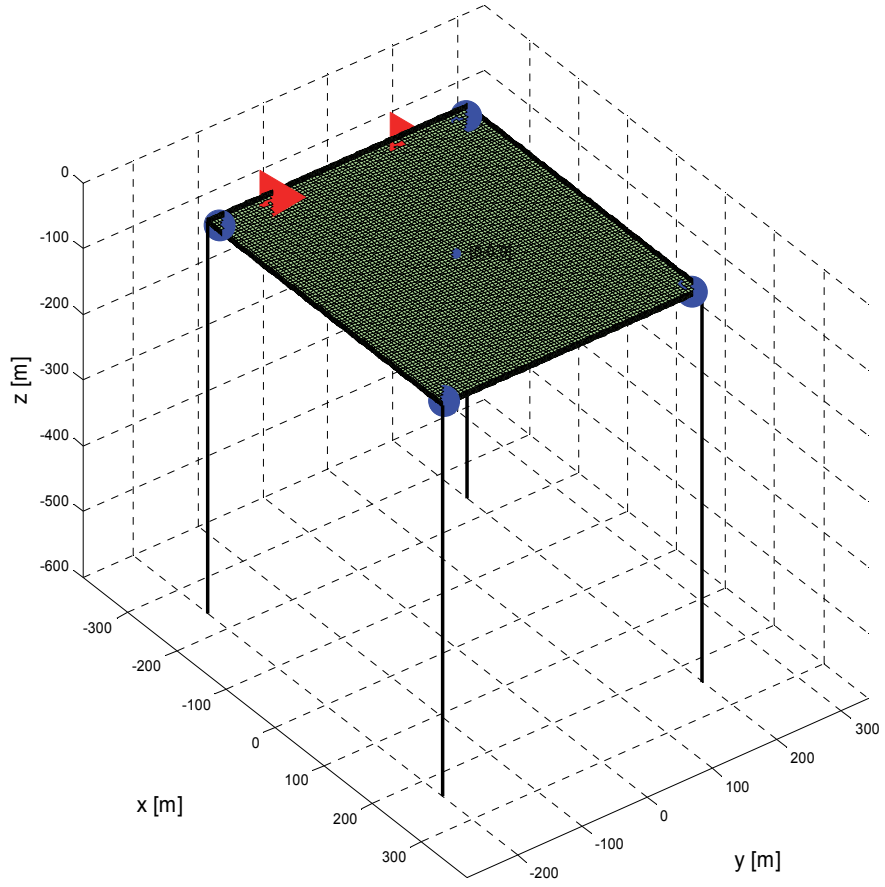

Figure 85. Schematic view of 3D pontoon with taut mooring system and DP system

With the same sea state 5 random seas in the quartering direction, the moored 3D pontoon with the DP system is investigated. As the freely floating case, the Morison

plates are included and the second order wave loading for difference frequencies are applied by Newman's approximation.

Optimum DP Control

The optimum DP control consists of 2 main components, well-defined Kalman noise parameters to remove the designated high frequency motions and optimal PD gains to generate the most efficient counteracting loads. The Kalman noise parameters depend on how much high frequency motions exist and the PD gains are determined by the performance function parameters.

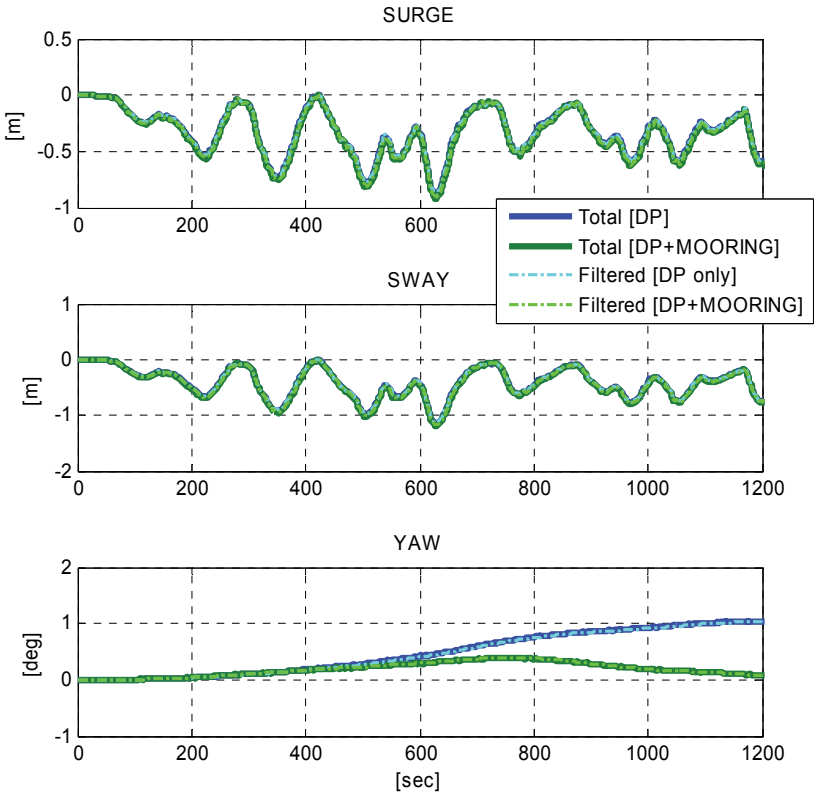

Figure 86. Horizontal motion comparisons between DP only case and DP with mooring system case

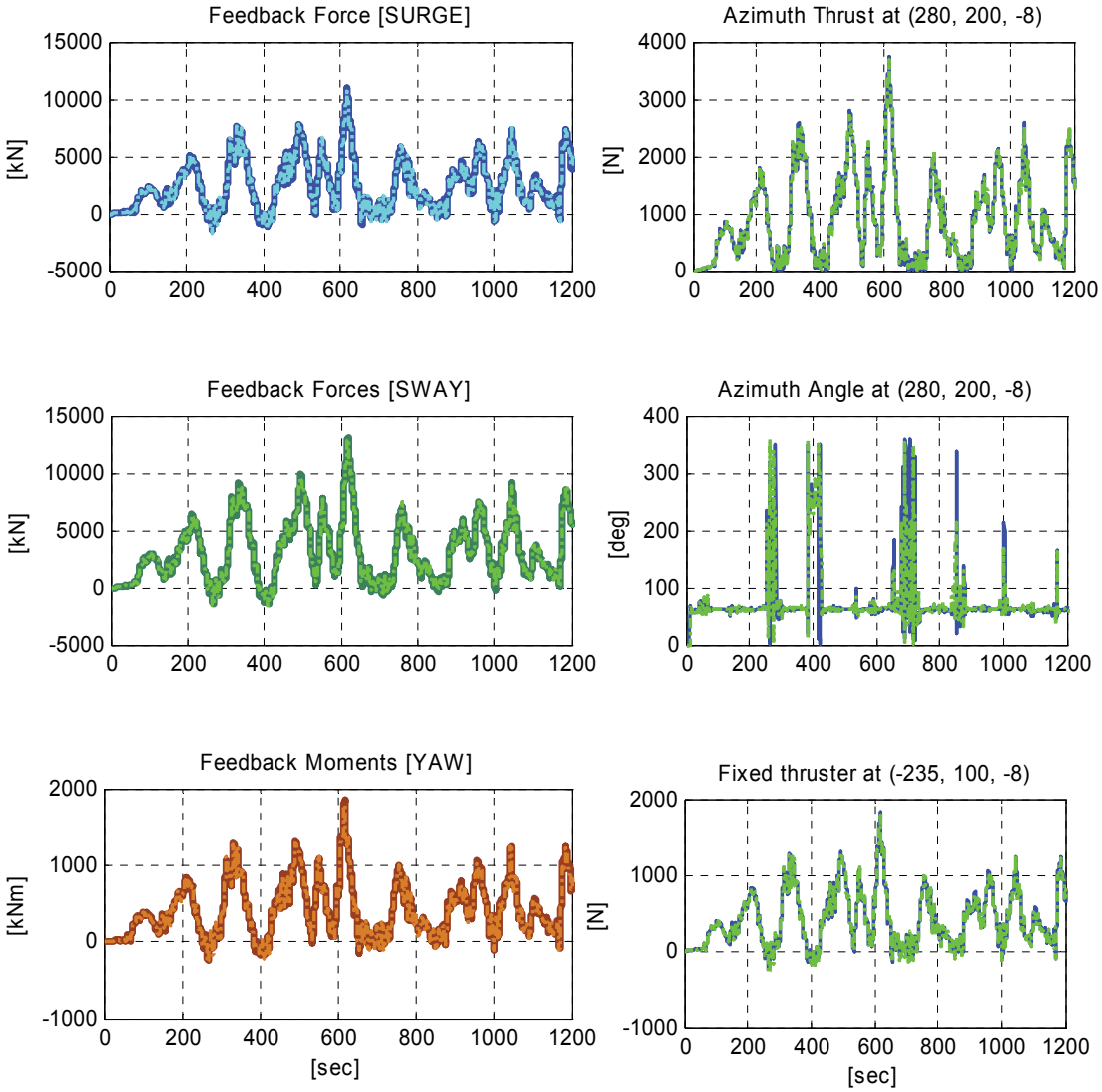

Figure 87. DP control resultants of 3D pontoon with taut mooring system (solid lines for the DP only case and dotted lines for DP and mooring combined case)

First, as shown in Figure 86, the developed high accuracy DP system is directly applied to the 3D moored pontoon in that the watch circle is small enough not to be

excited by the mooring tensions and thus the high frequency motions would be in similar scale as before.

The moored 3D pontoon has almost identical DP controlled motions in surge and sway to those of the 3D pontoon without the mooring system. In this case study, the mooring system combination with the DP system significantly improves the yaw performance. Moreover, the results represent that the optimum DP control built on the freely floating condition is still valid for the moored 3D pontoon.

The DP system generates almost same counteracting loads for both cases overall, whereas the angle records at the azimuth thrusters are a bit different in Figure 87.

Benefits of Mooring-combined DP System

Beyond the only DP-controlled system, the mooring-combined DP system can have multiple advantages in that two separate systems, DP system and mooring system, cooperate to achieve the target station keeping performance. Consequently, either or both systems would take fewer loads on the system and it could provide with more advantageous efficiency, reliability, and durability.

The comparisons of responses in Figure 87 clearly show benefits to the mooring system although the DP system takes almost same loads as the freely floating 3D pontoon with DP system only.

For clarification of the mooring-combined DP system at first, the 6 DOF responses of the moored 3D pontoon with the high accuracy DP system are compared with those without DP.

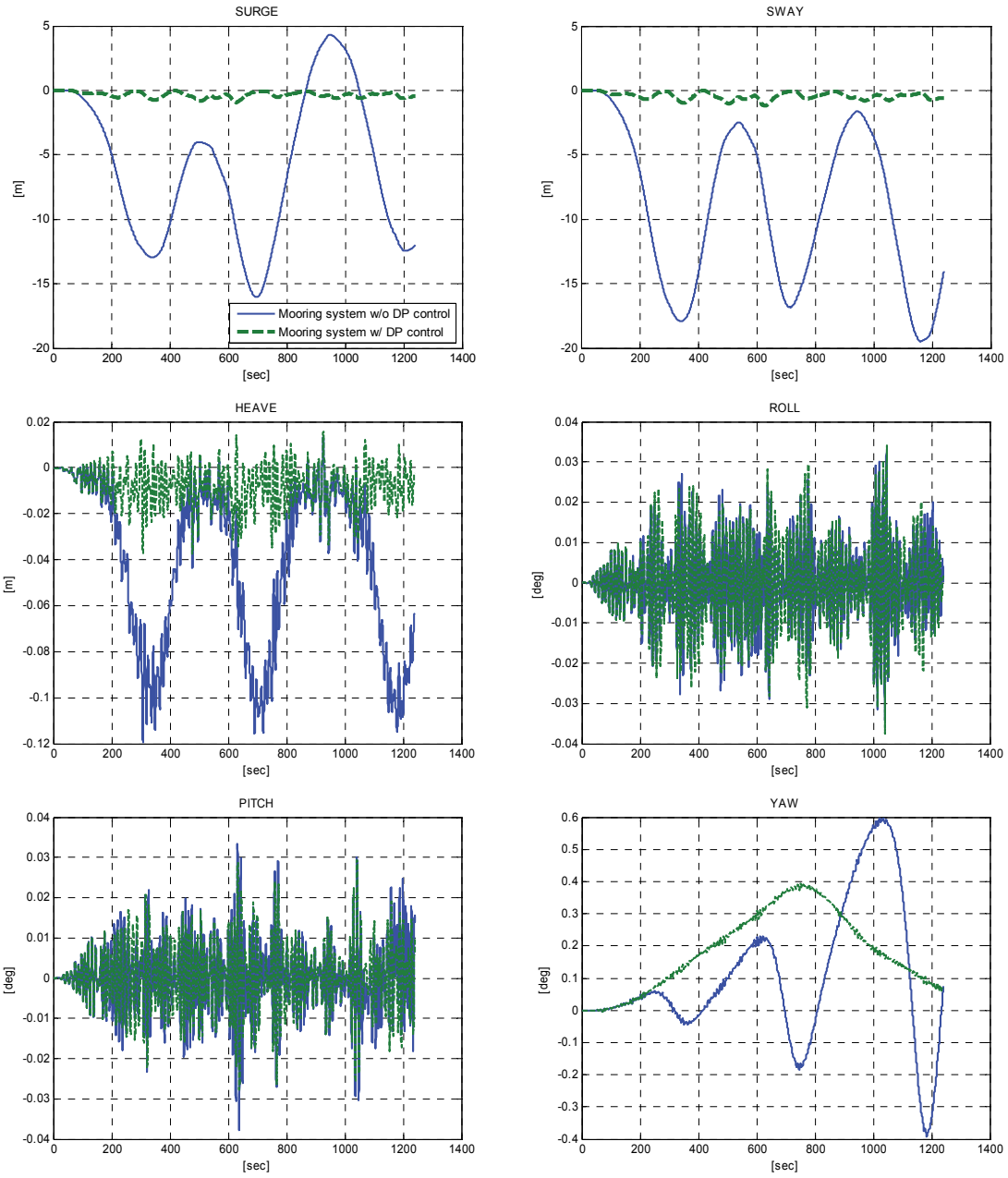

Figure 88. Comparison of 6 DOF displacements between mooring only case and mooring-DP combined case

Considering that the vertical mooring lines are vulnerable in the horizontal motions, the difference between two results is apparent in Figure 88. The 3D pontoon

with the only mooring system undergoes large and slowly-varying horizontal motions over 15 m, and the heave motions subsequently have large amplitude motions in the low frequency. It is straightforward to have much more improved global performance results by adding the high accuracy DP system to the moored pontoon with the large watch circle.

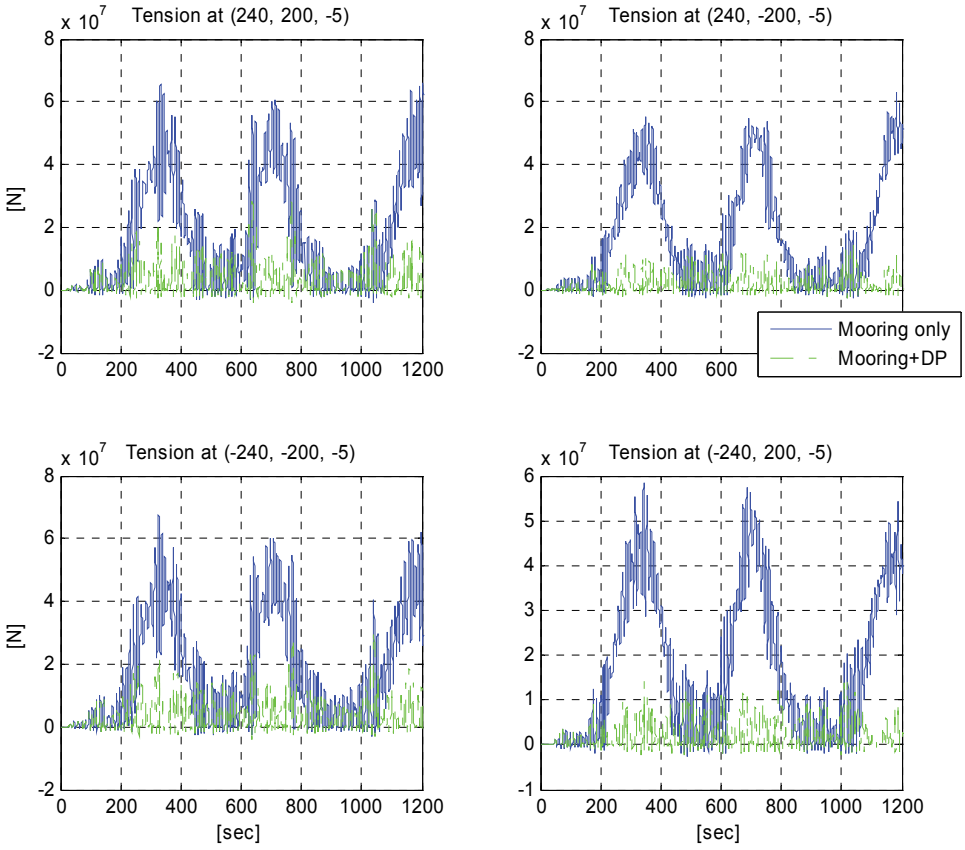

Figure 89. Comparison of mooring tensions between the only mooring case and mooring-DP combined case I

As shown in Figure 89, the mooring tensions are overwhelming in the case without the DP control and it means the high accuracy DP system takes main loads over the mooring system to achieve the watch circle 2 m. Therefore, the high accuracy DP system with mooring system is only beneficial to the mooring system, and there is insignificant difference or benefit to the DP system by adding the mooring system. It is mainly due to the mooring system design. The vertical mooring lines allow horizontal motions in tens meters and thus it can be regarded as identical motion conditions to the freely floating condition, especially for the high accuracy DP system, which allows only several meters.

If the mooring system is active within the motion range where the DP system is controlling, both of mooring and DP systems will benefit simultaneously and it can be demonstrated by conducting the general DP system which allows about the watch circle of 2~3% water depth. As an example, an additional case study is conducted for the watch circle about 10~20 m.

To allow the larger watch circle, one can decrease the *O*, response coefficients, or increase the *N*, thrust coefficients. In this study, the N is increased to reduce the PD gains with all others fixed, and thus the watch circle gets larger to 10~20 m.

$$N = \begin{bmatrix} 100 & 0 & 0 \\ 0 & 100 & 0 \\ 0 & 0 & 1 \end{bmatrix} \qquad (74)$$

The PD gains are reduced to

$$G = \begin{bmatrix} 3.2\text{E}+7 & 3.2\text{E}+5 & 0 & 0 & 0 & 0 \\ 0 & 0 & 3.2\text{E}+7 & 3.2\text{E}+5 & 0.8\text{E}+1 & -8.2\text{E}-2 \\ 0 & 0 & 1.7\text{E}+1 & 8.2\text{E}-3 & 5.8\text{E}+10 & 3.2\text{E}+7 \end{bmatrix}. \quad (75)$$

The DP control is applied to both of the freely floating condition and the moored condition and the results are compared between two cases. The horizontal motions in Figure 90 satisfy the 10~20 m watch circle in both cases but the case combined with mooring system shows the better-controlled responses with smaller amplitudes. Meanwhile, the required counteracting thrusts are smaller in the mooring-combined DP case as given in Figure 91.

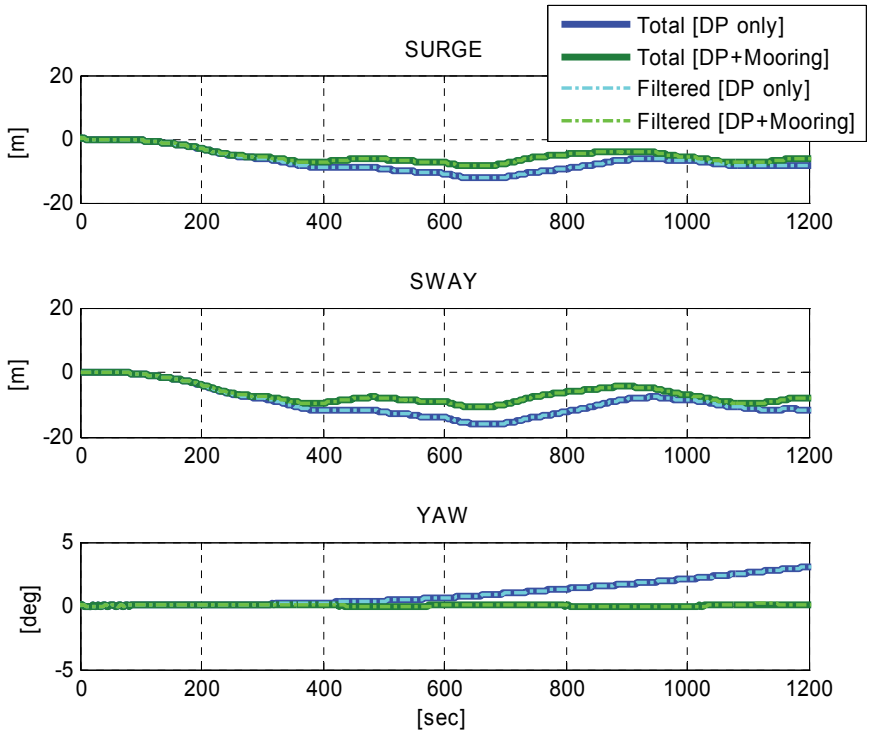

Figure 90. Horizontal motion comparison for general DP control between only DP case and DP-mooring combined case

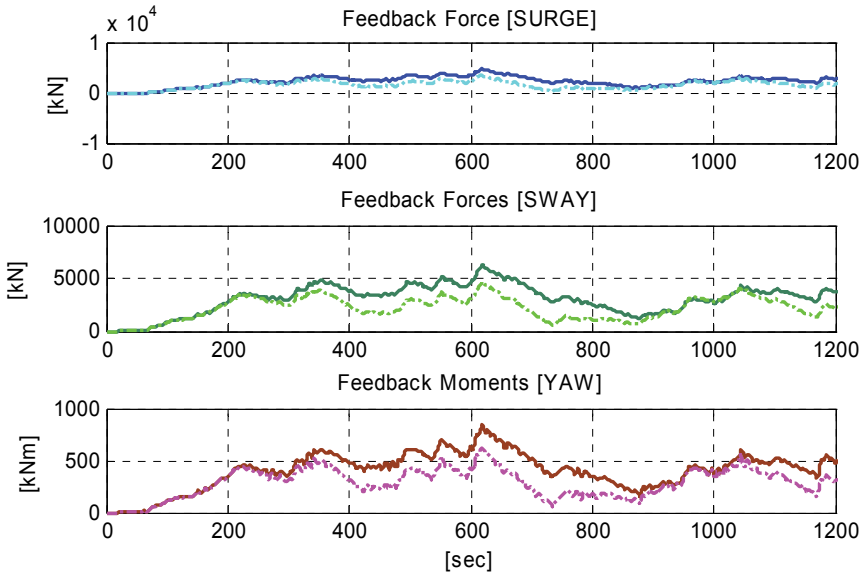

Figure 91. Counteracting loads comparison for general DP control between only DP case (solid) and DP-mooring combined case (dotted)

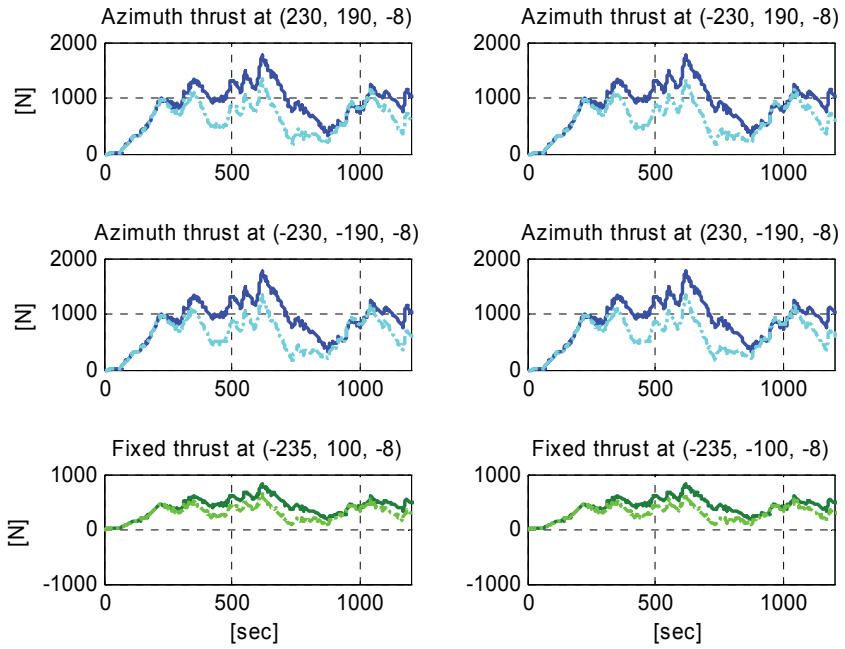

Figure 92. Individual thrust comparison for general DP control between only DP case (solid) and DP-mooring combined case (dotted)

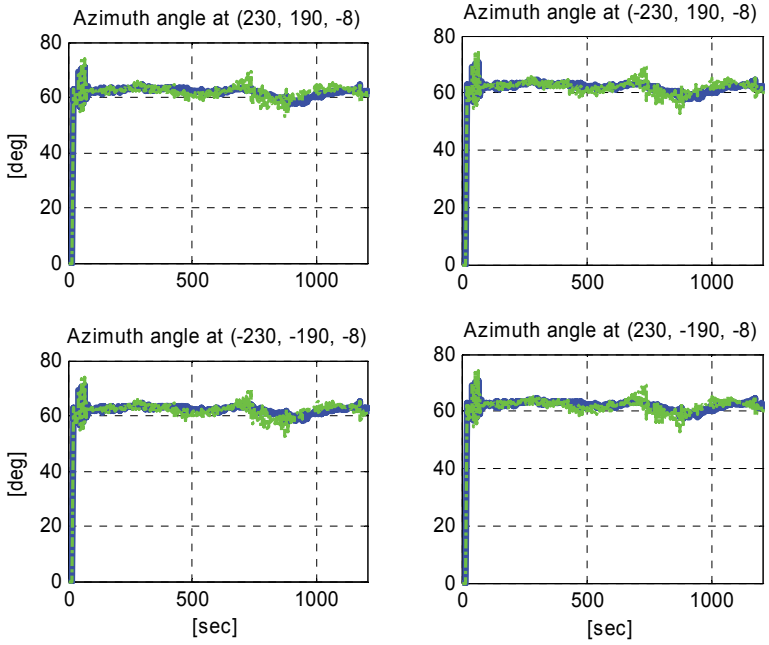

Figure 93. Individual azimuth angle comparison for general DP control between only DP case (solid) and DP-mooring combined case (dotted)

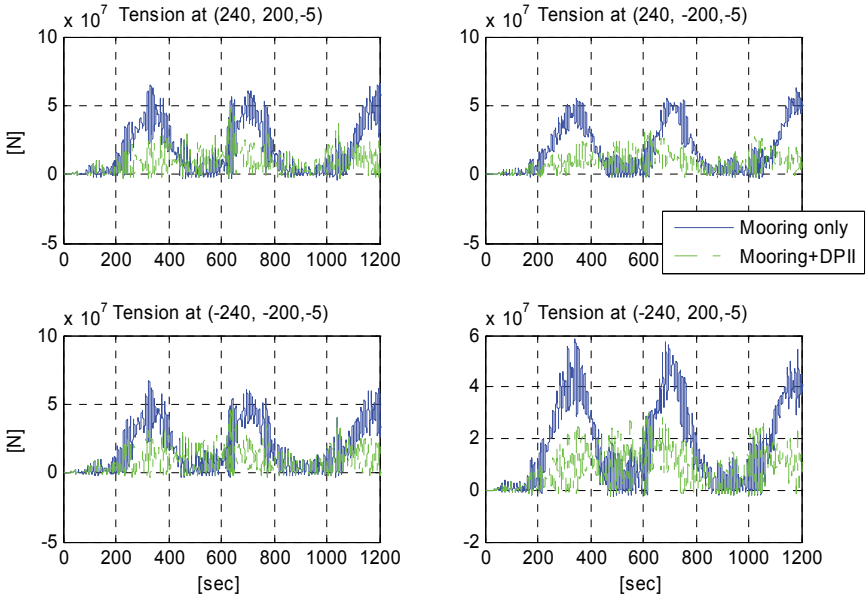

Figure 94. Comparison of mooring tensions between the only mooring case and mooring-DP combined case II

It represents the highly improved efficiency by adding the mooring line for the large watch circle cases. Consequently, the individual thrusters require the less thrust in Figure 92 and interestingly the azimuth angles have small variation at about 64 degree without any rapid change or overturning incidents as shown in Figure 93. It is mainly due to the larger watch circle makes the 3D pontoon stay in the negative x and y axes and thus the thrust angle is always positive without the change of direction sign.

Contrary to the high accuracy DP control, the general DP control with the large watch circle clearly demonstrates beneficial points by adding the mooring system. It provides with smaller motion amplitudes even with the less thruster loads. In the comparison of mooring tensions with the only mooring case in Figure 94, it is seen the mooring system takes loads to counteract, which reduces the burdens on the DP system.

9. CONCLUSION

The 3D hydroelastic analysis coupled with nonlinear mooring-riser dynamics is completed for a moored offshore structure in both the frequency and time domains. In both domains, the dynamic motion responses and stress resultants are achieved not only for regular waves but also for random seas. The coupled 3D hydroelastic analysis includes the fully coupled interactions among the floating body's dynamics and deformations, nonlinear mooring-riser's dynamics and deformations, and waves or any other environmental loads. Respective results are robustly verified across the domains, based on the cross-correlation of the frequency and time domains. In time domain, the new methodology for the direct hydroelastic structural analysis without costly CFD or DNS is developed.

A parametric study for the floating body's flexibility and a case study for a 3D structure show that the motion and stress resultants of both the floating structures and mooring-riser systems are influenced by the hydroelastic interactions, depending on the wave frequencies, headings, and resonance phenomena. The mooring tensions have significant impact on the overall stress resultants distributions and deformation shapes.

The hydroelastic dynamic analysis provides more physics with a numerical hammer test so that the real wet natural frequencies of the deformable floating body are assessed. Moreover, the developed methodology enables to estimate the fully coupled stress resultants of an offshore system in the random seas, even with the rigid body assumption. With overwhelming computation efficiency, it enables various applications such as more accurate local structural analyses without any missing loads, more realistic

fatigue analyses from the fully coupled dynamics in the random seas, and further extensions to couple with other dynamic units as wind turbines. In addition to the random seas, other types of irregular or impact loads are applicable to the hydroelastic analysis.

As another promising technology for offshore development, a high accuracy dynamic positioning system is developed. An optimum control system is achieved by combination of Kalman filtering, PD feedback control, and generalized allocation. It turns out that the appreciable small watch circles less than 2 m are achievable in the sea state 5 oblique random waves for a short operating period from the high accuracy DP control system. Subsequently, the mooring-combined DP system is investigated and it is seen that such a combined system is beneficial in that the loads to counteract can be shared by those systems, mooring system and DP system. Depending on the scale of watch circle, either one or both systems benefit with less loading on each system.

REFERENCES

[1] Arcandra, T., *Hull/mooring/riser coupled dynamic analysis of a deepwater floating platform with polyester lines*. Dissertation, Ocean Engineering, Texas A&M University, 2001, College Station, TX.

[2] Bishop, R.E.D. and W.G. Price, *Hydroelasticity of ships*. Cambridge University Press, 1979, Cambridge, UK.

[3] Cadet, O. *Introduction to Kalman filter and its use in dynamic positioning systems*. Proceedings of Dynamic Positioning Conference, 2003, Houston.

[4] Cho, I. and M. Kim, *Interactions of a horizontal flexible membrane with oblique incident waves*. Journal of Fluid Mechanics, 1998. 367: p. 139-161.

[5] Cummins, W., *The impulse response function and ship motions*. Report, David Taylor Model Basin, 1962, Washington DC.

[6] Faltinsen, O.M., *Sea loads on ships and offshore structures*. Cambridge Ocean Technology Series. Cambridge University Press, 1990, Cambridge, UK.

[7] Fossen, T.I., *Guidance and control of ocean vehicles*. Wiley, 1994, Chichester, New York.

[8] Friedland, B., *Control system design: an introduction to state-space methods*. Dover Publications, 2012, New York.

[9] Fubini, G., *Sugli integrali multipli*. Rend. Acc. Naz. Lincei, 1907. 16: p. 608-614.

[10] Garrett, D.L., *Dynamic analysis of slender rods*. Journal of Energy Resources Technology, 1982. 104(4): p. 302-306.

[11] Grimble, M.J., R.J. Patton, and D.A. Wise, *The design of dynamic ship positioning control-systems using stochastic optimal-control theory*. Optimal Control Applications & Methods, 1980. 1(2): p. 167-202.

[12] Hamamoto, T., A. Suzuki, N. Tsujioka, and K.-i. Fujita. *3D BEM-FEM hybrid hydroelastic analysis of module linked large floating structures subjected to regular waves*. Proceedings of The Eighth International Offshore and Polar Engineering Conference, 1998, Montreal, Quebec, Canada: International Society of Offshore and Polar Engineers.

[13] Kang, H. and M.H. Kim, *Hydroelastic analysis and statistical assessment of flexible offshore platforms*. International Journal of Offshore and Polar Engineering, 2014. 24(1): p. 35-44.

[14] Kang, H.Y. and M.H. Kim. *Time-domain Hydro-elastic dynamic analysis of a large floating body including second-order wave loads*. Proceedings of International Workshop on Water Waves and Floating Bodies, 2013, L'Isle sur la Sorgue, France.

[15] Kang, H.Y. and M.H. Kim. *Three-Dimensional Hydroelastic Dynamic Analyses Including Torsion for a Large Floating Platform in Frequency and Time Domains*. Proceedings of The ASME 2014 33rd International Conference on Ocean, Offshore and Arctic Engineering, 2014, San Francisco, California, USA.

[16] Kashiwagi, M., *A B-spline Galerkin scheme for calculating the hydroelastic response of a very large floating structure in waves*. Journal of Marine Science and Technology, 1998. 3(1): p. 37-49.

[17] Kashiwagi, M. *A direct method versus a mode-expansion method for calculating hydroelastic response of a VLFS in waves*. Proceedings of The Eighth International Offshore and Polar Engineering Conference, 1998, Montreal, Quebec, Canada: International Society of Offshore and Polar Engineers.

[18] Kashiwagi, M., *Research on hydroelastic responses of VLFS: Recent progress and future work*. International Journal of Offshore and Polar Engineering, 2000. 10(2): p. 81-90.

[19] Kashiwagi, M., *A time-domain mode-expansion method for calculating transient elastic responses of a pontoon-type VLFS*. Journal of Marine Science and Technology, 2000. 5(2): p. 89-100.

[20] Kim, B.W., S.Y. Hong, J.H. Kyoung, and S.K. Cho, *Evaluation of bending moments and shear forces at unit connections of very large floating structures using hydroelastic and rigid body analyses*. Ocean Engineering, 2007. 34(11-12): p. 1668-1679.

[21] Kim, M.H. and D.K.P. Yue, *The complete 2nd-order diffraction solution for an axisymmetric body .1. monochromatic incident waves*. Journal of Fluid Mechanics, 1989. 200: p. 235-264.

[22] Kim, M.H. and D.K.P. Yue, *The complete 2nd-order diffraction solution for an axisymmetric body .2. bichromatic incident waves and body motions*. Journal of Fluid Mechanics, 1990. 211: p. 557-593.

[23] Lee, C.-H., *WAMIT theory manual*. Massachusetts Institute of Technology, 1995, Cambridge, Massachusetts.

[24] Lee, C. and J. Newman, *Computation of wave effects using the panel method*. Numerical Models in Fluid Structure Interaction, 2005. 42: p. 211-251.

[25] Lee, D.H. and H.S. Choi. *Transient hydroelastic response of very large floating structures by FE-BE hybrid method*. Proceedings of The Thirteenth International Offshore and Polar Engineering Conference, 2003, Honolulu, Hawaii, USA: p. 25-30.

[26] Leissa, A.W., *Vibration of plates*. Nasa Sp-160. Scientific and Technical Information Division, National Aeronautics and Space Administration, 1969, Washington DC.

[27] Newman, J. *The evaluation of free-surface Green functions*. Proceedings of The Fourth International Conference on Numerical Ship Hydrodynamics, 1985, Washington DC

[28] Newman, J.N., *Wave effects on deformable-bodies*. Applied Ocean Research, 1994. 16(1): p. 47-59.

[29] Newman, J.N., *Marine hydrodynamics*. M.I.T. Press, 1997, Cambridge, Massachusetts.

[30] Newman, J.N., *Efficient hydrodynamic analysis of very large floating structures*. Marine Structures, 2005. 18(2): p. 169-180.

[31] Ogilvie, T.F. *Recent progress toward the understanding and prediction of ship motions*. Proceedings of The Fifth Symposium on Naval Hydrodynamics, 1964, Bergen, Norway: p. 3-80.

[32] Ran, Z., *Coupled dynamic analysis of floating structures in waves and currents*. Dissertation, Ocean Engineering, Texas A&M University, 2000, College Station, TX.

[33] Rao, S.S., *Vibration of continuous systems*. Wiley, 2007, Hoboken, New Jersey.

[34] Sordalen, O.J., *Optimal thrust allocation for marine vessels*. Control Engineering Practice, 1997. 5(9): p. 1223-1231.

[35] Stewart, J., *Calculus*. Brooks/Cole, 2009, Stamford, Connecticut.

[36] Tuitman, J. and Š. Malenica, *Fully coupled seakeeping, slamming, and whipping calculations*. Proceedings of the Institution of Mechanical Engineers, Part M: Journal of Engineering for the Maritime Environment, 2009. 223(3): p. 439-456.

[37] Watanabe, E., T. Utsunomiya, and C.M. Wang, *Hydroelastic analysis of pontoon-type VLFS: a literature survey*. Engineering Structures, 2004. 26(2): p. 245-256.